Imperial College London

Microstructurally-Sensitive Short Crack Growth in Zircaloy-4

Author: Weifeng Wan

Supervisor: Professor Fionn P.E. Dunne

A thesis submitted in part fulfilment of the requirements for the degree of Doctor of Philosophy in the Department of Materials at Imperial College London

December 2020

Abstract

This thesis explores the mechanisms of short fatigue crack growth in polycrystal Zircaloy-4 with a blocky alpha microstructure. A full-field experimental study of cyclic plastic three-point bend beam loading has been conducted on Zircaloy-4 in order to assess quantitatively the mechanistic drivers for short crack growth.

The short crack growth is sensitive to the local microstructure with respect to grain crystallographic orientation and grain boundaries in Zircaloy-4. Crack paths are observed along crystallographic planes in polycrystal blocky alpha microstructures with predominant c-axis texture aligned out-of-plane or in-plane and normal to loading. Prismatic <a>-direction crack growth rate is remarkably lower than that for prismatic <c>-direction growth for the given loading direction. Microstructural obstructions such as grain boundaries can result in obvious crack retardation of short crack growth, especially when coupled with strong deflection in crack path. Short crack growth is coupled with slip activation which has a strong effect on crack path and crack growth rate. Prism slip is associated with prismatic <a>-direction crack growth, while prism, basal and <c+a> pyramidal slips are observed in the prismatic plane <c>-direction growth.

An in-situ optical digital image correlation (DIC) technology has been utilised to measure the strain distribution in the crack-tip area. When coupled with the crystallographic orientations obtained by electron backscatter diffraction (EBSD) measurement, the measured strain fields allow a series of micro-mechanical quantities

including local stress, GND density, dissipated energy density and stored energy density to be addressed. Both the dissipated energy density and stored energy density well capture the fluctuation of crack growth rate (crack growth retardation) but the stored energy density provides better correlation. Thus, the cyclic stored energy density is found to be a potential driving force for short crack growth.

Table of contents

Abstract 3

List of Figures 7

List of Tables 14

Statement of Originality 15

Copyright Declaration 16

Acknowledgements 17

Publications 18

1. Introduction 19

2. Literature review 22

2.1. Zirconium and zirconium alloys 22

2.1.1. Chemicals and phases in zirconium 22

2.1.2. Texture in HCP zirconium 24

2.1.3. Deformation of HCP zirconium 25

2.1.4. Blocky alpha in HCP zirconium 29

2.2. Fatigue fundamentals 30

2.2.1. Cyclic deformation and fatigue life 31

2.2.2. Mechanistic studies of fatigue crack nucleation 35

2.2.3. Mechanistic studies of fatigue crack growth 37

2.2.4. Microstructurally-sensitive short crack and its driving force 43

2.2.5. Fatigue crack study in zirconium 48

2.3. Summary 50

3. Microstructure-interacting short crack growth in blocky alpha Zircaloy-4 52

3.1. Introduction 52

3.2. Materials and Methods 56

3.2.1. Texture 56

3.2.2. Blocky alpha 57

3.2.3. Three-point bend testing 58

3.2.4. SEM and EBSD 62

3.2.5. Digital image correlation 64

3.3. Short crack paths 65

3.4. Strain distribution 70

3.5. Slip activation and fracture tomography 72

3.6. Short crack growth rates 80

3.7. Twinning 90

3.8. Conclusions 94

4. Strain rate sensitivity of Zircaloy-4 at room temperature 97

4.1. Introduction 97

4.2. Methods 100
4.2.1. Crystal plasticity and thermal activation slip rule 100
4.2.2. Experimental methods 103
4.3. Microstructural characterisation 105
4.4. Local strain evolution in creep test 106
4.5. CPFE modelling of notched sample in creep and comparisons with experiment 109
4.5.1. Slip activation 110
4.5.2. Strain evolution 112
4.5.3. Stress distribution at the end of holding 114
4.6. Assessment of local strain rate sensitivity 119
4.7. Conclusions 124
5. Stored energy - Driving force for short crack growth 126
5.1. Introduction 126
5.2. Dislocation-based stored energy density criterion 129
5.3. Experimental 133
5.3.1. Fatigue test 133
5.3.2. In-situ optical DIC 134
5.4. Short crack path and crack growth rate 135
5.4.1. Microstructure and crack morphology 135
5.4.2. Crack growth rate 137
5.5. Strain and stress distributions in the crack-tip area 140
5.5.1. Strain distribution 140
5.5.2. Stress distribution 147
5.6. Strain and stress evolution in the crack-tip area during crack growth 151
5.6.1. Strain evolution in the crack-tip area 151
5.6.2. Stress evolution in the crack-tip area 157
5.7. GND density 160
5.8. Cyclic stored energy density 165
5.9. Conclusions 173
6. Conclusion and future work 175
Future work 177
References 179
Appendix 194
Appendix A. In-plane strain measurement by cross-correlation algorithm 194
Appendix B. Rotation matrices mapping the reference crystal system into the local system for specified crystallographic orientation 196
Appendix C. Gradient algorithm in GND density calculation 197

List of Figures

Fig. 2-1. Hexagonal close-packed alpha phase (a) and body-centred cubic beta phase (b) in zirconium. 23
Fig. 2-2. Pole figures of a commercial pure zirconium rolled sheet showing {0001} basal texture. 25
Fig. 2-3. Schematic of a uniaxial tensile stress applied on a pure metal single-crystal cylinder. 26
Fig. 2-4. Slip systems in HCP zirconium. Redrawn from (Hasija et al., 2003) with permission from Elsevier. 27
Fig. 2-5. (a) A schematic of a stable hysteresis loop; (b) cyclic stress-strain curve of stable hysteresis loops. Reprinted from (Suresh, 1998). 32
Fig. 2-6. Schematic of Bauschinger effect showing the stress-strain curve in a forward and reverse flow test. Redrawn from (Paul et al., 2011) with permission from Elsevier. 33
Fig. 2-7. Schematic of persistent slip bands (PSBs) structure in polycrystal. Redrawn from (Sangid et al., 2011b) with permission from Elsevier. 37
Fig. 2-8. Schematic of fatigue crack growth stages. Redrawn from (Anderson, 1996). 38
Fig. 2-9. Schematics of loading modes at cracks. Redrawn from (Anderson, 1996).... 41
Fig. 2-10. Schematic of crack-tip blunting. Redrawn from (Anderson, 1996). 42
Fig. 2-11. Schematic of the stored energy density as driving force for short crack growth. 48
Fig. 3-1. (a) SEM image of as-received Zircaloy-4 grain map; (b) inverse pole figure in the Y-direction; (c) pole figure showing the grain orientations in the area of (a)/(b). 57
Fig. 3-2. (a) SEM image and (b) IPFZ image showing the grain map in as-received fine-grain Zircaloy-4 before heat treatment; (c) SEM image and (d) IPFZ image showing the grain map in large-grain (blocky alpha) Zircaloy-4 after heat treatment..... 58
Fig. 3-3. (a) Schematic of edge-notched beam sample; (b) SEM image of edge notch; (c) 2D schematic of sample orientations in three-point bend testing with c-axis aligned

in the Z-direction in Samples A and E, while the Y-direction in Samples B, C and D; (d) cyclic loading condition; (e) image of three-point bend testing set-up.....61
Fig. 3-4. Schematic of EBSD detection showing the band width relation (PC is the pattern centre, z the distance between sample and detector). 64
Fig. 3-5. OM image (a) and SEM image (b) showing the distributed 1 μm silica speckles on the sample surface for DIC.....65
Fig. 3-6. SEM images and IPFZ at ROIs in Sample A (a) (b), Sample B (c) (d), Sample C (e) (f), Sample D (g) (h) and Sample E (i) (j). 66
Fig. 3-7. SEM and IPFZ images showing the crack path and the grain orientation for Sample A (a) (b) at cycle 3300, Sample B (c) (d) at cycle 3000, Sample C (e) (f) at cycle 2860, Sample D (g) (h) at cycle 3680, and Sample E (i) (j) at cycle 1700. 68
Fig. 3-8. (a) OM image of ROI at Cycle 1; (b) OM image of ROI at Cycle 1000; (c) enlarged OM image of (b); (d) the strain (xx) distribution of ROI at Cycle 1 and (e) at Cycle 1000, all for Sample A 71
Fig. 3-9. (a) OM image of ROI at cycle 0; strain (xx) distributions of ROIs at (b) cycle 1, (c) cycle 1000 and (d) cycle 2000, all for Sample C 71
Fig. 3-10. (a) SEM image showing the crack in Sample A; (b) SEM image of the enlarged area in the dashed red rectangle in (a). Broken lines indicate active slip systems, and dotted lines crack paths. 75
Fig. 3-11. (a) SEM image showing a part of the crack path of Sample C from nucleation site to D4; (b) SEM image of the enlarged area in the dashed black rectangle in (a); (c) SEM image of the enlarged area in the dashed red rectangle in (a). 76
Fig. 3-12. (a) OM image showing the crack path of Sample D; (b) SEM image showing the pyramidal slip trace near the crack path in Grain D1. 76
Fig. 3-13. (a) SEM image showing the crack path in Sample E, Grain E2; (b) SEM image of the enlarged area in the dashed red rectangle in (a) showing the prismatic slip trace near the crack path. 77
Fig. 3-14. (a) SEM image of fracture surface of Sample A; (b) SEM image of the enlarged area in the dashed red rectangle in (a) showing prism planar regions on the fracture surface; (c) SEM image of an enlarged area in (b) showing striations parallel to crystal

c-axes; (d) SEM image of fracture surface of Sample D; (e) SEM image of the enlarged area in the dashed blue rectangle in (d) showing the prism planar regions; (f) SEM image of an enlarged area in (e) showing striations parallel to <c+a> directions. 79
Fig. 3-15. (a) Crack length versus cycle number, and (b) da/dN versus ΔK in Sample A. 84
Fig. 3-16. (a) Crack length versus cycle number, and (b) da/dN versus ΔK in Sample B. 84
Fig. 3-17. (a) Crack length versus cycle number, and (b) da/dN versus ΔK in Sample C. 84
Fig. 3-18. (a) Crack length versus cycle number, and (b) da/dN versus ΔK in Sample D. 85
Fig. 3-19. (a) Crack length versus cycle number, and (b) da/dN versus ΔK in Sample E. 85
Fig. 3-20. (a) SEM image of crack tip area in Sample A; (b) IPFX image of the same area as (a); (c) the crystallographic orientation of the Twin 1 and parent; (d) the crystallographic orientation of the Twin 2 and parent. 93
Fig. 3-21. (a) SEM image of crack tip area in Sample C; (b) IPFX image of the same area as (a); (c) enlarged image of the black dashed rectangular area in (b); (d) enlarged image of the yellow dashed rectangular area in (b); (e) crystallographic orientations of the twin and parent in (c); (f) crystallographic orientations of the twin and parent in (d). 94
Fig. 4-1. Schematic diagram of (a) a dislocation escaping an obstacle through a thermal activation process and (b) the corresponding energy barrier curves (Dunne et al., 2007; Granato et al., 1964; Zheng et al., 2016b). 103
Fig. 4-2. (a) Optical microscope image of the edge notch at the middle bottom of the beam sample; (b) loading history of the three-point bend creep test. 105
Fig. 4-3. (a) SEM image and (b) IPFZ showing grain morphologies and crystallographic orientations near the notch of Sample MZ. 106
Fig. 4-4. Experimentally measured total strain (xx) evolution distributions (a-n) at holding time from 0 s to 3600 s; and (o) in the unloaded condition in Sample MZ. .108

Fig. 4-5. (a) Strain (xx) field in the unloaded condition; (b) strain (xx) variations along the red dashed line marked in (a) at different hold time. 108
Fig. 4-6. (a) Full finite element model of three-point bend testing on an edge-notched beam sample; (b) sub-model in the truncated area of full model. 110
Fig. 4-7. CPFE modelling results showing distribution of the resolved shear strain γ of prismatic slip systems in Grain M1 when creep holding for 3600s: (a) Prismatic Slip 1; (b) Prismatic Slip 2; (c) Prismatic Slip 3 (Liu et al., 2020). 111
Fig. 4-8. Strain (xx) distribution near the notch from CPFE simulations compared with DIC results at different holding time frame of (a) 0 s, (b) 30 s, (c) 300 s, (d) 1200 s, (e) 3600 s and (f) in the unloaded condition. 113
Fig. 4-9. (a) Strain (xx) field near the notch at the start of holding; (b) The average strain (xx) evolution of the white dashed area marked in (a); (c) strain (xx) evolution of point P marked in (a). 114
Fig. 4-10. DIC measured elastic strain component distributions of Sample MZ when holding for 3600s: (a) elastic strain (xx); (b) elastic strain (xy); (c) elastic strain (yy). 117
Fig. 4-11. Comparison of local stress components between DIC experiment and CPFE modelling: (a) stress (xx), (b) stress (yy) and (c) stress xy obtained from experimental results; (d) stress (xx), (e) stress (yy) and (f) stress (xy) obtained from simulation results; (g) line graph showing the stress (xx) from point S to S' as marked in (a) and (d). ...118
Fig. 4-12. Effective strain ε, strain rate $\dot{\varepsilon}$, and strain rate sensitivity m distribution when stress holding for (a) (e) (i) 5 s, (b) (f) (j) 20 s, (c) (g) (k) 120 s and (d) (h) (l) 1800 s in a creep test. 123
Fig. 4-13. Local strain rate sensitivity (HT = 5 s) variation along path A-B across the Grain boundary between M1 and M2. 124
Fig. 5-1. In-situ micro-scale optical digital image correlation set-up. 134
Fig. 5-2. SEM images showing notch geometries and crack paths in Sample AZ (a) and Sample BY (b); (c) IPFZ of Sample AZ; (d) IPFY of Sample BY. 136
Fig. 5-3. Crack length versus cycle number in Sample AZ (a) and BY (b); (c) crack growth rate versus effective crack length in Samples AZ (red) and BY (blue); (d) optical

microscope (OM) images with grain boundaries overlapping showing the events when the short crack encounters microstructural obstructions from cycle 2100 to 2400 in Sample BY. 139
Fig. 5-4. Total strain distribution of Sample AZ in the area near the crack-tip at cycle 2200 with the effective crack length at around 500 μm: (a) total strain (xx); (b) total strain (xy); (c) total strain (yy). 142
Fig. 5-5. Total strain distribution of Sample BY in the area near the crack-tip at cycle 2400 with the effective crack length at around 500 μm: (a) total strain (xx); (b) total strain (xy); (c) total strain (yy). 143
Fig. 5-6. (a) IPFZ of Sample PZ; (b) SEM image showing the area in the dashed rectangular; (c) enlarged SEM images of (b) showing the slip traces near the crack-tip. 144
Fig. 5-7. (a) OM image of Sample QY1 showing a crack path; (b) enlarged SEM image of (a) at the crack tip; (c) SEM image of Sample QY2; (d) enlarged SEM image of (c) at the crack-tip. 145
Fig. 5-8. Elastic strain distribution of Sample AZ in the area near the crack-tip at cycle 2200 with the effective crack length at around 500 μm: (a) elastic strain (xx); (b) elastic strain (xy); (c) elastic strain (yy). 146
Fig. 5-9. Elastic strain distribution of Sample BY in the area near the crack-tip at cycle 2400 with the effective crack length at around 500 μm: (a) elastic strain (xx); (b) elastic strain (xy); (c) elastic strain (yy). 147
Fig. 5-10. Stress distribution of Sample AZ in the area near the crack-tip at cycle 2200 with the effective crack length at around 500 μm: (a) stress (xx); (b) stress (xy); (c) stress (yy). 150
Fig. 5-11. Stress distribution of Sample BY in the area near the crack-tip at cycle 2400 with the effective crack length at around 500 μm: (a) stress (xx); (b) stress (xy); (c) stress (yy). 151
Fig. 5-12. Evolution of effective plastic strain distribution of Sample AZ in the ROI in the unloaded condition from cycle 1000 to 2400 with the effective crack length from 380 to 520 μm (The black arrow marks the crack tip). 154

Fig. 5-13. Evolution of effective total strain distribution of Sample AZ in the ROI at peak load from cycle 1000 to 2400 with the effective crack length from 380 to 520 μm (The black arrow marks the crack tip). 155
Fig. 5-14. Evolution of effective plastic strain distribution of Sample BY in the ROI in the unloaded condition from cycle 1800 to 2800 with the effective crack length from 360 to 640 μm (The black arrow marks the crack tip). 155
Fig. 5-15. Evolution of effective total strain distribution of Sample BY in the ROI at peak load from cycle 1800 to 2800 with the effective crack length from 360 to 640 μm (The black arrow marks the crack tip). 156
Fig. 5-16. Average effective strains of Sample AZ and BY in the crack-tip ROI area (150 μm × 300 μm) versus effective crack length. 156
Fig. 5-17. (a) SEM image showing the crack-tip of Sample AZ at cycle 2400; (b) IPFX image showing the twinning at the crack-tip in an enlarged area in (a). 157
Fig. 5-18. Evolution of Von Mises stress distribution of Sample AZ in the crack-tip area at peak load from cycle 1000 to 2400 (The black arrow marks the crack tip)..... 158
Fig. 5-19. Evolution of Von Mises stress distribution of Sample BY in the crack-tip area at peak load from cycle 1800 to 2800 (The black arrow marks the crack tip)..... 158
Fig. 5-20. Average Von Mises stresses at peak load in the ROI versus effective crack length of Samples AZ and BY. 160
Fig. 5-21. Evolution of GND density of Sample AZ from cycle 1000 to 2400 (The black arrow marks the crack tip). 163
Fig. 5-22. Evolution of GND density of Sample BY from cycle 1800 to 2800 (The black arrow marks the crack tip). 164
Fig. 5-23. (a) Average GND density in the ROI and (b) local GND density ahead of the crack-tip versus effective crack length. 165
Fig. 5-24. Schematic of cyclic dissipated energy density calculation: (a) the crack growth from cycle i-k to cycle i with a crack advance Δa; (b) the stress at peak load versus accumulated plastic strain in the ROI. 167
Fig. 5-25. Evolution of cyclic stored energy density distribution in the ROI of Sample AZ (The black arrow marks the crack tip). 169

Fig. 5-26. Evolution of cyclic stored energy density distribution in the ROI of Sample BY (The black arrow marks the crack tip). 169
Fig. 5-27. (a) Average cyclic dissipated energy density in the ROI versus effective crack length; (b) average cyclic stored energy density in the ROI versus effective crack length. 172
Fig. 5-28. (a) Local cyclic dissipated energy density and (b) local cyclic stored energy density at the crack-tip versus effective crack length. 173
Fig. A-1 Schematic illustration of a reference square subset before and after deformation. Reprinted from (Pan et al., 2009). 195
Fig. A-2. Schematic of configuration deformation with in-plane displacement *u* and *v*. 196

List of Tables

Table 2-1. Twinning types in zirconium (Tenckhoff, 1988; Tong, 2016). 28

Table 3-1. Summary of sample geometry, loading conditions and edge-notch shape in Samples A, B, C, D and E. 62

Table 3-2. Grain Euler angles and slip system maximum (apparent) Schmid factor before deformation in Samples A, C, D and E. 73

Table 3-3. Surface crystallographic crack growth rates (***b*** indicates corresponding Burgers vector direction, and non-***b*** indicates normal to Burgers vector respectively for surface crack growth). 86

Table 4-1. Beam geometries and notch shape of Sample MZ. 104

Table 4-2. Grain Euler angles and slip system maximum Schmid Factors in Sample MZ. 112

Table 4-3. Plastic properties for prismatic slip of Zircaloy-4 at 20 °C (Liu et al., 2020). 119

Table 5-1. Summary of sample geometry including edge-notch shape and loading conditions in Samples AZ and BY. 133

Statement of Originality

This thesis is the summary of research work carried out in the Department of Materials, Imperial College London from October 2016 to December 2020, under the supervision of Professor Fionn P.E. Dunne. I, Weifeng Wan, confirm:

- The work presented in this thesis, except where otherwise acknowledged or stated, is entirely my own original work at Imperial College London.
- All the sources I have used or quoted from are appropriately referenced within this thesis.
- Where the thesis is presented on the work done by myself jointly with others, I have clearly stated the contributions from myself and others.

Copyright Declaration

The copyright of this thesis rests with the author and is made available under a Creative Commons Attribution Non-Commercial No Derivatives licence. Researchers are free to copy, distribute or transmit the thesis on the condition that they attribute it, that they do not use it for commercial purposes and that they do not alter, transform or build upon it. For any reuse or redistribution, researchers must make clear to others the licence terms of this work.

Acknowledgements

Over the past four years I have been grateful to have the opportunity to study at Imperial College London. There are a number of people who helped me in the completion of my PhD thesis that I would like to acknowledge.

Firstly, Professor Fionn Dunne whose supervision has provided me with strong belief and continuous support throughout my PhD. Without him I would not have completed this thesis, nor had I achieved my work published in top journals. The past few years have been the most challenging and enjoyable time of my life. Thank you!

Dr Ben Britton and Dr Jun Jiang for their insightful views and suggestions on my experimental work.

All of my colleagues in the Micromechanics Group for their help and encouragement in my PhD research. It has been a great pleasure to work with you at Imperial.

Dr Mahmoud Ardakani for microscopy training and Mr Ben Wood for technical support and lab management, both of which require huge amounts of patience.

Industrialists from Rolls-Royce plc who provided Zircaloy-4 material, and Imperial College-China Scholarship Council for financial support.

Lastly, my loving parents for their selfless support and understanding!

Publications

- Y. Xu, **W. Wan***, F.P.E. Dunne, Microstructural fracture mechanics: Stored energy density at fatigue cracks, **Journal of the Mechanics and Physics of Solids**. 146 (2021) 104209. https://doi.org/10.1016/j.jmps.2020.104209.
- **W. Wan***, F.P.E. Dunne, Microstructure-interacting short crack growth in blocky alpha Zircaloy-4, **International Journal of Plasticity**. 130 (2020) 102711. https://doi.org/10.1016/j.ijplas.2020.102711.
- D. Wilson*, **W. Wan**, F.P.E. Dunne, Microstructurally-sensitive fatigue crack growth in HCP, BCC and FCC polycrystals, **Journal of the Mechanics and Physics of Solids**. 126 (2019) 204–225. https://doi.org/10.1016/j.jmps.2019.02.012.

1. Introduction

Research in nuclear materials has been increasing with the continued development of the nuclear industry. Zirconium alloys are widely used as fuel claddings and pressure tubes in the core of reactors due to their good ductility, high corrosion resistance and low cross-section to thermal neutrons. The principal properties of these zirconium alloys are dominated by the hexagonal close-packed (HCP) alpha phase. Zircaloy-4, which is the focus of this thesis, has the nominal composition of Zr-1.5 wt%Sn-0.2 wt%Fe-0.1 wt%Cr (Northwood, 1985).

Power fluctuations by demand in a nuclear reactor core lead to periodic swelling of the fuel pellets and reversing to their original size which gives rise to cyclic loads on Zircaloy cladding which will lead to component failure. Such a low cycle fatigue process could have lethal consequences when cracks nucleate and grow in Zircaloy cladding in service. Therefore, the estimation of fatigue life of zirconium alloys and understanding mechanisms of crack nucleation and propagation are of great significance for industrial safety.

Short cracks or small cracks imply the crack length of several grains. In many cases, a large proportion of the total fatigue life is consumed by short crack growth (Suresh and Ritchie, 1984). The short crack growth is sensitive to local microstructures including grain morphology and crystallographic orientation at the mesoscale and lattice curvature, dislocation substructures and grain boundaries at the microscale (Pineau et al., 2016). Interacting with the local microstructure, short crack exhibits a number of characteristic behaviours such as tortuous crack paths and fluctuating crack growth

rates. Traditional fracture mechanics of ductile metals assumes that materials will crack in a homogeneous, isotropic and elastic-plastic medium, and thereby does not explicitly recognise microstructure. Pioneering methodologies including the Griffith fracture energy (Griffith, 1921), the stress intensity factor (Irwin, 1957) and J-integral (Rice, 1968) have been extensively applied to characterise the crack growth at the macro-scale; however, they reflect neither the characteristic length scale, nor the mechanistic crack tip drivers when the crack length is in the scale of several grains. Wilson and co-workers (Wilson et al., 2019, 2018) have recently established a model in which the stored energy density is identified as a driving force for short crack growth. The stored energy density is a physically based quantity which considers local strain, local stress and dislocation density. The results of simulation work from Wilson and co-workers encourages experimental investigation and especially the direct measurement of the stored energy density. For further understanding on the mechanism of short crack growth, this challenge is the main subject of this thesis.

To achieve the measurement of a succession of mechanical quantities including local strain, stress and GND density, a novel in-situ high-resolution digital image correlation (DIC) technology has been applied. In addition, scanning electron microscope (SEM) coupled with electron backscatter diffraction (EBSD) are used to obtain the grain information such as grain morphology, grain size distribution, crystallographic orientation and texture. DIC and EBSD are the main microstructural characterisation techniques utilised throughout this thesis.

Chapter 3 explores the short crack growth in large-grain Zircaloy-4. Experimental crack

growth rate studies with respect to local grain morphology and crystallographic orientation are addressed. The difference of crack growth rates are assessed in the context of texture. Considering the challenge of in-situ strain measurement near the crack-tip or notch, Chapter 4 firstly assesses the strain rate sensitivity of Zircaloy-4 at the micro-scale and suggests a real-time in-situ DIC technology is necessary. Furthermore, the measured strains and consequence for calculated stresses in a creep test is validated using crystal plasticity finite element (CPFE) modelling carried out independently (Liu et al., 2020) in Chapter 4, which paves the way to obtain the reliable micromechanical quantities near the crack-tip in the short crack growth in experiment. In Chapter 5 a full-field experimental study on the driving force for short crack growth has been conducted by using in-situ DIC technology and EBSD examination, and is the first time that stored energy density in crack-tips has been measured experimentally and used to assess its microstructural sensitivity. To calculate the stored energy density in crack-tips a new DIC setup which can achieve the resolution of strain to 3 μm has been established, and new methods and corresponding algorithms have been developed to calculate the stress and GND density fields at crack-tips.

The aim of this thesis is to enhance the understanding of fundamental mechanisms of short crack growth by utilising state of the art characterisation techniques. This knowledge has direct relevance and impact for the understanding of fatigue crack paths and growth rates in Zircaloy-4 of importance in the nuclear power industry.

2. Literature review

The literature review begins with the knowledge of zirconium and zirconium alloys including the introduction of the physical metallurgy of zirconium and the deformation of hexagonal close-packed (HCP) zirconium. Then it continues with the review of the fatigue crack fundamentals including the methods of fatigue life estimation, the mechanistic studies of fatigue crack nucleation and propagation, microstructural-sensitive short crack and particular investigations of fatigue crack growth in zirconium alloys. Finally, the main scientific questions which still exist and the objectives of this study are summarised.

2.1. Zirconium and zirconium alloys

2.1.1. Chemicals and phases in zirconium

The first zirconium metal was prepared by Berzilius in 1824. In their early reported applications zirconium metals were used in pyrophoric devices such as fuses, ammunition primers and fireworks. Zirconium and zirconium alloys have been utilised in the nuclear industry since the end of 1950s as they have a low absorption cross-section of thermal neutrons, a high corrosion resistance and good mechanical properties (Nielsen and Wilfing, 2012). Although pure zirconium is very reactive in air and solutions, a stable, adherent oxide film forms immediately on the surface which protects zirconium from further oxidation or corrosion. To further enhance the corrosion resistance and strengthen the mechanical properties for the use in nuclear reactors, other

alloying elements are added to prepare new zirconium alloys. This study focuses primarily on Zircaloy-4, which has a nominal composition of Zr-1.5Sn-0.2Fe-0.1Cr (wt. %).

Like the other IVa transition metals Ti and Hf, Zr has the low temperature phase (alpha) with a HCP structure and a high temperature phase (beta) with a body-centred cubic (bcc) structure, respectively (Willaime and Massobrio, 1989). The transition temperature between alpha and beta phase for pure zirconium is 862 °C at constant pressure (Toffolon-Masclet et al., 2008). Fig. 2-1 shows the atomic structure of alpha and beta phase in zirconium. Another hexagonal structure phase, omega phase may be present as a metastable precipitate which forms during low-temperature aging or quenching from above the alpha-beta transition temperature. The existence of the omega phase results in increase in strength but a large reduction in ductility (Hickman, 1969).

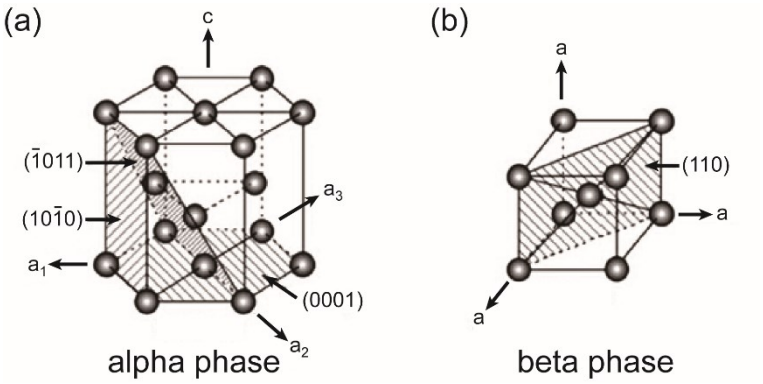


Fig. 2-1. Hexagonal close-packed alpha phase (a) and body-centred cubic beta phase (b) in zirconium.

2.1.2. Texture in HCP zirconium

Kearns proposed a method to characterise preferred orientation in HCP alloys (Kearns, 1965). This method was used to determine an orientation parameter, the Kearns factor '*f*', which is defined as a weighted average of the basal pole figure intensity with respect to the sample normal direction. Perfect alignment of the basal poles in one direction yields an '*f*' value of 1.0 in that direction and zero in $<10\bar{1}0>$ and $<11\bar{2}0>$ directions; a value of 1/3 is obtained for all directions in a random sample (Kearns, 2001).

There are two typical deformation textures in zirconium: prismatic texture and basal texture. The prismatic texture forms when the HCP c-axes are perpendicular to the compression loading axes, while the basal texture refers to the compression direction aligned with the c-axes. Prismatic textures are found to yield at lower stress than basal textures (Kaschner and Gray, 2000; McCabe et al., 2006). Fig. 2-2 shows the pole figures of a commercial pure zirconium rolled sheet. Typical basal texture is seen with c-axis <0001> aligned with the normal direction of the sheet (Z-direction).

Grain size has a profound effect on the deformation texture evolution in zirconium alloys. Salinas (Salinas-Rodriguez, 1995) compared to the texture characteristics of the compressed fine-grain and coarse-grain samples of Zr-2.5Nb and found that a $<11\bar{2}0>$ fibre texture and a [0001] fibre texture tilted approximate 20° towards the compression direction are shown in the fine grain microstructure, while a basal texture is seen in the large-grain microstructure characterized as a sudden rotation of the <c> axis to became parallel to the compression direction.

The texture evolution in zirconium is also a function of applied strain. Gerspach et al (Gerspach et al., 2009) studied the texture in a recrystallized low-alloyed zirconium sheet (Zr702) showing that recrystallized texture changes with respect to the reduction ratios. The initial deformation texture has a strong effect on the final-step texture. It is concluded that increasing the amounts of deformation facilitate the rotation of the <c> axis towards the compression axis.

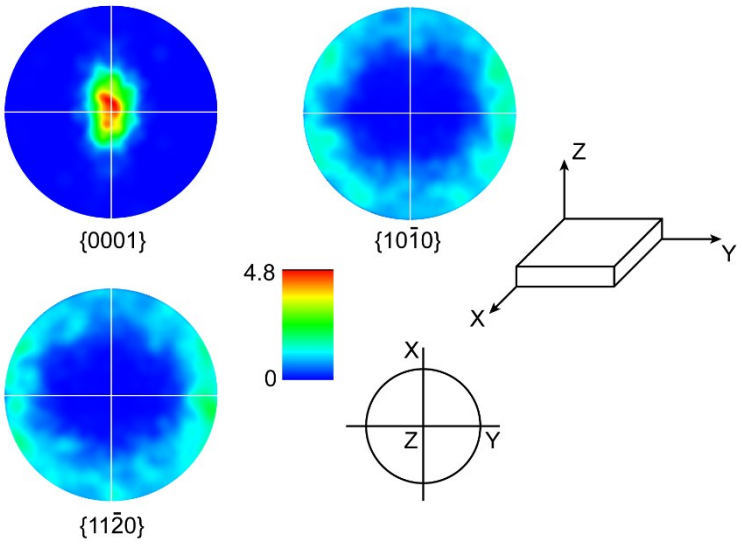


Fig. 2-2. Pole figures of a commercial pure zirconium rolled sheet showing {0001} basal texture.

2.1.3. Deformation of HCP zirconium

2.1.3.1. Slip systems in HCP zirconium

The activation of a slip system relies on the resolved shear stress on slip plane achieving a critical value, which is known as critical resolved shear stress (CRSS), τ_c. The CRSS can be measured directly by conducting a uniaxial tension or compression test on an

oriented single-crystal sample (Akhtar, 1973a) as shown in Fig. 2-3. The resolved shear stress is given by

$$\tau_r = \frac{F_r}{A_1} = \frac{F\cos\lambda}{A_0/\cos\theta} = \frac{F}{A_0}\cos\theta\cos\lambda = \sigma\cos\theta\cos\lambda \qquad (2\text{-}1)$$

where A_1 is the slip plane area, A_0 the cross-section area of the cylinder, F_r the shear force, λ the angle between the axial force F and the slip direction, and θ the angle between F and the normal to the slip plane. This equation is also known as Schmid's Law, and $\mu = \cos\theta\cos\lambda$ is defined as Schmid Factor (Boas and Schmid, 1936).

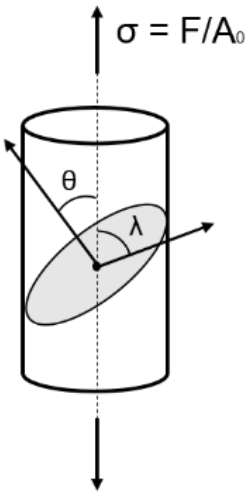


Fig. 2-3. Schematic of a uniaxial tensile stress applied on a pure metal single-crystal cylinder.

HCP crystallography results in considerable anisotropy in elastic and plastic mechanical properties, in which slip systems play a significant role in the plastic deformation. The slip systems in alpha-zirconium (HCP) are shown in Fig. 2-4. <a> direction slips occur on $\{0001\}$ basal, $\{10\bar{1}0\}$ prismatic and $\{10\bar{1}1\}$ pyramidal planes, while <c+a> direction slip occurs on $\{\bar{1}011\}$ (1st order) and $\{11\bar{2}2\}$ (2nd order) planes. <a>

prismatic slip is the dominant slip system in the deformation of HCP zirconium at room temperature, while <a> basal slip and <c+a> slip are less favoured with higher CRSS than <a> prismatic slip (Akhtar, 1973b; Akhtar and Teghtsoonian, 1971; Rapperport, 1959). The CRSS of <a> prism, <a> basal, and <c+a> first order pyramidal slip systems in zirconium are determined as 153 ± 30 MPa, 204 ± 66 MPa and 532 ± 58 MPa by Gong et al (Gong et al., 2015) who used focused ion beam (FIB) to prepare single crystal cantilevers from individual polycrystals of particular crystallographic orientation in commercially pure zirconium.

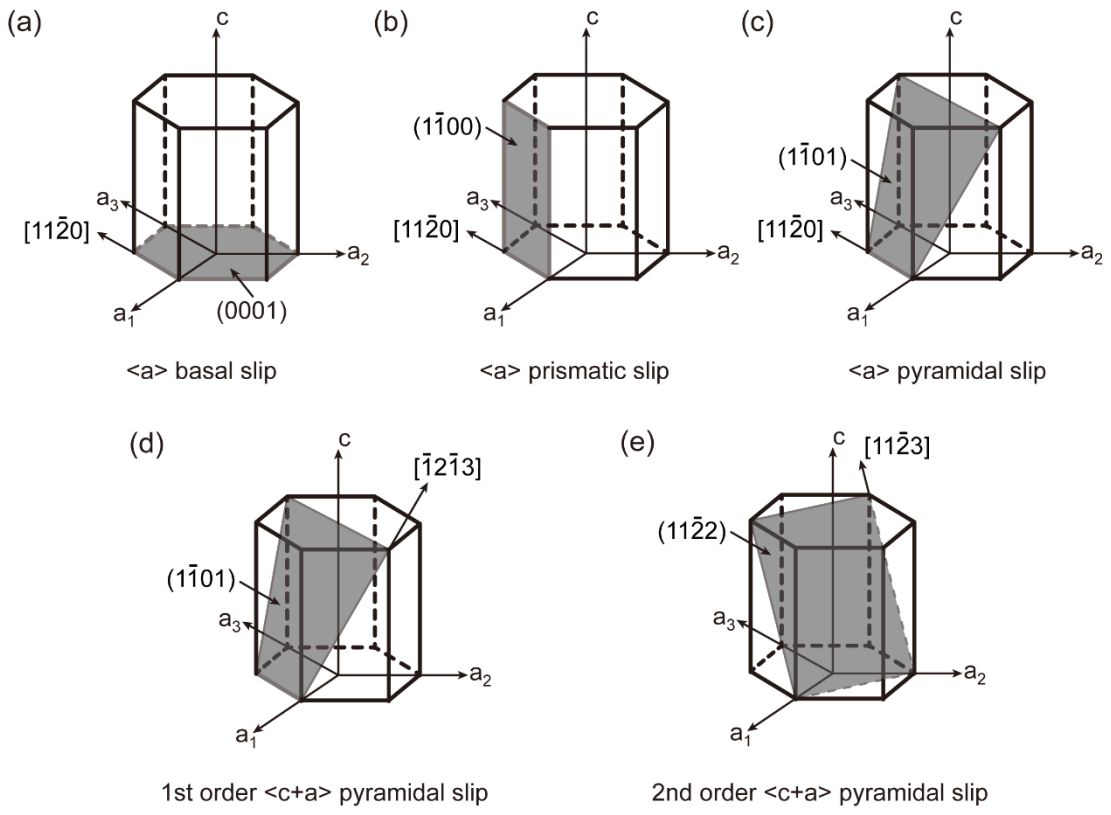


Fig. 2-4. Slip systems in HCP zirconium. Redrawn from (Hasija et al., 2003) with permission from Elsevier.

2.1.3.2. Deformation twinning in HCP zirconium

Deformation twinning is an especially important mechanism in low symmetry crystals. Twinning is defined by the twin plane, which is the mirror plane between the twin and the parent, and the twinning shear direction. Twinning occurs when two separate crystals share some of the same crystal lattice points in a symmetrical manner, and it enables lattice shuffling through coordinated crystal shear with significant lattice reorientation (Christian and Mahajan, 1995). Generally, twinning can be described as a 180° rotation about the normal of the twin plane, or a reflection in the twin plane. In HCP metals, due to the limited number of slip systems, twinning provides deformation parallel to the c-axis which neither <a> prismatic slip nor <a> basal slip can achieve. The main twinning types in zirconium can be classified as contraction (C1, C2) or extension (T1, T2) twins, which accommodate strain to contract or extend the c-axis of a hexagon, respectively as summarised in Table 2-1. The predominant twinning type in zirconium is T1 when the c-axis is under extension at room temperature (Tenckhoff, 1988).

Table 2-1. Twinning types in zirconium (Tenckhoff, 1988; Tong, 2016).

Twin type	**Twin plane**	**Shear direction**	**Shear plane**	**Lattice rotation angle**
T1	$\{10\bar{1}2\}$	$<10\bar{1}1>$	$\{1\bar{2}10\}$	85.22°
T2	$\{11\bar{2}1\}$	$<11\bar{2}\bar{6}>$	$\{10\bar{1}0\}$	34.84°
C1	$\{11\bar{2}2\}$	$<11\bar{2}\bar{3}>$	$\{10\bar{1}0\}$	64.22°
C2	$\{10\bar{1}1\}$	$<\bar{1}012>$	$\{1\bar{2}10\}$	57.05°

During deformation, twinning has a competition with slip. Differing from the dislocations moving in the slip system (along a particular plane in a particular direction), a twinning dislocation can only glide in one-way mode such that the twinning can accommodate shear strain. Twinning contributes to the reorientatioin of the grain as well as slip, and it creates a region of the crystal with a drastically different orientation than the matrix (Clausen et al., 2008).

Twinning has a strong effect on texture and also gives rise to the hardening behaviour in zirconium alloys. The twinning activity and the associated creation of twinning domains inside grains lead to rapid texture evolution (Tome, 1991). Competing with slip, twinning forms during the deformation and affects the texture evolution. Twinning plays the role as barriers to dislocations interpreting the hardening behaviour in hexagonal materials (Abdolvand et al., 2011; Proust et al., 2007). Kaschner et al (Kaschner et al., 2006) elucidate the effect of twinning in the hardening response of zirconium by explaining that twins influence the reload behaviour by either reorienting material for easy slip or by providing barriers to slip.

2.1.4. Blocky alpha in HCP zirconium

Standard tubes made by zirconium alloys in nuclear reactors have 0.57 mm thick walls and a 9.5 mm tube diameter (Macdonald et al., 2014), which is thin enough to minimise neutron absorption and guarantee the efficiency of thermal transformation while thick enough to tolerate high stresses under the working situation. It is desirable to obtain fine, uniform grain size microstructure for the optimal properties of zirconium alloys.

The microstructure is known as ‘blocky alpha’ when the grain size of zirconium alloy is larger than ~300 μm such that it is possible for the ‘blocky alpha’ grains to grow through the tube wall with the thickness mentioned above. Obviously, the ‘blocky alpha’ microstructure should be avoided in industrial applications. ‘Blocky alpha’ microstructure in zirconium was firstly described by Washburn (Washburn, 1964). After that Molodov and Bozzolo (Molodov and Bozzolo, 2010) investigated the effect of magnetic field on the annealing texture and microstructure evolution in cold-rolled (80%) pure zirconium indicating that the magnetic field contributes to an increase in grain growth kinetics and enhances the abnormal grain growth during annealing at 700 °C. Recently, Tong et al (Tong and Britton, 2017) found that when a 2% pre-strain is applied, the grain size of Zircaloy-4 can achieve the nearly 100% ‘blocky alpha’ phase with a grain size of ~470 μm during 800 °C annealing.

2.2. Fatigue fundamentals

Fatigue is defined as a term which ‘applies to changes in properties which can occur in a metallic material due to the repeated application of stresses or strains, although usually this term applies specially to those changes which lead to cracking or failure’ by the International Organisation for Standardization in Geneva (Suresh, 1998). Fatigue is usually associated to the damage and failure under cyclic loading in engineering. The fatigue failure could contribute to a catastrophic accident such that the study of fatigue behaviour is of importance in science and engineering.

2.2.1. Cyclic deformation and fatigue life

Fatigue is generally classified as low-cycle fatigue and high-cycle fatigue with respect to loading conditions. The low-cycle fatigue has a finite endurance of cyclic loading with a significant plastic deformation in each cycle, in which the stress in every cycle is higher than the yield stress of the material, while the stress in high-cycle fatigue is lower than the yield stress and the cycle numbers are commonly larger (> 10^5). Stress controlled and strain controlled cyclic loading, which represent extremes of fully unconstrained and constrained loading conditions respectively, are two commonly loading strategy applied on fatigue test. A 'shakedown' period is observed at the beginning of both stress controlled and strain controlled cyclic loading following with a stable saturation value of strain amplitude and stress amplitude which gives rise to stable hysteresis loops (Mughrabi, 1978). Fig. 2-5 shows the schematic of stable hysteresis loop in cyclic loading.

The monotonic stress-strain curve in ductile materials under uniaxial tension can be characterised by Ramberg-Osgood relationship (Ramberg and Osgood, 1943):

$$\varepsilon = \frac{\sigma}{E} + \left(\frac{\sigma}{A}\right)^{1/n_m} \qquad (2\text{-}2)$$

where E is the Young's modulus, A the monotonic strength coefficient, ε the uniaxial strain, σ the uniaxial stress, and n_m the strain hardening component.

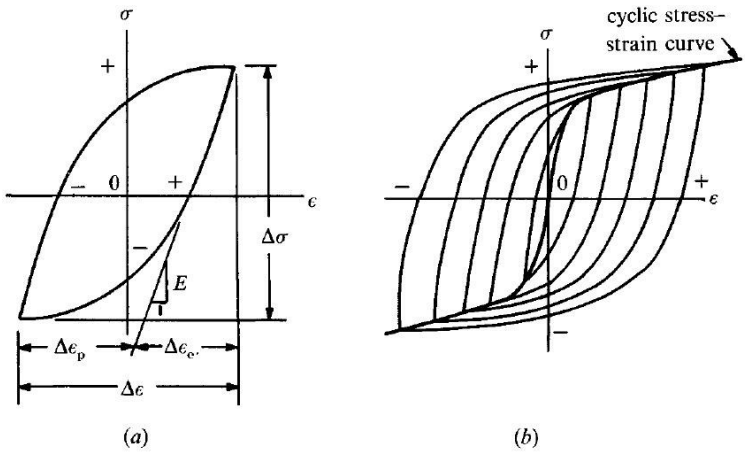


Fig. 2-5. (a) A schematic of a stable hysteresis loop; (b) cyclic stress-strain curve of stable hysteresis loops. Reprinted from (Suresh, 1998).

Cyclic plastic deformation phenomena in low-cycle fatigue may lead to cyclic hardening or softening, Bauschinger effect, strain range effect and ratcheting. In fully reversed stress-controlled cyclic loading the strain amplitude sees a rise (softening) or a reduction (hardening) while in strain controlled cyclic loading the stress amplitude increases (hardening) or decreases (softening). The cyclic hardening or softening is attributed to slip, alloying and precipitation in polycrystalline metals (Brett and Doherty, 1978; Feltner and Laird, 1967a, 1967b). The Bauschinger effect describes the yield strength decrease during reloading in a reverse loading direction (Bauschinger, 1886). In polycrystalline metals, dislocation walls and sub-grain boundaries form during forward loading while rearrange on reversal loading (Hasegawa et al., 1986). This irreversible variation contributes to the Bauschinger effect. Fig. 2-6 shows the schematic of Bauschinger effect in a forward and reverse flow test in which σ_0 is the yield stress and E the Young's modulus.

In stress-controlled low-cycle fatigue the yielding results in progressive plastic strain accumulation, known as ratcheting behaviour (Hassan and Kyriakides, 1994). The ratcheting behaviour which accounts for loading history, mean stress and stress amplitude, has a significant influence on fatigue life (Jiang and Sehitoglu, 1994a, 1994b; Paul et al., 2010). Ratcheting strain increases progressively with cyclic loading (Kang, 2008). It is found that the rate of ratcheting increases in a cyclic softening material while decrease in a cyclic hardening material (Hassan and Kyriakides, 1994). Ratcheting strain was considered as a driving force for fatigue crack growth in a nickel alloy based on the simulation work from Tong et al (Tong et al., 2013). The following experimental work presented an in-situ measurement on ratcheting strain evolution ahead of a stationary crack-tip of a stainless steel under cyclic loading at room temperature by DIC (Tong et al., 2015).

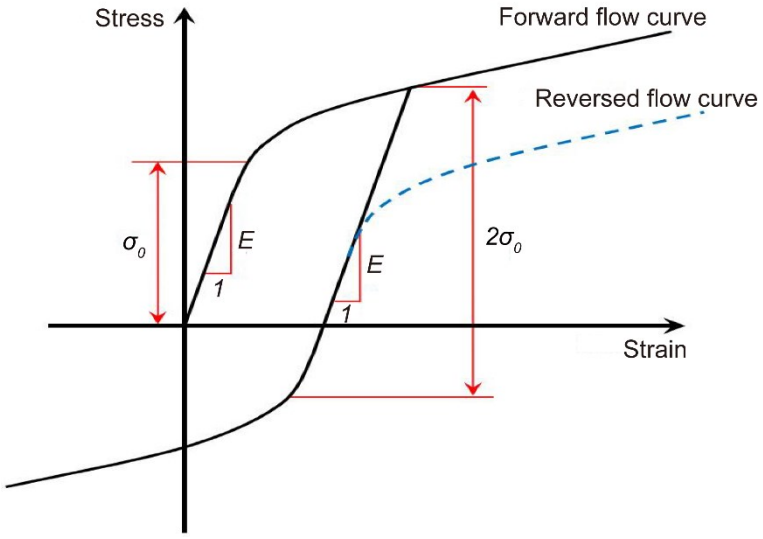


Fig. 2-6. Schematic of Bauschinger effect showing the stress-strain curve in a forward and reverse flow test. Redrawn from (Paul et al., 2011) with permission from Elsevier.

The fatigue life is described as the total number of cycles to fail material under fatigue loading. It is the sum of the cycles to initiate a crack and the cycles spent for dominant crack growth to final failure. In this section the continuum approaches to estimate the total fatigue life are reviewed with both cyclic stress-based and strain-based method.

The stress-based and strain-based approaches to fatigue are found widely used in industrial applications. The first stress-based approach to fatigue was firstly introduced by Wöhler (Wohler, 1860), known as the *S*-*N* curve or the Wöhler curve, which plots nominal stress amplitude *S* versus cycles to failure *N* is used to describe the fatigue performance in high-cycle fatigue. The *S*-*N* curve can be expressed as a power law relation as

$$N_1 = N_2 \left(\frac{S_1}{S_2}\right)^{\frac{1}{b}} \qquad (2\text{-}3)$$

where S_1 and S_2 are the stress amplitude, N_1 and N_2 the cycles to failure, b the Basquin slope of the power law equation, which is used to calculate the cycles to failure for a known stress amplitude (Basquin, 1910). In low-cycle fatigue when considerable plasticity occurs, for example, high stress amplitudes or stress concentrations, the fatigue life is greatly shortened. In the light of significant role of plastic strain in fatigue, Coffin (Coffin, 1954) and Manson (Manson, 1954) independently proposed a plastic strain-based approach. The Coffin-Manson relation to low-cycle fatigue, given by

$$N_f^{\beta} \Delta\epsilon_p = C \qquad (2\text{-}4)$$

where N_f is the number of cycles to failure, β the constant with respect to the material,

$\Delta\epsilon_p$ the plastic strain range, and C a constant related to fracture ductility of the material.

The empirical relations mentioned above are appropriate to describe fatigue life under fully reversed cyclic loads where the mean stress, is zero. However, the mean stress is not zero in most engineering applications, and it is found to play an important role in fatigue life. The effect of mean stress in fatigue can be represented by constant fatigue life relations such as the Goodman relation (Goodman, 1899) where combinations of the stress amplitude and mean stress offers a constant fatigue life. Another method to estimate fatigue life is based on accumulative damage. The Palmgren-Miner rule assumes the fatigue to be a linear damage accumulation process in which the failure occurs when the sum of the damage from each load reaches a critical value (Miner, 1945; Palmgren, 1924).

2.2.2. Mechanistic studies of fatigue crack nucleation

The fatigue life consists of the total cycles for crack nucleation and crack growth to failure in which the former takes a large proportion of the total fatigue life. The fatigue crack nucleation is considered to be an incubation process for crack formation to the size scale which can be physically observed depending on applications. The original mechanism of crack nucleation was proposed by Wood (Wood, 1958) who postulated that the cyclic straining results in 'to-and-fro' fine slip movements along the fatigue slip bands and leads to 'roughening' of the material surface, which finally contributes to fatigue crack nucleation. Forsyth (Forsyth, 1953) firstly reported the experimental observation of 'exuded ribbons' on the electropolished sample surface in an Al-Cu alloy

during cyclic deformation, which is considered to be the slip-induced surface roughening. More experimental evidence showed that the surface roughening such as the intrusion-extrusion pair was considered to be the omen of crack initiation (Cottrell and Hull, 1957). The surface roughening occurs when the average dislocation distance reaches the critical distance for dislocation annihilation. A dipole with opposite sign edge dislocations annihilates to form a vacancy resulting in surface roughening (Essmann et al., 1981).

The surface roughening are attributed to the slip irreversibility in persistent slip bands (PSBs) (Brown, 2013; Ho et al., 2015; Man et al., 2009). PSB is well known to play the key role in fatigue crack nucleation. Early observation of PSBs in fatigue can trace back to the work reported by Ewing & Humfrey (Ewing and Humfrey, 1903) and Gough (Gough, 1933) showing the cyclic deformation was concentrated on slip bands or shear bands and the fine cracks developed at these slip bands. The term 'PSB' was first used by Thompson et al (Thompson et al., 1956) who suggested that the PSBs had distinct microstructures with surrounding matrix materials by observing PSBs on the electropolished metal surface. Fig. 2-7 shows the schematic of PSB in a polycrystalline microstructure. Cyclic loading results in strain localisation on slip bands with the increase of dislocation density (Cheng and Laird, 1981). The dislocations agglomerate into the wall structure inside the PSB, as a consequence of PSBs being softer than the matrix material (Sangid et al., 2011a). During the cyclic loading the hardened matrix material results in abrupt strain gradient along the interface between PSB and matrix, where the fine crack prefers to form (Ma and Laird, 1989a, 1989b). The energy criterion

was proposed to associate the fatigue crack nucleation to the total energy related to PSB formation (Sangid et al., 2011a). Recent studies focused on the interaction between grain boundary and PSB gave rise to an energy-based criterion of PSB structure for crack nucleation (Sangid et al., 2011b).

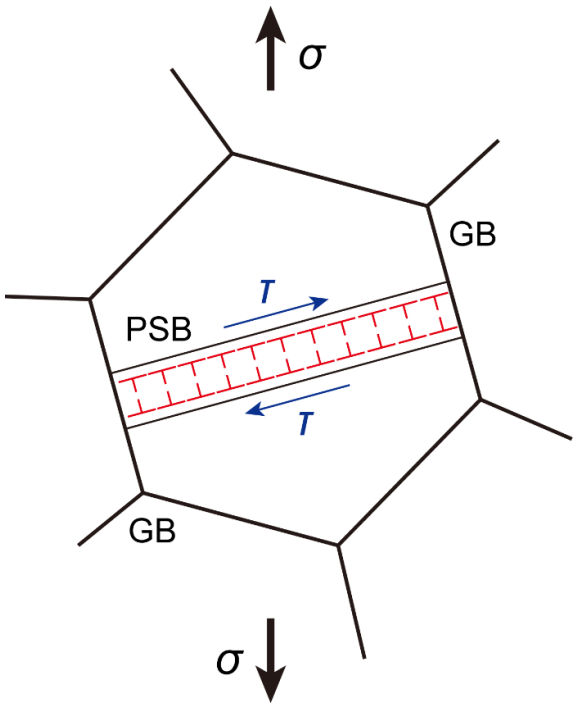


Fig. 2-7. Schematic of persistent slip bands (PSBs) structure in polycrystal. Redrawn from (Sangid et al., 2011b) with permission from Elsevier.

2.2.3. Mechanistic studies of fatigue crack growth

After a period of incubation, crack forms to the size which can be physically observed, and grows with continuous cyclic loading. Generally, fatigue crack growth is defined as three stages as shown in Fig. 2-8. Stage I indicates the crack with the length less than the width of several grains, which is also termed as a short crack. The short crack is sensitive to the microstructure. The main subject of this thesis is focused on short crack

growth. More details of short crack will be reviewed in the next section. Stage II shows a linear log-log relation between crack growth rate (*da/dN*) and stress intensity factor range (ΔK), known as Paris law. (Paris and Erdogan, 1963): The crack growth rate for materials under cyclic stress is a function of the stress intensity factor *K* (mode I) of fracture mechanics:

$$\frac{da}{dN} = A\Delta K^m \qquad (2\text{-}5)$$

where $\frac{da}{dN}$ is fatigue crack growth rate, ΔK is stress-intensity factor range ($\Delta K = K_{max} - K_{min}$). *A* and *m* are constants with respect to the materials, environment, stress ratio and other factors. The stress intensity factor *K* characterises the stress conditions at the crack tip for a linear elastic material. The stage II crack growth is mainly related to the remote loading while the local microstructures have little effect on the crack growth rate. Stage III refers to an instable period with the crack closed to the final fracture.

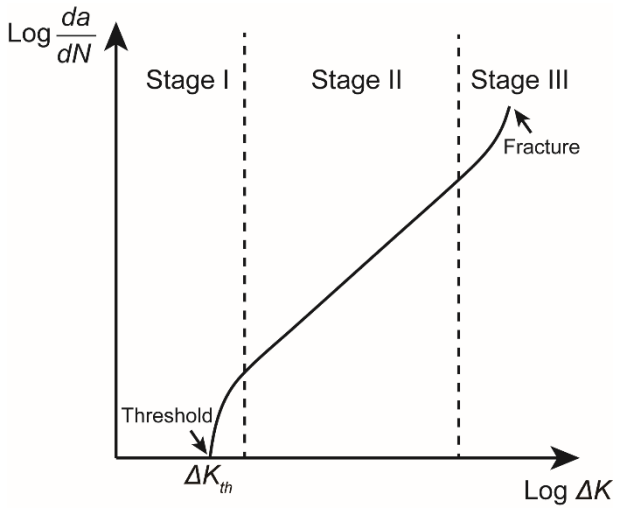


Fig. 2-8. Schematic of fatigue crack growth stages. Redrawn from (Anderson, 1996).

The first experimental evidence for stress concentration was from Inglis's (Inglis, 1913) analysis on elliptical holes in flat plates. The stress applied on the crack is thought to be the key factor to create fracture surfaces. In an atomic view, fracture occurs when the stress applied at the atomic level is large enough to create two fracture surfaces by breaking the atom bonding. Griffith (Griffith, 1921) firstly proposed fracture surface energy to describe the crack growth suggesting that the crack growth occurs when the energy released on fracture reaches the surface energy created. Consider a plate which contains a crack with length of $2a$ (the plate width $\gg 2a$), The Griffith energy balance is given by

$$\sigma_f = \sqrt{\frac{2E\gamma_s}{\pi a}} \qquad (2\text{-}6)$$

where γ_s is the surface energy, σ_f the fracture stress and E Young's modulus. It is important to note that γ_s represent the surface energy of one fracture plane with two in total. This equation is valid when cracking in an ideal brittle material, however, it is found that this relation is not reliable when applied to ductile materials such as metals. Irwin (Irwin, 1948) and Orowan (Orowan, 1948) independently modified the Griffith energy balance considering the plasticity in fracture, which is given by

$$\sigma_f = \sqrt{\frac{2E(\gamma_s+\gamma_p)}{\pi a}} \qquad (2\text{-}7)$$

where γ_p is the plastic work per unit area of fracture surface. Later Irwin (Irwin, 1956) proposed energy release rate to measure the energy available for crack advance. The energy release rate approach is essentially equivalent to the Griffith energy model. The

energy release rate is a derivative with respect to the rate of change in potential energy, which is supplied by the internal strain energy and external forces. The energy release rate for a wide plate with a crack of length *2a* under plane stress condition is expressed as

$$G_r = \frac{\pi a \sigma^2}{E} \qquad (2\text{-}8)$$

where σ is the remote loading stress, E the Young's modulus and a half of the crack length. The energy release rate was considered to be the crack driving force as it describes the rate of the potential to drive the crack advance.

As the most widely used crack driving force, the stress intensity factor is defined based on the stress state at the crack tip (Irwin, 1957; Tada et al., 1973). A crack can have three types of loading on behalf of the global loading condition as shown in Fig. 2-9. Mode I loading is the loading condition in which the principal load is applied normal to the crack plane (surface) opening the crack. Mode II and Mode III corresponds to in-plane and out-of-plane shear loading respectively. A crack can be loaded in any one of these modes, or a combination of two or three modes.

The stress intensity factor is only valid for isotropic materials under a linear elastic fracture mechanics (LEFM) condition. Apparently, LEFM is not applicable to plastic deformation in ductile materials such that the stress intensity factor is not appropriate to use with plasticity considered. Two elastic-plastic parameters, J-integral and crack-tip-opening displacement (CTOD) were applied to describe crack growth with plasticity.

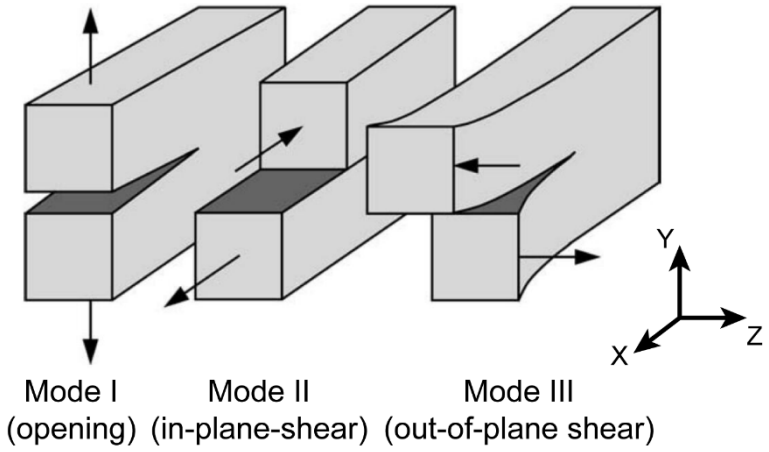


Fig. 2-9. Schematics of loading modes at cracks. Redrawn from (Anderson, 1996).

The opening at the crack-tip as a measure of fracture toughness was proposed by Wells (Wells, 1961). Wells noticed that the opening initial sharp crack under cyclic loading was blunted due to crack-tip plasticity as illustrated in Fig. 2-10. The crack blunting was found to be proportional to the toughness such that the CTOD was used to characterise the crack growth. CTOD was related to the stress intensity factor by solving the displacement at the physical crack tip in the limit of small-scale yielding, which is given by (Irwin, 1961)

$$\delta = \frac{4}{\pi}\frac{K_I^2}{\sigma_{YS}E} \qquad (2\text{-}9)$$

where δ is CTOD, E Young's modulus, K_I mode I stress intensity factor and σ_{YS} yield stress.

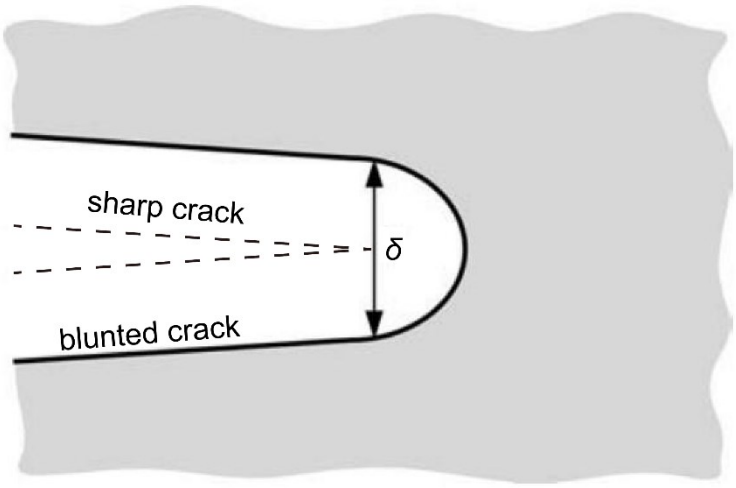


Fig. 2-10. Schematic of crack-tip blunting. Redrawn from (Anderson, 1996).

Another measure of the driving force for crack growth is J-integral. The J-integral was introduced by Rice (Rice, 1968) as a path-independent contour integral for the analysis of cracks. In the nonlinear elastic condition, where the material unloads along the same loading path as it was loaded, the J-integral is equal to the energy release rate. Consider an arbitrary path Γ around a crack-tip. The J-integral is given by

$$J = \int_{\Gamma} \left(wdy - T_i \frac{\partial u_i}{\partial x} ds\right) \qquad (2\text{-}10)$$

where w is strain energy density, T_i traction vector components, u_i displacement vector components and ds length increment along the contour Γ. The strain energy density w is expressed as

$$w = \int \boldsymbol{\sigma} d\boldsymbol{\varepsilon} \qquad (2\text{-}11)$$

where $\boldsymbol{\sigma}$ and $\boldsymbol{\varepsilon}$ are the stress tensor and strain tensor., and T_i is given by

$$T_i = \boldsymbol{\sigma} n_j \qquad (2\text{-}12)$$

where n_j are the components of the unit vector normal to the path Γ. As mentioned above, the J-integral is independent on the path Γ, and uniquely characterises the stress and strain at the crack tip (Hutchinson, 1968; Rice and Rosengren, 1968).

The stress intensity factor, CTOD and J-integral are traditional single-parameter driving forces for crack growth with prominent limitations. The stress intensity factor is only valid in homogeneous linear elastic fracture mechanics although it has been widely employed beyond its limitation in practice. The J-integral has enjoyed a great success in describing the crack growth in elastic and small-scale yielding material. Both CTOD and J-integral provide a measure of the driving force with plasticity; however, they are only valid in homogeneous materials without considering material anisotropy, not to say local microstructures such that they are reasonable to be used in study of long crack growth but largely confined to be applied on microstructural-sensitive short crack growth.

2.2.4. Microstructurally-sensitive short crack and its driving force

Short cracks with a size on the order of several grains propagates at the driving force level such as stress intensity factor is significantly below the threshold for long crack growth (El Haddad et al., 1979). It is worthy to clarify the definition of short crack including microstructural-sensitive short crack and physically short crack. The latter is sufficiently large to smear out the influence of local microstructures but be affected

more by the remote loading. In this study, we mainly focus on the microstructurally-sensitive short crack which is termed as ‘short crack’ for convenience. Short cracks commonly grow crystallographically following specific slip planes (Pineau et al., 2016; Suresh and Ritchie, 1984). At the mesoscale local microstructures including grain morphology (Tokaji et al., 1994, 1988), grain boundary (Nakajima et al., 1998) and crystallographic orientation (Blochwitz et al., 2008; Ward-Close and Beevers, 1980) have profound effect on short crack growth. At a smaller length scale the dislocation substructures, slip, and the development of lattice curvature are thought to lead to local interacting with the crack growth (Andersson and Persson, 2004; Wilkinson et al., 2006). However, the substantial understanding on the effect of such smaller scale quantities is not fully established.

Short crack growth presents retardation and deflection when traversing a grain boundary. The retardation is manifested by a crack growth rate decrease or ultimately by becoming stationary at the grain boundary. The grain boundary acts as a barrier to dislocation motion, which results in slip pile-ups and stress concentrations. Zhang and Edwards (Edwards and Zhang, 1994; Zhang and Edwards, 1992) found the plastic zone of the short crack was blocked by a grain boundary which resulted in the crack growth retardation. Navarro and Rios (Navarro and de los Rios, 1988) found that short crack growth rate was a function of the crack-tip position relative to the grain boundary. The grain orientations, especially the misorientation between the adjacent grains were considered to play important role on the interaction between short cracks and grain boundaries. The strength of the interaction between short cracks and grain boundaries

were found to be stronger for larger misorientations between the neighbouring grains (Tanaka et al., 1986). Grain boundaries with higher misorientations, on average, result in larger deflections and retardations (Gao et al., 2007). Zhai et al (Zhai et al., 2000) proposed a crystallographic mechanism model to explain the crack deflection at the grain boundary, suggesting that the twist and tilt angles of the crack plane deflection are the key factors accounting for the short crack growth path and rate rather than the lattice misorientation between the two neighbouring crystals. In this model, twist and tilt are the angles between the traces of the two slip planes on the boundary plane and the sample surface respectively. A large twist angle of the crack plane deflection at the grain boundary results in a higher resistance to short crack growth while a low twist angle leads to the opposite consequence (Zhai et al., 2005). A two-dimensional observation on a surface crack has a drawback that the sub-surface information of short crack and local microstructures are not accessible. Fortunately, more advanced characterisation techniques have been applied to obtain a 3D morphology of short cracks in recent years giving rise to further understanding on the short crack growth behaviours. The development of focused ion beam (FIB) tomography with 3-D reconstruction offered the possibility to carry out the 3D characterisation of the crack growth behaviour across a grain boundary. Holzapfel et al (Holzapfel et al., 2007) studied the retardation of short crack growth by the interaction with a grain boundary decorated by carbide precipitates. Their results showed that the carbide precipitates lead to a significant suppression of crack growth. Schaef et al (Schaef et al., 2011) presented detailed data of short crack growth rate coupled to grain boundary position. They found

both the inclination angle between the active slip systems and the inclination angle of the grain boundary determines the interaction between microcracks and grain boundaries. X-ray diffraction contrast tomography (DCT) and synchrotron X-ray give rise to non-destructive characterisation on short crack. Recently King et al (King et al., 2011) used DCT and Synchrotron microtomography to carry out 3D in-situ observation of short crack growth in magnesium. In this work, a short crack was observed to be retarded at grain boundaries with large misorientations of the basal slip plane. The interactions between the short crack and grain boundaries could be explained by Zhai's tilt-twist model.

The driving force for short crack growth is still a challenging task in the study of fatigue because of its uncertain crack behaviour and complicated mechanism. The traditional single-parameter driving force for fatigue crack growth including stress intensity factor, CTOD and J-integral cannot correlate the microstructurally sensitive short crack growth under multiaxial conditions due to the local microstructures. McDowell and Dunne (McDowell and Dunne, 2010) suggested the computable Fatigue Indicator Parameters (FIPs) based on cyclic plastic strain range and cumulative ratchetting deformation as a method of correlating the local microstructure. The most commonly used FIP is the Fatemi-Socie parameter (Fatemi and Socie, 1988) which is given by

$$FIP_{FS} = \Delta\gamma^{p}_{max}(1 + k\frac{\sigma_n}{\sigma_y}) \qquad (2\text{-}13)$$

where $\Delta\gamma^{p}_{max}$ is the maximum plastic shear strain range, σ_n the peak normal stress on the maximum plastic shear range plane, σ_y the yield stress, and k a constant

commonly between 0.5 and 1. The Fatemi-Socie parameter correlates well on short crack growth in ductile materials under multiaxial loading conditions (Fatemi and Kurath, 1988). Castelluccio and McDowell (Castelluccio and McDowell, 2012) proposed a nonlocal (volume averaged) Fatemi-Socie-FIP-based model in a single crystal indicating the correlation of the cyclic crack-tip displacement with γ_{max}^{p} averaged within slip bands adjacent to the crack-tip. Although the FIP-based model provides a useful quantitative characterization of fatigue life (Musinski and McDowell, 2012) and short crack growth rate (Shamsaei and Fatemi, 2014), it is not a measurable physical quantity relating to local microstructures.

The localised energy required to drive a growing crack is considered to relate to dislocation structure such that the mechanistic foundation for a driving force should involve the contribution of dislocations (Wilson et al., 2018). Wilkinson and Roberts (Wilkinson and Roberts, 1996) proposed a model suggesting that the short crack-tip sends out interstitial dipoles in the materials on two parallel slip planes, and grows by absorbing vacancy dipoles. The stored energy density introduced by (Wan et al., 2014) and (Chen et al., 2018) has enjoyed great success in capturing crack nucleation site in a range of ductile materials. More recently, Wilson et al (Wilson et al., 2019, 2018; Wilson and Dunne, 2019) utilised stored energy density as a driving force simulating short crack growth within a crystal plasticity finite element (CPFE) model. The stored energy density is expressed as

$$G = \int \frac{|\xi \boldsymbol{\sigma} : d\boldsymbol{\epsilon_p}|}{\sqrt{\rho_{SSD}+\rho_{GND}}} \qquad (2\text{-}14)$$

where ρ_{SSD} and ρ_{GND} are the statistically stored dislocation and geometrically necessary dislocation density, $\boldsymbol{\sigma}$ stress tensor, $\boldsymbol{\epsilon_p}$ plastic strain tensor and ξ the fraction of plastic deformation work stored in the material which is assumed to be constant at 5% during fatigue process. Fig. 2-11 shows the schematic of the short crack growth driven by stored energy. Mechanistically, when the crack grows the stored energy is released from a dislocation by creating new crack surfaces.

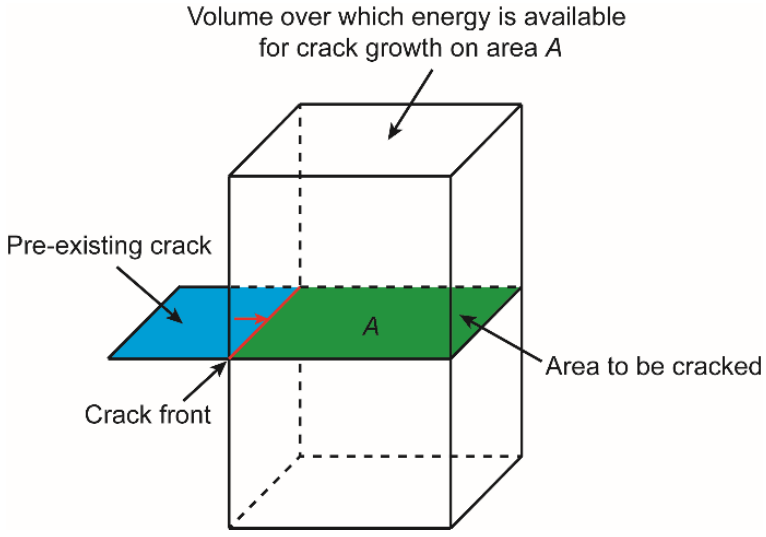


Fig. 2-11. Schematic of the stored energy density as driving force for short crack growth.

2.2.5. Fatigue crack study in zirconium

Fatigue crack in zirconium and zirconium alloys has been extensively studied in the recent decades. Experimental studies on Zircaloy-2 show the low-cycle fatigue behaviour correlates well with the Coffin-Manson relation in the temperature range from 20 °C to 400 °C (Pandarinathan and Vasudevan, 1980; Pettersson, 1975). The fatigue behaviour in zirconium is temperature dependent. Zircaloy-2 shows fatigue strengthening due to dynamic strain aging between 20 °C and 300 °C, however, the

fatigue life decreases in higher temperature range from 300 °C to 700 °C (Snowden and Stathers, 1977). Zircaloy-4 shows abnormal cyclic hardening in the temperature range from 300 °C to 400 °C is attributed to dynamic strain aging with increasing rate of dislocation accumulations (Armas et al., 1996). The deformation mechanism on fatigue behaviour in zirconium has been explored by microstructural characterisation. Pure zirconium shows planar slip whereas Zircaloy-4 shows wavy slip in high-cycle fatigue because alloying additions improve the stacking fault energy and hence facilitate the formation of cross-slip and dislocation networks (Lin and Haicheng, 1998). On the other hand, twinning is argued to facilitate fatigue damage in alpha-zirconium (Warren and Beevers, 1970), and is observed coupling with fatigue crack growth around the crack-tip in zirconium (Kerr et al., 2010).

Zirconium and zirconium alloys are extensively used as fuel claddings and pressure tubes in high temperature water cooled nuclear reactors. The environmentally induced problems have arisen during the industrial use. Delayed hydride cracking (DHC) is the most common one among those which is caused by hydrides in zirconium alloys including $ZrH_{0.5}$-ζ, ZrH-γ, $ZrH_{1.5\text{-}1.7}$-δ, and ZrH_2-ε (Bair et al., 2015). The hydrides precipitate in zirconium alloy when H atoms are constantly absorbed from water during the operation in a nuclear reactor, which results in embrittlement through the DHC process (Cox, 1990). On the mechanism of DHC, hydrides precipitate and grow at the crack-tip due to the stress concentration by hydrogen diffusion along the stress field (Dutton et al., 1977; Puls, 1990). The pre-existing crack-tips move ahead with the brittle hydrides fracture under applied cyclic load. The formation of a new crack-tip leads to

a new surrounding stress field driving the precipitation of more hydrides and then the process repeats (Cann and Sexton, 1980).

2.3. Summary

HCP zirconium displays strong anisotropy in deformation due to the low availability of slip systems including prismatic, basal and pyramidal slip. To favour the deformation of HCP zirconium along the c-axis, twinning plays an important role in plastic deformation. The compressed zirconium usually acquires a strong basal texture which greatly effects the mechanical properties.

Fatigue studies on zirconium and its alloys have historically focused on life estimation, including studies of the macro mechanical responses with cyclic loading. The investigation of microstructurally-sensitive short crack in zirconium has rarely been reported. Although numerous studies have explored the effect of local microstructures on microstructurally-sensitive short crack growth in HCP alloys, to date, no detailed crack growth data has been reported upon the interaction between crack growth rate and local microstructure. For the understanding on the mechanism of short crack growth, the measurement of the micro-scale mechanical quantities including local stress, local strain and dislocation density around the crack-tip, which are essential to the driving force for short crack growth, have not been discovered due to the challenge of experimental design.

The global approach on describing fatigue crack growth has been well established in

recent decades. Stress intensity factor under LEFM condition and J-integral coupling with CTOD under small scale yielding have enjoyed great success in describing long crack growth as a measure of driving force. However, such single-parameter indicators are not reliable to characterise microstructurally-sensitive short crack growth. It is well known that a large proportion of the fatigue life of an engineering component is associated with short crack growth. From a scientific standpoint, developing a quantitative understanding of short crack growth must be regarded as one of the most important task. Stored energy density involving all the important micromechanical quantities (stress, strain and dislocation density) is a possible driving force for short crack growth, which is truly microstructurally sensitive.

In this study, substantial experimental data of short crack growth in a textured Zircaloy-4 have been collected. The crack growth rate and crack path of short crack interacting with local microstructures, e.g. crystallographic orientation, slip activation and twinning, have been addressed. Based on the features observed on short crack growth, experimental measurement of stored energy density in the crack-tip area in fatigue short crack growth have been fulfilled by an in-situ DIC technology coupling with EBSD examination. The validation of stored energy density as a reliable driving force for short crack growth has been discussed.

3. Microstructure-interacting short crack growth in blocky alpha Zircaloy-4

3.1. Introduction

Understanding microstructure-sensitive fatigue crack growth in structural materials offers the potential to prevent fatigue failure in engineering components which may lead to catastrophic accidents. Extensive study of fatigue crack growth has been carried out over many decades. Paris Law (Paris and Erdogan, 1963) sought a relationship between fatigue crack growth rate and the stress intensity range for Stage II cracks. This relationship has been validated by numerous experiments. Elber et al (Elber, 1970) suggested fatigue crack closure required the modification of the Paris Law, and studied the effect of plastic strain accumulation around the crack tip. However, when the crack length is small and at the microstructural level, the stress intensity factor determined macroscopically, ΔK, is no longer reliable to describe fatigue crack growth because the microstructure has a strong effect on local stress state resulting from crystallographic elastic anisotropy, adjacent grain constraint effects, and slip localisation (Morris, 1980; Morris et al., 1981; Pineau et al., 2016; Tanaka et al., 1986). As a result, the mechanisms of fatigue crack growth at the microscale are still an important and active area of research.

A dual-stage process of fatigue crack growth was introduced by Forsyth (Forsyth, 1963). It was proposed that in Stage I fatigue cracks prefer to grow along crystallographic slip planes, driven by maximum shear stress. Stage I cracks, or short cracks, are at a length

of up to several grains. Short cracks have been classified as microstructurally and mechanically short by Tokaji et al (Tokaji et al., 1987) who reported that mechanically short crack propagation mainly follows the plastic blunting mechanism, and was argued to be less affected by microstructure compared with microstructurally short cracks. Kitagawa and Takahashi (Kitagawa and Takahashi, 1976) proposed a diagram, known as KT diagram, for fracture mechanics. The KT-diagram, which combines the fatigue crack growth threshold and the fatigue endurance limit into a single plot, has been widely used to predict the allowable stress range for infinite life (Aigner et al., 2019; Ciavarella and Monno, 2006; Maierhofer et al., 2015; Zerbst et al., 2016). El Haddad et al (El Haddad et al., 1979) introduced an intrinsic crack length based on the KT-diagram to predict threshold stress for short crack growth. Chapetti (Chapetti, 2003) defined a microstructural threshold as a function of crack length for short cracks. In this model, the physically short crack behaviour was obtained from the long crack growth, introducing the reduced threshold due to unsaturated crack closure. Based on Chapetti's model, Santus et al (Santus and Taylor, 2009) introduced ΔK for physically short cracks, offering a tool to describe the behaviour but without full mechanistic understanding.

Dislocation mechanics based models have been proposed to predict the conditions required for short crack growth threshold and the effect of microstructural features. In the near threshold regime short cracks often grow along crystallographic planes that are inclined to the principal load axis which results in a shear mode stress state at the crack tip. Tanaka et al (Tanaka and Mura, 1981) investigated the effect of grain size and crack length on the threshold condition of fatigue growth of short cracks. This model is based

on the assumption that the threshold condition is determined by the blockage of the crack-tip slip band on a grain boundary. Wilkinson et al (Wilkinson et al., 1998) studied near the threshold condition for fatigue crack propagation, and introduced a short crack propagation model in which the crack tip sends out interstitial dipoles into the material on two parallel slip planes, and propagates by absorbing vacancy dipoles. They also found that the threshold cyclic stress intensity, ΔK_{th} increases when the load ratio decreases.

Short cracks are thought to be sensitive to local microstructure. Retardation and deflection commonly occur when the crack approaches and traverses a grain boundary and the latter has a strong effect on short crack growth rate and crack path. The retardation is reflected by the decrease of crack growth rate or ultimately by becoming stationary at the grain boundary. The latter is attributed to slip-blockage at the grain boundary, until the local stress rises to drive the crack tip forward and across the boundary. Hansson et al (Hansson and Melin, 2010) studied the grain boundary influence on short fatigue crack growth rate by assuming that the short cracks grow in a single shear mechanism due to nucleation, glide and annihilation of discrete dislocations. They found that both the grain boundary configuration (predominantly grain misorientation and grain size) and distance from the crack to a grain boundary have an influence on crack growth rate.

When cracks traverse a grain boundary the deflection angle is highly affected by the misorientation between the grains adjacent to the grain boundary. Zhai et al (Zhai et al.,

2000) sought to explain the crack deflection and retardation at a grain boundary based on the tilt and twist angles between the crack paths in the two grains. However, this model underestimates the effect of the slip plane on the crack path. For low-symmetry hexagonal close-packed (HCP) alloys such as titanium, zirconium and magnesium, the slip systems are expected to have a stronger effect on crack path and crack growth rate. Marrow et al (Marrow et al., 2014) used serial block face scanning electron microscopy (SBFSEM) to provide three-dimensional characterisation of short crack shape in magnesium. The results from Marrow and co-workers suggested that basal planes dominate the fracture planes and the tilt and twist of the basal plane at a grain boundary or twin interface are important factors for fatigue crack growth rate.

Multiple advanced techniques have been applied to quantify short crack behaviour. Digital image correlation (DIC) offers quantification of strain distributions in the crack tip region. Carroll and co-workers (Carroll et al., 2013) applied high resolution DIC to measure the strain accumulation in long fatigue crack growth in a nickel-based alloy. Very recent experimental work (Malitckii et al., 2018) focused on the strain accumulation during microstructurally short crack propagation in a bcc Fe-Cr ferritic stainless steel. By using HR-DIC to measure the strain field, they found that the shear strain accumulation has significant influence on the crack growth.

This chapter is focused on microstructurally short crack growth in ‘blocky alpha’ Zircaloy-4, which has large grain size of ~400 μm. The large grain microstructure facilitates the study of the crack growth behaviour intragranularly and at the grain

boundaries using quantitative characterisation. Full-field investigations using OM, SEM, DIC and EBSD techniques provide rich data with which to investigate the mechanistic basis of short crack growth including the grain orientations and morphologies with respect to crack path, crack growth rate and twinning. In the following sections, materials characterisation and experimental methods are introduced. This is followed by the assessment of the effects of microstructure (crystallography, grain boundaries, texture) on short crack growth in blocky alpha Zircaloy-4, and includes analysis of crack path direction, tortuosity and rate of growth.

3.2. Materials and Methods

3.2.1. Texture

The as-received Zircaloy-4 provided by Rolls-Royce plc. was in the form of hot-rolled and recrystallized plate (around 3 mm in thickness). Electron backscatter diffraction (EBSD) was utilised to quantify grain orientations of the as-received Zircaloy-4 plate as shown in Fig. 3-1. Fig. 3-1 (a) shows the scanned grain map containing around 4300 grains. The average grain size was found to be 13.5 μm. Fig. 3-1(b) shows the inverse pole figure (IPF) in the Y-direction, and Fig. 3-1 (c) the pole figures along {0001}, $\{10\bar{1}0\}$ and $\{11\bar{2}0\}$. The as-received Zircaloy-4 plate displays strong basal texture as the c-axis [0001] direction is predominantly aligned parallel to the normal direction.

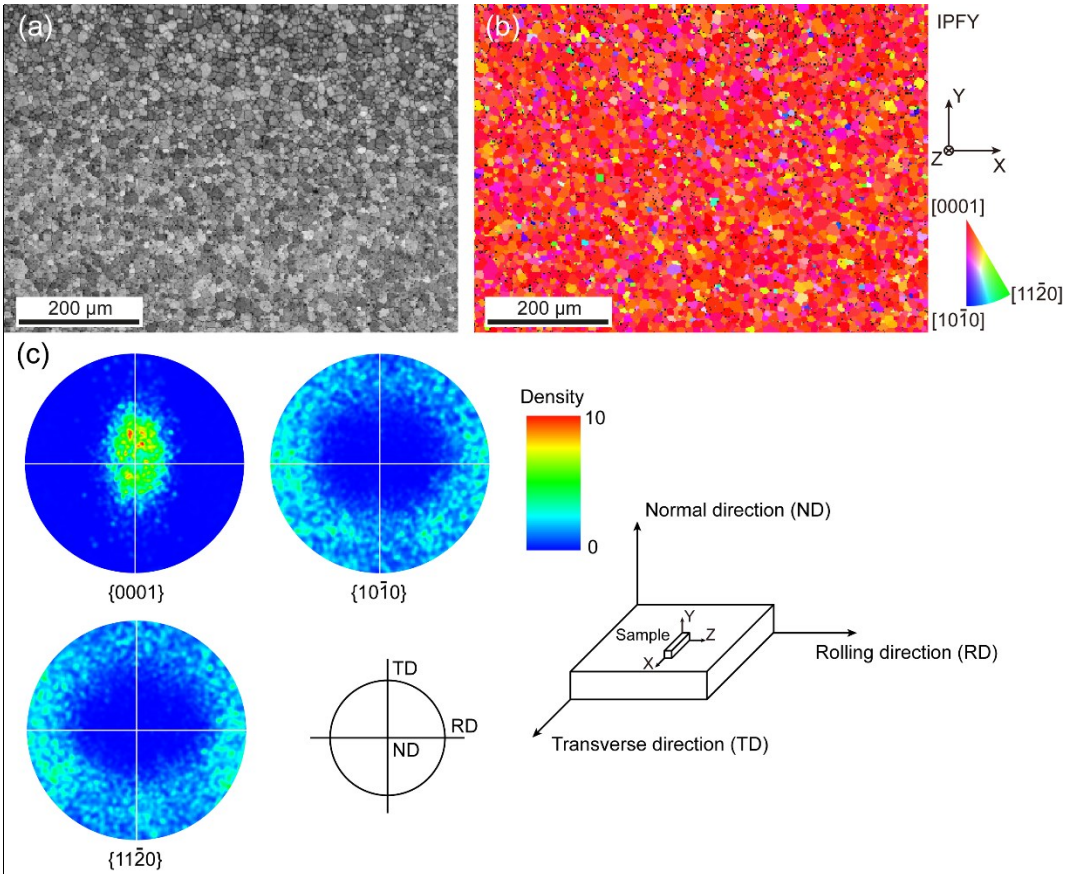


Fig. 3-1. (a) SEM image of as-received Zircaloy-4 grain map; (b) inverse pole figure in the Y-direction; (c) pole figure showing the grain orientations in the area of (a)/(b).

3.2.2. Blocky alpha

Square section samples were heat treated at 800 °C for 2 weeks to generate large (ie of order 400 μm) grains known as 'blocky alpha'. Independent studies on fine-grained Zircaloy-4 suggest that grains grow to blocky alpha with the driving force provided by stored strain energy (Tong and Britton, 2017). This strain energy can come from rolling deformation or anisotropic thermal expansion strain for the as-received Zircaloy-4 plate. Fig. 3-2 shows the fine-grain microstructure before and the blocky alpha microstructure after heat treatment. The grain size increases from around 10 μm to over 400 μm, with

a few remaining small grains. Additionally, the IPFZ images shown in Fig. 3-2 (b) and (d) indicate that the blocky alpha microstructure inherits the basal texture from the fine-grain microstructure.

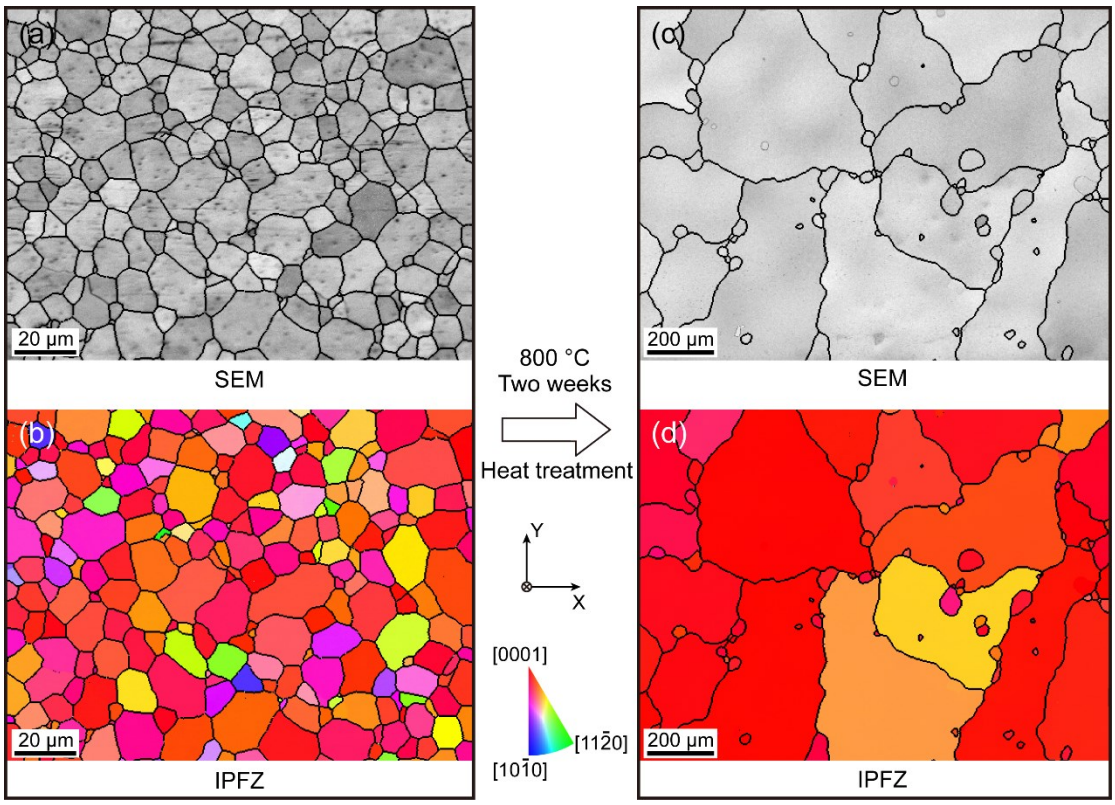


Fig. 3-2. (a) SEM image and (b) IPFZ image showing the grain map in as-received fine-grain Zircaloy-4 before heat treatment; (c) SEM image and (d) IPFZ image showing the grain map in large-grain (blocky alpha) Zircaloy-4 after heat treatment.

3.2.3. Three-point bend testing

Three-point bend testing was designed to apply cyclic loading to blocky alpha Zircaloy-4 beam samples A, B, C, D and E. The as-received Zircaloy-4 plate was cut into beam shape samples with dimensions of approximately 12 × 3 × 3 mm^3 by electrical discharge machining (EDM). After that an edge notch was prepared at the bottom centre of each

beam shown in Fig. 3-3 (a) and (b), which is introduced to localise the nucleation of cracks to enable their short growth behaviour to be studied. In the three-point bend testing, force controlled cyclic loading was applied on the top of the beam as shown in Fig. 3-3 (c), (d) and (e), with R-ratio of 0 (ie zero to peak to zero). The distance between the two fixed supporting pins was 10 mm, the latter having a radius of 1.5mm. The clearance at first loading between the sample base and the lower part of the sample holder was > 5 mm.

The geometries of the beam samples and the loading conditions including the applied maximum force at the top and the calculated maximum stresses at the base of the beam samples are detailed in Table 3-1. These loads give rise to stress intensities (ΔK) with a range of about 11 to 18 $MPm^{0.5}$ which are consistent with those considered in other studies on hydrogenated and hydride Zr alloys (Cockeram and Kammenzind, 2018) and for commercially pure Zr (Li et al., 2015). With respect to the strong basal texture in the blocky alpha Zircaloy-4 samples, three-point bend testing has been carried out with the predominant c-axis texture aligned in the Z-direction in Samples A and E but aligned in the Y-direction for Samples B, C and D as indicated in Fig. 3-3 (c). In particular, Samples A and B share the same geometry and cyclic loading conditions but have differing predominant c-axis textures.

The cyclic loading testing was interrupted for optical microscope (OM) observation of sample surfaces. The large grain size developed to give blocky alpha ensures that free-surface cracks may develop to a substantial depth whilst remaining within the same

uniform grain crystallography for a given grain. As they reside at or close to the free front surface, the growing cracks observed are likely to be representative of those under conditions of plane stress. The beam sample was returned to the rig after observation for continued testing. The crack length at every interval was measured from the optical microscope image, and the crack growth rate calculated from the slope of two neighbouring data points of crack length (a_i and a_{i+1}) versus cycle number sequentially (N_i and N_{i+1}) as below (E647-93, 1993)

$$\bar{a} = (a_{i+1} + a_i)/2 \qquad (3\text{-}1)$$

$$(\frac{da}{dN})_{\bar{a}} = \frac{a_{i+1}-a_i}{N_{i+1}-N_i} \qquad (3\text{-}2)$$

where a is crack length, N cycle number, and $\bar{a}$ is interval crack length. The stress intensity factor (mode I), ΔK is calculated from standard formulae for edge-notched and cracked beam samples (Anderson, 1996) from

$$\Delta K = \frac{P}{B\sqrt{W}} f\left(\frac{a_e}{W}\right) \qquad (3\text{-}3)$$

$$f\left(\frac{a_e}{W}\right) = \frac{3(\frac{S}{W})\sqrt{\frac{a_e}{W}}}{2(1+2\left(\frac{a_e}{W}\right))(1-\frac{a_e}{W})^{3/2}}\{1.99 - \frac{a_e}{W}\left(1-\frac{a_e}{W}\right)\left[2.15 - 3.93\left(\frac{a_e}{W}\right) + 2.7(\frac{a_e}{W})^2\right]\} \qquad (3\text{-}4)$$

in which P is the load applied on the three-point beam, S the distance between the supporting pins, W and B the height and thickness of the beam respectively, and a_e is the effective crack length,

$$a_e = a_p + a_0 \qquad (3\text{-}5)$$

determined from the sum of the notch depth (height) a_0 and the projected crack length a_p which is obtained from the projection of crack length, a into the Y direction. We note that the stress intensity, as calculated, is not necessarily representative of the short crack driving force; rather, it is used here as an approximation to provide a consistent methodology to characterise crack length, and recognise that growth of thumbnail cracks, crack tortuosity and other factors (including large-scale yielding) may result in substantial deviations from the actual driving force at the crack tip.

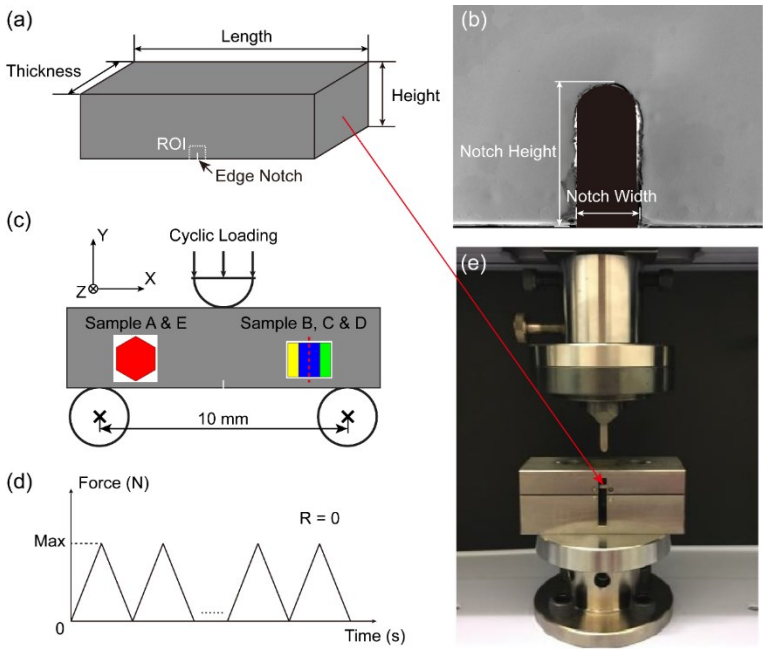


Fig. 3-3. (a) Schematic of edge-notched beam sample; (b) SEM image of edge notch; (c) 2D schematic of sample orientations in three-point bend testing with c-axis aligned in the Z-direction in Samples A and E, while the Y-direction in Samples B, C and D; (d) cyclic loading condition; (e) image of three-point bend testing set-up.

Table 3-1. Summary of sample geometry, loading conditions and edge-notch shape in Samples A, B, C, D and E.

Sample	Geometry (mm)	Maximum Force (N)	Maximum Stress (MPa)	Notch Shape (μm)
A	Height 3.22 Thickness 2.69 Length 12.00	700	376	Notch Height 280 Notch Width 140
B	Height 3.18 Thickness 2.72 Length 12.02	700	382	Notch Height 280 Notch Width 140
C	Height 3.00 Thickness 3.53 Length 12.04	850	401	Notch Height 330 Notch Width 140
D	Height 3.02 Thickness 3.67 Length 12.03	850	380	Notch Height 330 Notch Width 140
E	Height 3.32 Thickness 2.78 Length 12.02	767	375	Notch Height 280 Notch Width 140

3.2.4. SEM and EBSD

Materials characterisation in this thesis was conducted by scanning electron microscope (SEM) and electron backscatter diffraction (EBSD) examination. A Zeiss Sigma-300 SEM with Bruker EBSD detector was applied to scanning over the prepared sample surface. When doing the regular SEM the images were acquired under an accelerating voltage at 5 keV with the working distance at around 10 mm. For EBSD detection, the SEM was operated at a 20 keV accelerating voltage with the scanning surface of a bulk sample tilted 70 degrees from horizontal. EBSD allows crystallographic orientation to be obtained at each individual scanning point by automatically indexing the diffraction

patterns. The resolution of the Kikuchi pattern is 400 × 300 pixels (8 bit) with the exposure time at around 50 ms. Fig. 3-4 shows the schematic of EBSD when the Kikuchi pattern is collected by a detection. The incident electrons which follow Bragg's law take a projection of crystal plane onto a screen forming Kikuchi bands. The width of the bands is a direct function of the d-spacing of the diffracting plane through Bragg's law:

$$\lambda = 2d_{hkl}sin\theta \qquad (3\text{-}6)$$

where λ is the wavelength of the incident wave, d_{hkl} the d-spacing of the reflection plane, and θ the angle prescribing the width of the corresponding band. A Hough-based transformation is utilised to identify the positions of Kikuchi bands. The angles between the detected bands can be calculated and compared with a list of interplanar angles for the analysed structures such that the indexing solution is obtained with the best fit from a look-up table and the orientation matrix can be calculated (Wilkinson and Britton, 2012).

The quality of SEM and EBSD examination is dependent on sample preparation including grinding and polishing. Care must be taken to ensure the sample surface free of any mechanical damage after the final polishing process. Sample preparation steps of Zircaloy-4 for EBSD examination is introduced as follow:

(1) Grind sample surface subsequently by 800#, 1200#, 2000# and 4000# SiC abrasive paper;

(2) Preliminarily polish sample surface by OPS solution;

(3) Electropolish sample surface in a solution of 10 vol. % perchloric acid in methanol at -30 °C for 60 seconds under an applied voltage of 25 V.

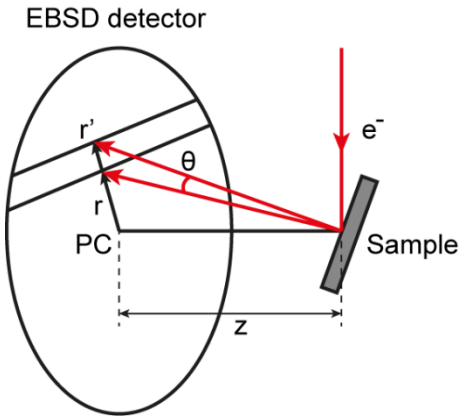


Fig. 3-4. Schematic of EBSD detection showing the band width relation (PC is the pattern centre, z the distance between sample and detector).

3.2.5. Digital image correlation

As a practical and effective method for in-plane strain measurement, two-dimensional DIC is widely utilised in the field of experimental mechanics. This study refers to the in-plane strain measurement by tracing the displacement of speckles on surface during deformation achieved by mechanical loading. The speckles were generated by spraying 1 μm silica particles on polished sample surface as shown in Fig. 3-5. The images of sample surface with speckles were recorded by optical microscope, followed by the post-process on image sequence to calculate strain fields using an in-house Matlab code based on a cross-correlation algorithm (as detailed in Appendix A). The DIC technique in this chapter was carried out with interrupted three-point bend test, which allowed

sample to be taken away from the test for recording speckle images.

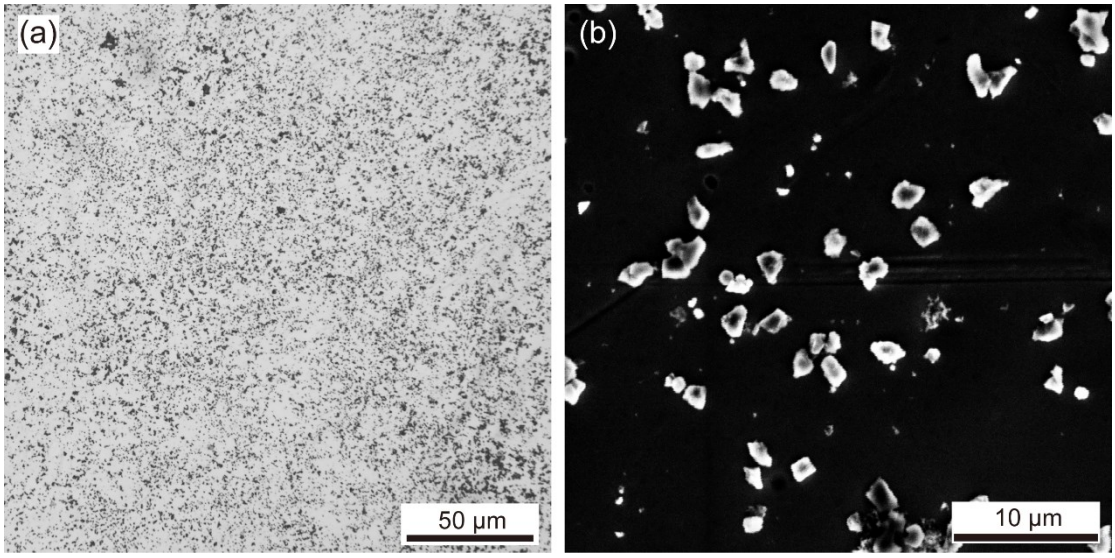


Fig. 3-5. OM image (a) and SEM image (b) showing the distributed 1 μm silica speckles on the sample surface for DIC.

3.3. Short crack paths

The microstructures (grain maps and IPF images) in the ROIs for the five samples are shown in Fig. 3-6. Typical blocky alpha microstructures are observed in all five samples with large grains around the notch root and some small grains randomly distributed at grain boundaries or within large grains. Short cracks are expected to nucleate at the notch root, and then to propagate through the microstructures which are captured by interruption of the cyclic loading tests, quantitative characterisation, followed by repeated sequences of cyclic loading and characterisation.

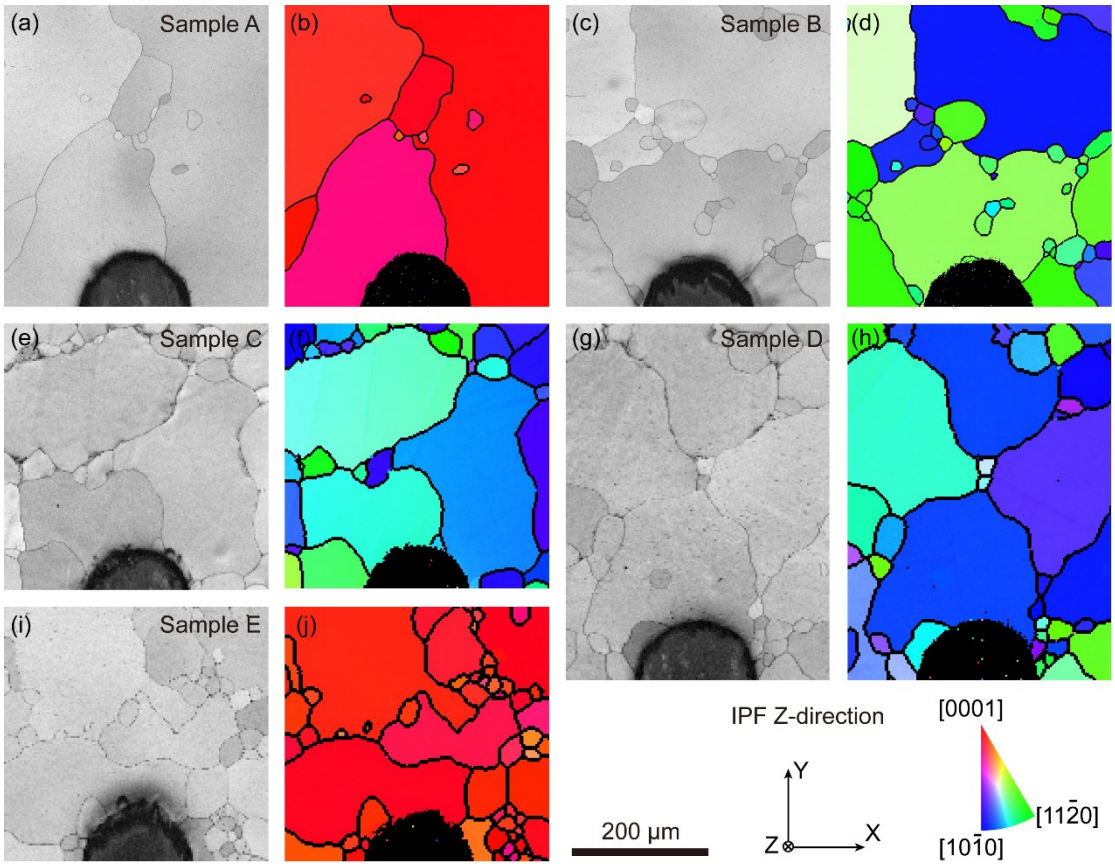


Fig. 3-6. SEM images and IPFZ at ROIs in Sample A (a) (b), Sample B (c) (d), Sample C (e) (f), Sample D (g) (h) and Sample E (i) (j).

After cyclic loading, the crack paths in all five samples are observed by SEM. In Sample A, a zig-zag shaped crack path after 3300 cycles is shown in Fig. 3-7 (a). In particular, the crack nucleates at Grain A1, propagates upwards towards the grain boundary with Grain A2, and continues propagating in the latter grain. Crystallographic orientations are extracted from EBSD results and the IPFX image is shown in Fig. 3-7 (b). The c-axes of Grains A1 and A2 are approximately aligned with the Z-direction, especially that of Grain A2 which is almost perpendicular to the sample surface. The zig-zag crack path in Grain A2 is aligned with the prismatic planes marked in blue and green with sharp deflections, which are marked as D1, D2, D3 and D4 in Fig. 3-7 (a).

The crack in Sample B shown in Fig. 3-7 (c) and (d), however, grows firstly along a more tortuous path, and then tracks along a prismatic plane in Grain B1. It traverses Grains B1, B2 and B3, until it finally enters Grain B4. The crystallographic orientations of these grains are displayed in Fig. 3-7 (c) by the hexagons, and it is clear that the c-axis directions follow a curved path from Grain B1 to Grain B4, which is generally consistent with the crack path, with the exception of the growth in grain B1.

A particularly tortuous short crack path is observed in Sample C as shown in Fig. 3-7 (e) and (f). The crack begins at the grain boundary between Grain C1 and Grain C3, and bifurcates into two directions: one turns left into Grain C2 at the triple junction (D1) as the main crack path; another grows along the grain boundary and develops as a small branch but soon arrests. After a stage of near-horizontal propagation the main crack encounters the second deflection (D2) and turns through about 90^{o} to the Y-direction.

However, it deflects twice again at D3 and D4, and then finally turns back to the Y-direction and hits the grain boundary between Grain C2 and Grain C3. The crack deflects three times (D2, D3 and D4) within Grain C2 and separates the whole grain into two parts, labelled Grain C2' and Grain C2'' as shown in Fig. 3-7 (e). Subsequently, the crack grows across the grain boundary between Grains C2 and C3 without changing direction, passing through Grain C3 until reaching the grain boundary between Grains C3 and C5. The crack deflects again, marked as D5 at this grain boundary, and then changes direction back along the Y-direction at D6. Finally, the last deflection of the crack occurs at D7 at which the crack bifurcates.

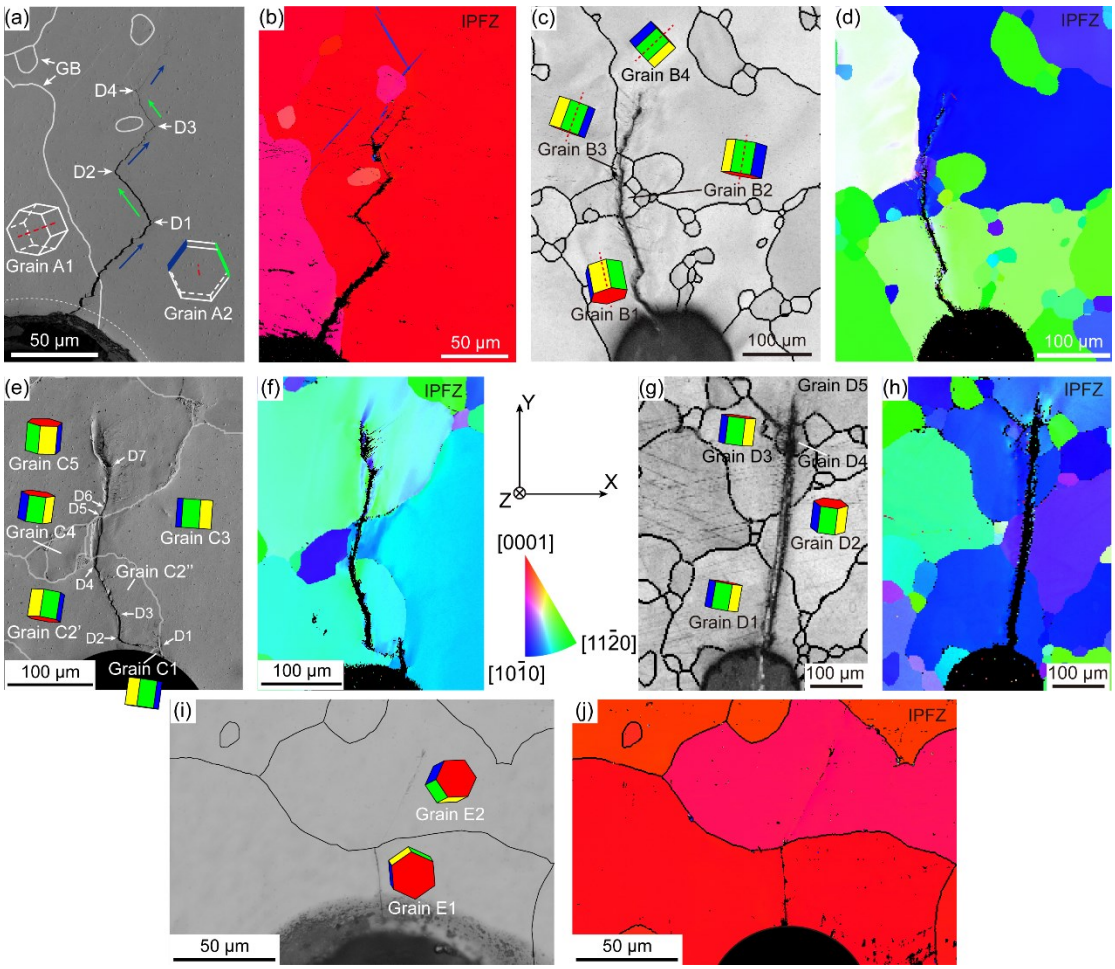


Fig. 3-7. SEM and IPFZ images showing the crack path and the grain orientation for Sample A (a) (b) at cycle 3300, Sample B (c) (d) at cycle 3000, Sample C (e) (f) at cycle 2860, Sample D (g) (h) at cycle 3680, and Sample E (i) (j) at cycle 1700.

The crack path in Sample D after 3680 cycles is shown in Fig. 3-7 (g) and (h) with the SEM and IPFX images. The c-axes of Grain D1, Grain D2 and Grain D3 are highly aligned in the Y-direction. After nucleation at Grain D1 the crack appears to propagate along a relatively straight path following prismatic planes in multiple grains without significant deflection. Fig. 3-7 (i) and (j) show the crack path in Sample E at cycle 1700. The crack nucleates at the middle of the notch surrounded by Grain E1, and then grows

across Grain E1 along a straight path which is aligned with a prismatic plane marked in blue, before reaching the grain boundary with Grain E2. An obvious deflection occurs at the grain boundary between Grain E1 and Grain E2 such that the crack path is remains aligned with a prismatic plane in Grain E2. This deflection drives the crack path from one prismatic plane in Grain E1 to another one in Grain E2.

Samples A and D give two extreme texture cases in which the grain c-axes are near normal and parallel to the crack propagation direction respectively. In Samples B and C, the grain c-axes are also largely aligned with the Y-direction, but there are some deviations from this for some grains (see Fig. 3-7 (c) and (e)). The crack path in Sample B generally follows the trace of the c-axis variation, but with interesting apparent intragranular deviations in Grain B1. For Sample C, similar to Sample B, the crack grows tortuously at the beginning (mainly in Grain C2), and then the crack path mostly follows the prismatic planes in Grains C3 and C5.

Sample E is similar in texture to Sample A (with c-axes predominantly normal to the free surface), but shows a different form of crack path, also resulting from prismatic growth, in Grains E1 and E2 (marked in blue in Fig. 3-7 (i)). In addition, the crack path change in Sample E occurs only at the grain boundary (Grain E1/E2) within the cycles monitored, as opposed to the intragranularly zig-zag path in Grain A2 of Sample A. From the five crack paths above, it is concluded that the short crack propagation in polycrystal Zircaloy-4 is sensitive to the local microstructure with respect to grain crystallographic orientation and grain boundaries. All the cracks appear to be

crystallographic (lying on crystal slip planes) but this is investigated next in more detail.

3.4. Strain distribution

Fig. 3-8 and Fig. 3-9 present the total strain (xx) field at the ROIs just before crack nucleation or at the initiation of the crack growth with crack length less than 50 μm in both Samples A and B. The elastic strains are very small compared with those resulting from the plasticity such that the total strain is very close to the plastic strain in these results. In addition, it is measured from the DIC at the unloaded state in the cycles, and the elastic strain can be ignored. The results in Fig. 3-8 also show the OM images recorded at the interrupted cycles 1 and 1000. A very small crack with length at around 40 μm is observed at cycle 1000 of Sample A as shown in Fig. 3-8 (b), which is shown enlarged in Fig. 3-8 (c). In addition to the two large, diffuse 'butterfly' slip bands emanating from each side of the notch, there is a particular slip band visible with strong strain localisation near the notch tip. This highlighted band develops towards the grain boundary and then deflects to a different direction when it enters the neighbouring grain. The maximum local strain (xx) reaches about 0.025 at cycle 1, and increases to 0.04 at cycle 1000. The crack nucleation site is well identified by the strain distribution map where strong strain localisation is apparent at the crack nucleation site, although the strain localisation is argued to be necessary but not sufficient for driving fatigue crack nucleation. In Sample B, no crack nucleation occurs even after 2000 cycles, and the two regular diffuse strain bands at the notch are visible at cycles 1, 1000 and 2000 as shown in Fig. 3-9 (b), (c) and (d) respectively. However, some indications of strain

localisation are becoming apparent at cycle 2000. The maximum strain at this cycle is about 0.02, which is lower than that even at the first cycle in Sample A. Thus, the earlier crack nucleation in Sample A than Sample B is attributed to the stronger strain localisation with the highlighted slip band in Sample A.

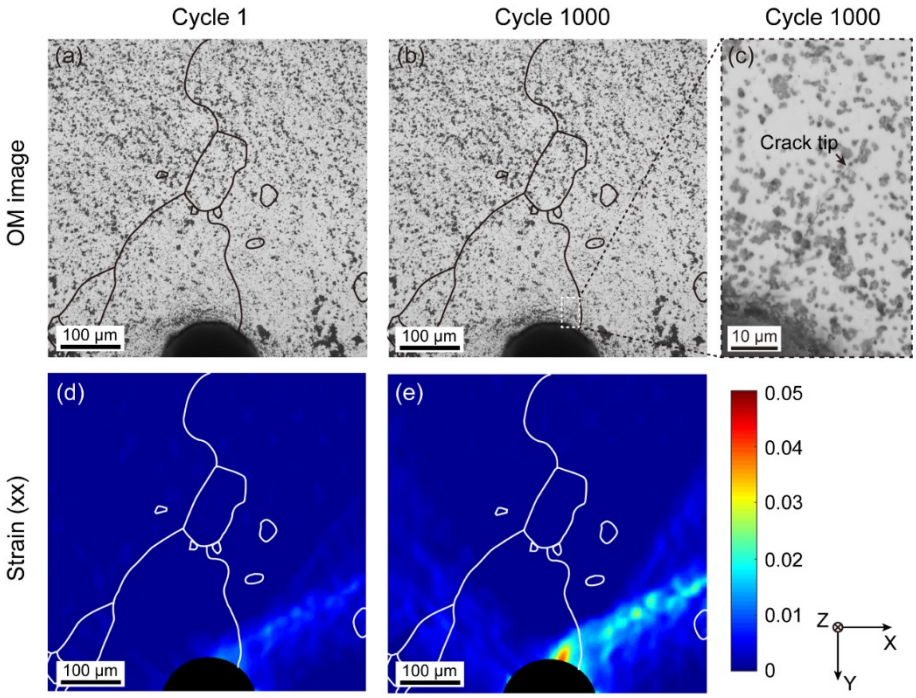


Fig. 3-8. (a) OM image of ROI at Cycle 1; (b) OM image of ROI at Cycle 1000; (c) enlarged OM image of (b); (d) the strain (xx) distribution of ROI at Cycle 1 and (e) at Cycle 1000, all for Sample A.

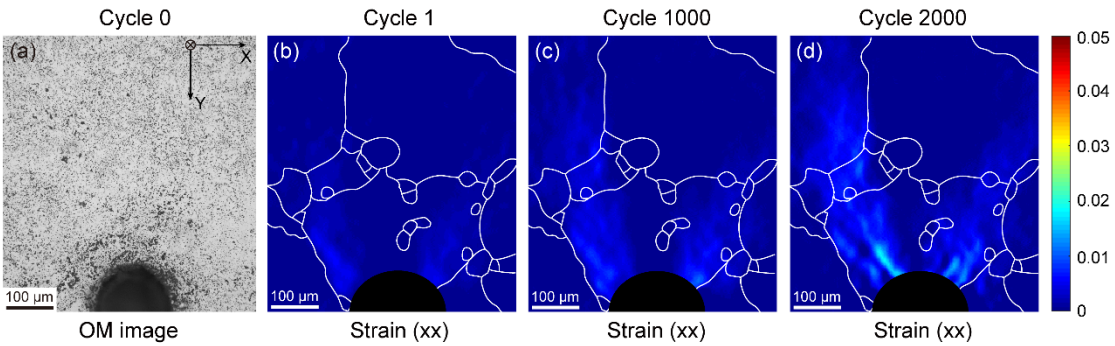


Fig. 3-9. (a) OM image of ROI at cycle 0; strain (xx) distributions of ROIs at (b) cycle 1, (c) cycle 1000 and (d) cycle 2000, all for Sample C.

3.5. Slip activation and fracture tomography

In three-point bend testing the remote loading gives rise to primary stresses along the X-direction, such that the local stresses within the ROI without a crack are likely dominated by the σ_{xx} component. By calculating the apparent Schmid factors (ie based on the remote uniaxial stress state), an indication of the possible primary slip systems before crack nucleation may be obtained. Table 3-2 presents the Euler angles of a subset of grains with 'ZXZ' convention, and the maximum apparent Schmid factor for basal, prismatic and <c+a> pyramidal slip systems in Samples A, C, D and E. For these four samples, basal slip has the lowest Schmid factor in all grains except Grain A1, compared with prismatic and pyramidal slip. Since the critical resolved shear stress (CRSS) of <c+a> first order pyramidal slip (532 ± 58 MPa) and basal slip (204 ± 66 MPa) are a factor of 3.5 times and ~ 30% higher than that of prismatic slip (153 ± 30 MPa) in zirconium (Gong et al., 2015), prismatic slip is expected to be the primary system for all the four samples in the stress state dominated by the σ_{xx} component. However, the local stress state at crack tip is more complicated especially when the crack path is tortuous, and growing along paths which are well removed from being normal to the remote applied stress direction, such that the activation of other slip systems becomes preferable.

The activated slip systems with respect to the crack growth are investigated by SEM observation under high magnification. Fig. 3-10 (a) shows the SEM images of the crack path in Sample A, while Fig. 3-10 (b) shows the enlarged area in the dashed red

rectangle in (a) at the area of the first crack deflection (D1). Clear evidence of the activation of slip in the prismatic slip system directions can be seen in the figure, at locations both close to and removed from the active crack zone. Prism slip bands in two directions, marked in green (Prism Slip 1) and blue (Prism Slip 3) dashed lines, are observed in the high magnification SEM picture in Fig. 3-10 (b). Both prism slip bands are argued to be important in determining the observed main crack path and deflection.

Table 3-2. Grain Euler angles and slip system maximum (apparent) Schmid factor before deformation in Samples A, C, D and E.

Grain	Euler Angle (degree)	Maximum Schmid Factor		
		Basal Slip	Prismatic Slip	Pyramidal Slip
A1	(110, 28, 274)	0.40	0.37	0.45
A2	(180, 6, 205)	0.01	0.46	0.45
C1	(172, 89, 197)	0.13	0.49	0.48
C2	(171, 83, 195)	0.15	0.49	0.49
C3	(356, 90, 18)	0.07	0.49	0.46
D1	(350, 87, 24)	0.16	0.47	0.49
D2	(353, 73, 26)	0.12	0.47	0.48
D3	(353, 86, 23)	0.11	0.47	0.48
E1	(211, 9, 54)	0.07	0.46	0.46
E2	(297, 21, 37)	0.30	0.43	0.49

A highly tortuous branch crack can be seen to grow from D1 towards the right, and finally developing along the direction marked by yellow arrows, which align with Prism Slip 2, shown by the Grain A2 unit hexagon. Hence the main (zig-zag) surface crack in Fig. 3-10 (a) seems to lie within the planes of two activated prism slip systems and

further, grow along the surface in directions which are parallel to the slip systems' Burgers vectors. The branch crack (Fig. 3-10 (b)) is also crystallographic and lies in an active prism slip plane, also growing parallel to the Burgers vector on the free surface.

Fig. 3-11 (a) shows the enlarged SEM images on a part of the crack path in Sample C from the nucleation site to D4. The unit hexagons in the figure present the crystallographic orientation of the grains. Slip bands reflecting slip system activity in Grains C2'' and C3 are marked by white dashed lines in Fig. 3-11 (b). These slip bands are aligned with the lines of intersection between prismatic slip planes (marked in white) and the free surface plane.

Returning to Fig. 3-11 (a), between D1 and D2, the crack grows near-horizontally strongly suggesting that it grows along a basal slip system as shown, and that the crack growth direction is coincident with the basal slip system Burgers vector on the surface. After D2 the main crack initially grows upwards, aligning with a prism plane (see local hexagon in grain C2'), but this time not growing in a direction parallel to the system's Burgers vector. In fact, the surface growth direction while being within a prism plane is normal to the Burgers vector. Fig. 3-11 (c) is then the enlarged SEM image showing the dashed red rectangular area in Fig. 3-11 (a).

In this figure, near to the crack are some slip bands marked in dashed yellow corresponding to pyramidal slip systems in Grain C2'' (see unit hexagon). In addition, to its left are indications of interactions of active prism slip with the free surface. Following the main crack path, it changes to the direction marked with the yellow arrow

after D3, which is aligned with the intersecting line between a pyramidal slip plane, marked in yellow in the Grain C2' unit hexagon, and the free-surface plane. Hence again, crack growth seems to be crystallographic and in this instance after D3, on the surface grows parallel to the pyramidal slip system in a direction which is also parallel with the slip system Burgers vector.

Above right to the crack path, there are many prismatic slip bands and even crack branches along the direction marked by white dashed arrows. These cracks also appear to be crystallographic. As mentioned above these prismatic slip bands are probably produced before the crack growth, and likely help to generate the short branches, dissipating energy from driving the main crack. This may be the reason why the crack chooses to grow along the pyramidal plane in Grain C2 and influences the crack growth rate (see later).

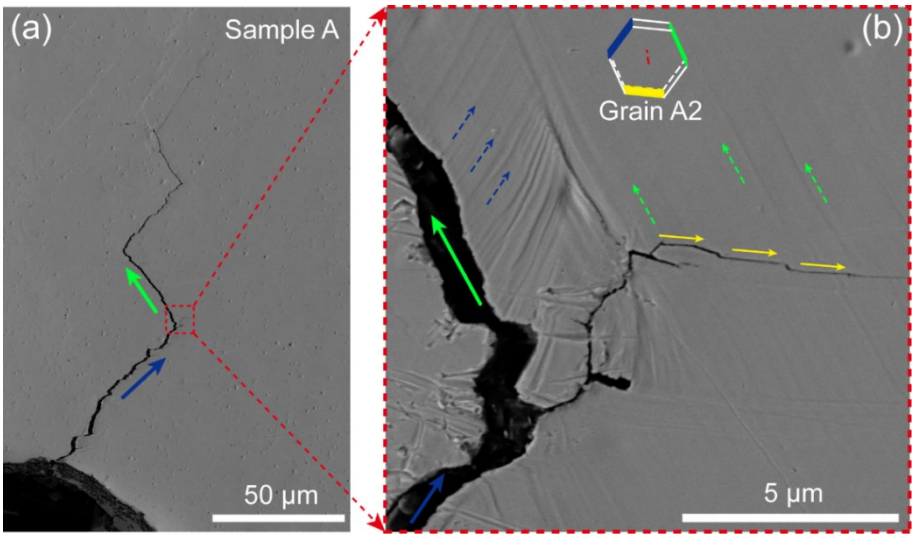


Fig. 3-10. (a) SEM image showing the crack in Sample A; (b) SEM image of the enlarged area in the dashed red rectangle in (a). Broken lines indicate active slip systems, and dotted lines crack paths.

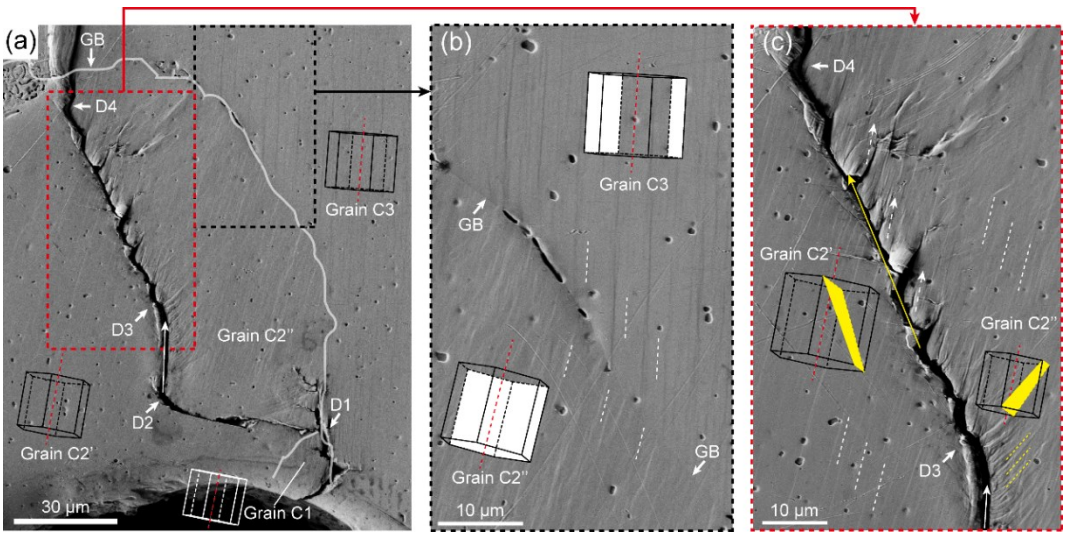


Fig. 3-11. (a) SEM image showing a part of the crack path of Sample C from nucleation site to D4; (b) SEM image of the enlarged area in the dashed black rectangle in (a); (c) SEM image of the enlarged area in the dashed red rectangle in (a).

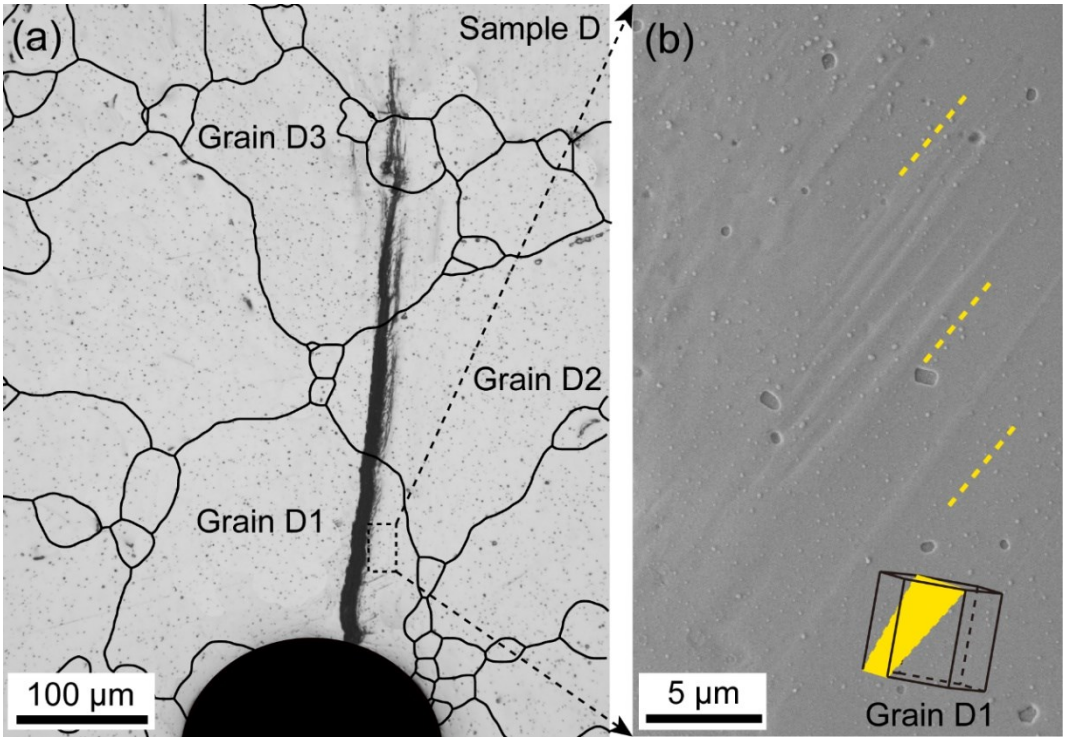


Fig. 3-12. (a) OM image showing the crack path of Sample D; (b) SEM image showing the pyramidal slip trace near the crack path in Grain D1.

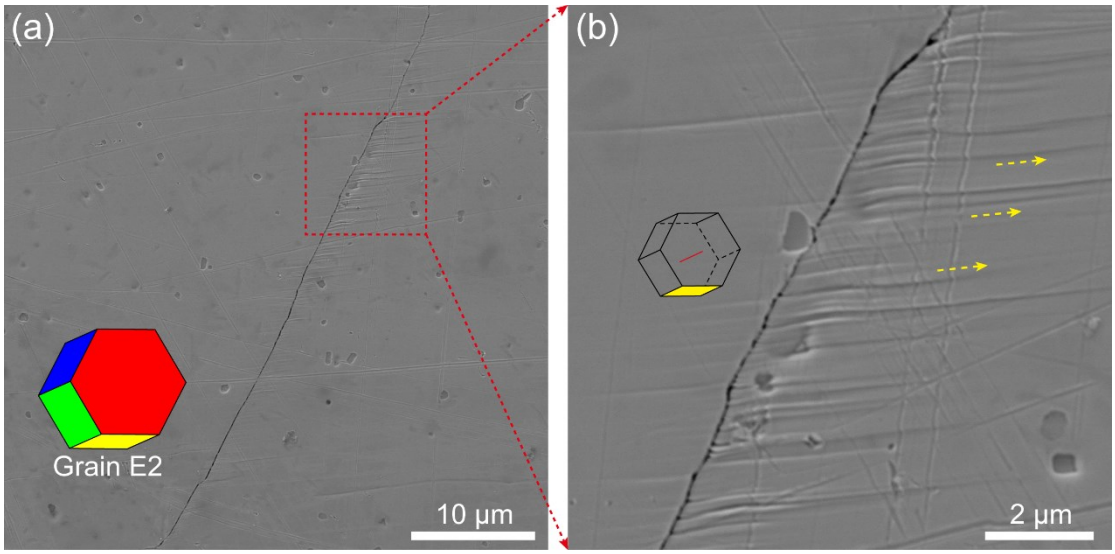


Fig. 3-13. (a) SEM image showing the crack path in Sample E, Grain E2; (b) SEM image of the enlarged area in the dashed red rectangle in (a) showing the prismatic slip trace near the crack path.

Fig. 3-12 (a) is an OM image showing the crack path of Sample D, and Fig. 3-12 (b) shows the enlarged SEM image of the area defined by the dashed black rectangle in (a), near the crack path. Slip bands, shown in dashed yellow lines, are observed in the enlarged SEM image, and are aligned with the lines of intersection between a pyramidal slip plane of Grain D1 (marked in yellow) and the free surface plane. The crack direction, however, is parallel with the crystal prismatic plane and the surface growth direction normal to the prism system Burgers vector, examples of which were also observed earlier in other samples.

Fig. 3-13 (a) shows the SEM image of the crack path in Sample E, Grain E1, and Fig. 3-13 (b) shows the enlarged SEM image of the area defined by the dashed red region in (a). The crack path in Grain E2 is aligned with the prismatic plane (marked in blue) as mentioned above. As shown in Fig. 3-13 (b), slip bands aligned with the lines of

intersection between the prismatic plane (marked in yellow in the hexagon) and the free surface plane are observed near the crack path in Grain E2.

Fracture surfaces (in the YZ plane) were examined with SEM in Samples A and D as shown in Fig. 3-14. Fig. 3-14 (a) and (b) show a fracture surface comprising several contrasting planes in Sample A, which are consistent with the zig-zag crack path in Grain A2, shown in Fig. 3-7. The positions of crack deflection sites are marked by red dashed lines in Fig. 3-14 (b). Together with the analysis of crack path directions in Sample A in Fig. 3-7 and Fig. 3-10, the crack in Grain A2 is demonstrated to be aligned with prismatic planes as shown in Fig. 3-14 (b).

Fig. 3-14 (c) shows an enlarged area of the crack surface in which micro-scale striations parallel with the crystal c-axis can be seen, developing along prism planes, and which are thought to be the lines reflecting the intersection of prismatic slip planes and the crack surface. Sample D with a straight crack path shows a 'corrugated' fracture surface near the sample side surface as shown in Fig. 3-14 (d) and (e). The alternate stripes distributed along the Z-direction on the fracture surface shown in Fig. 3-14 (e) potentially reflect prismatic planes and their influence on the fracture surface, which supports the crack growth in the crystal c-axis direction along prismatic planes in Sample D. Fig. 3-14 (f) is a higher magnification SEM image of part of Fig. 3-14 (e) showing micro-scale striations parallel to <c+a> pyramidal slip traces in Grain D3.

The crack paths in Samples A, C, D and E shown in Fig. 3-10, Fig. 3-11, Fig. 3-12 and Fig. 3-13, together with that in Sample B (see Fig. 3-7) are all found to be

crystallographic in nature. In particular, for Samples A and E, the crack path alternates and aligns with both prism planes and prism slip directions; that is, the surface crack growth follows the slip system Burgers vector. In Sample B, the surface crack path shows strong correlation with prism planes, but with direction normal to the prism system Burgers vector. However, in Sample C, in the most part, the surface crack growth path aligns with either prism (but non-Burgers vector direction) or <c+a> pyramidal slip (Burgers vector direction) systems.

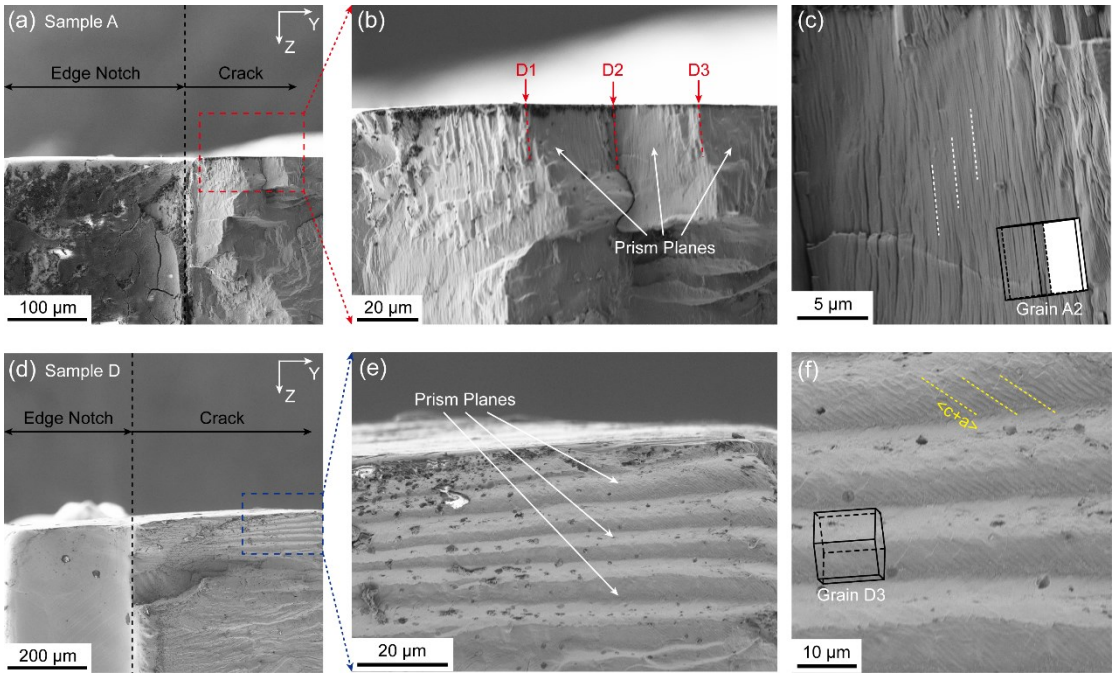


Fig. 3-14. (a) SEM image of fracture surface of Sample A; (b) SEM image of the enlarged area in the dashed red rectangle in (a) showing prism planar regions on the fracture surface; (c) SEM image of an enlarged area in (b) showing striations parallel to crystal c-axes; (d) SEM image of fracture surface of Sample D; (e) SEM image of the enlarged area in the dashed blue rectangle in (d) showing the prism planar regions; (f) SEM image of an enlarged area in (e) showing striations parallel to <c+a> directions.

Finally, in Sample D, the surface crack growth directly aligns with prism systems but grows normal to the Burgers vectors. While no obvious surface evidence of prism slip was observed in Sample D, there was evidence of this slip system activation in Sample C which has similar crystal orientations (ie c-axes normal to loading). Independent modelling work (Wilson et al., 2019, 2018) addressing both Ti and Zr alloy crack growth suggests that at the crack tip, prism slip can be the most favourable in these orientations and leads to crack growth within the prism planes. However, further characterisation studies are required to confirm, or otherwise, that crack tip prism slip activation in Zircaloy-4 occurs and drives the non-Burger prism crack growth directions. With this context, we next address the microstructure-sensitive crack growth rate observations.

3.6. Short crack growth rates

The interrupted three-point bend testing facilitates quantification of the crack length versus cycle number with respect to the microstructural features. The crack length was measured from OM images obtained from every observation made. The graph of crack length versus cycle number and crack growth rate, da/dN versus stress intensity factor (mode I) ΔK for Samples A, B, C, D and E are shown in Fig. 3-15, Fig. 3-16, Fig. 3-17, Fig. 3-18 and Fig. 3-19 respectively. The measured single crystal rates of growth obtained in this study are reassuringly in very good agreement with Stage I polycrystal crack propagation studies carried out on commercially pure Zr in (Li et al., 2015). The deflection sites are marked as Dx in each specific sample.

In Sample A, the crack nucleates before cycle 1000, and the crack length is recorded from cycles 1000 to 3000 with the crack length from 39 μm to 192 μm. The crack growth rate in Sample A shows obvious fluctuations, which correspond to the deflections of the crack path as marked in Fig. 3-7 (a). Compared with Sample A, crack nucleation in Sample B occurs at about cycle 2000. However, the crack grows much faster than that in Sample A, giving a crack length of 450 μm at cycle 3000.

The obvious distinction in crack growth rates can be visualised in the graph of da/dN versus ΔK with the maximum da/dN in Sample A (see in Fig. 3-15 (b)) less than the minimum value in Sample B (see in Fig. 3-16 (b)). In addition, the average crack growth rate of Sample A at 0.08 μm/cycle is much lower than that of Sample B at 0.46 μm/cycle. Recall from above that all of the crack paths are argued to be crystallographic (that is, having growth directions which lie within a given slip plane). The two samples A and B share the same loading conditions and geometries but have very differing textures. In Sample A, the surface crack growth is on prism planes with direction parallel to the slip system Burgers vector. This gives rise to the low average crack growth rate of 0.08 μm/cycle. In Sample B, the crack growth aligns with prism planes but the surface growth direction is normal to the prism Burgers vector, giving a growth rate of six times that for sample A.

Fig. 3-17 (a) shows the crack length versus cycle number in Sample C. The crack length is recorded from cycle 2200 to 2830 with an interval of 30 cycles. The deflection sites are marked corresponding to the crack propagation in Fig. 3-7 (e). The graph of crack

growth rate (da/dN) versus ΔK is presented in Fig. 3-17 (b). The crack growth rate starts relatively high at above 0.4 μm/cycle before cycle 2300, and then decreases to around 0.2 μm/cycle until the crack approaches the grain boundary between Grain C2 and Grain C3. It sees a sudden rise in growth rate when the crack enters Grain C3 but quickly drops down after the peak as the crack reaches another grain boundary between Grains C3 and C5. The average crack growth rate in Sample C is 0.40 μm/cycle. However, it is clear from Fig. 3-11 that the path is very tortuous and that growth occurs along a range of differing slip systems at differing rates, as can be seen in Fig. 3-17 (b).

The crack length versus cycle number in Sample D shown in Fig. 3-18 (a) shows smoother behaviour than for the three samples above, which is attributed to the relatively straight crack path without obvious deflections. The cycle number is recorded from cycle 3000 to 3670 with the crack length at from 101 μm to 452 μm. Fig. 3-18 (b) shows the graph of da/dN versus ΔK for Sample D. The da/dN shows little fluctuation when the crack traverses the grain boundaries, and it is noted that the relevant grains are more closely aligned for this sample than for Samples B and C.

For ΔK between 14 and 18 $MPm^{-0.5}$, da/dN is below 1.0 μm/cycle, while it increases to 1.7 μm/cycle at the final stage (after cycle 3600) when the crack enters Grain D4 and Grain D5. This increase of crack growth rate may suggest the crack propagation is approaching stage II, and becoming less microstructurally sensitive. The average crack growth rate in Sample D is 0.52 μm/cycle. We note from the previous section that the surface growth path was found to be completely crystallographic and prismatic, with

growth normal to the prism Burgers vector.

Fig. 3-19 (a) shows the crack length versus cycle number in Sample E. The crack length is recorded from cycle 800 to cycle 1700 with an interval of 50 cycles. The crack growth rate as shown in Fig. 3-19 (b) starts at around 0.13 μm/cycle in Grain E1, and then drops to less than 0.04 μm/cycle at the grain boundary between Grain E1 and Grain E2. This retardation is attributed to the crack deflection at the grain boundary as shown in Fig. 3-7 (i) and (j), which results in the crack path transferring from the prismatic plane in Grain E1 to another prismatic plane in Grain E2. In Grain E2, the crack growth rate recovers to around 0.08 μm/cycle. The average crack growth rate in Sample E is 0.08 μm/cycle. Similar to Sample A, the surface crack growth in Sample E is parallel to the prism Burgers vector.

The growth rates obtained throughout the history of the crack growth for each sample allow us to investigate in more detail the crack growth rates directly associated with the grain crystallography within which the crack tip resides. Recall from Table 3-1 that the peak bending stresses (at the base of the samples) are not identical (because of small variations in geometry etc) but are close enough to warrant a study of the crystallographic growth rates. In addition, we should be aware, as given above, that the tortuous crack path lengths are true lengths, but that ΔK values in Eqn. (3-3) are determined taking the crack lengths projected into the Y-direction which underestimates the true length for the zig-zag path of the crack in Sample A, for example.

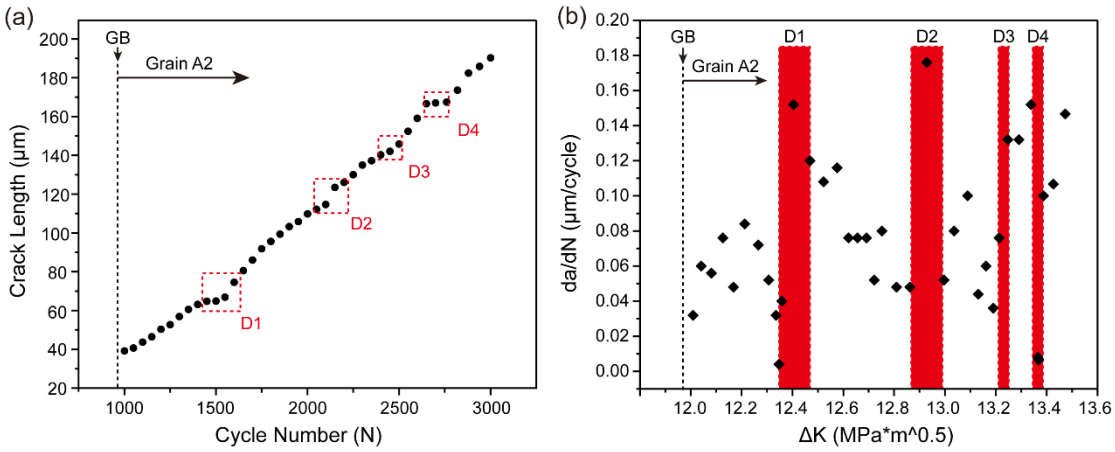


Fig. 3-15. (a) Crack length versus cycle number, and (b) da/dN versus ΔK in Sample A.

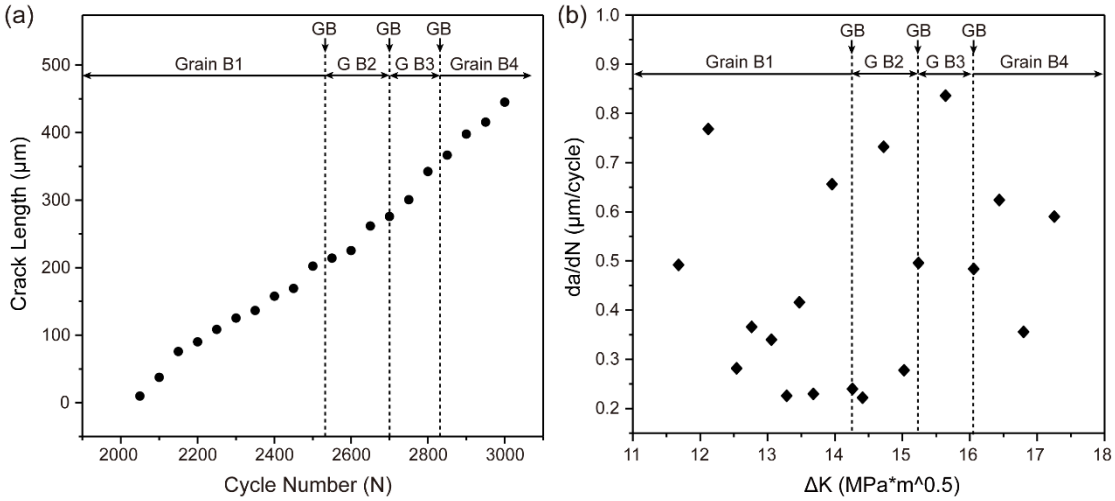


Fig. 3-16. (a) Crack length versus cycle number, and (b) da/dN versus ΔK in Sample B.

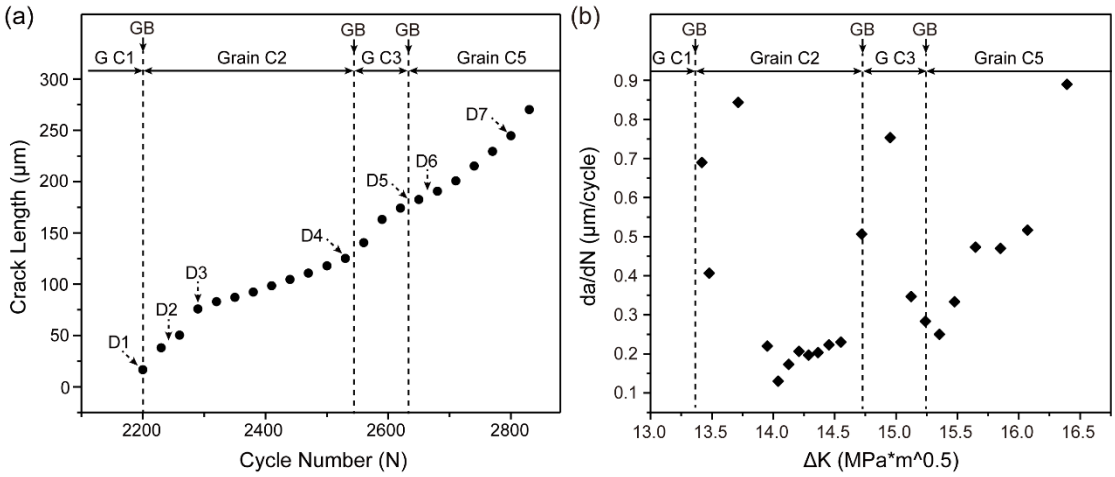


Fig. 3-17. (a) Crack length versus cycle number, and (b) da/dN versus ΔK in Sample C.

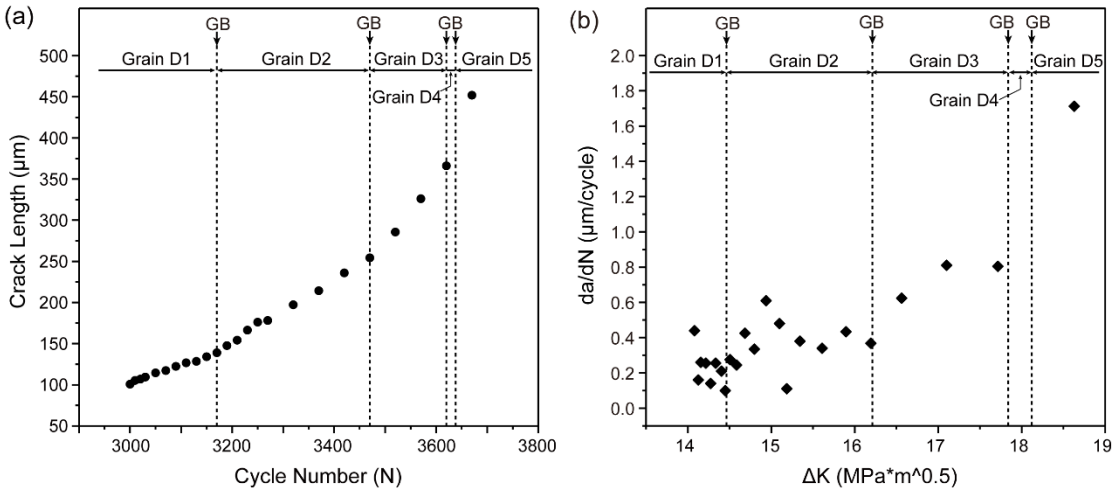


Fig. 3-18. (a) Crack length versus cycle number, and (b) da/dN versus ΔK in Sample D.

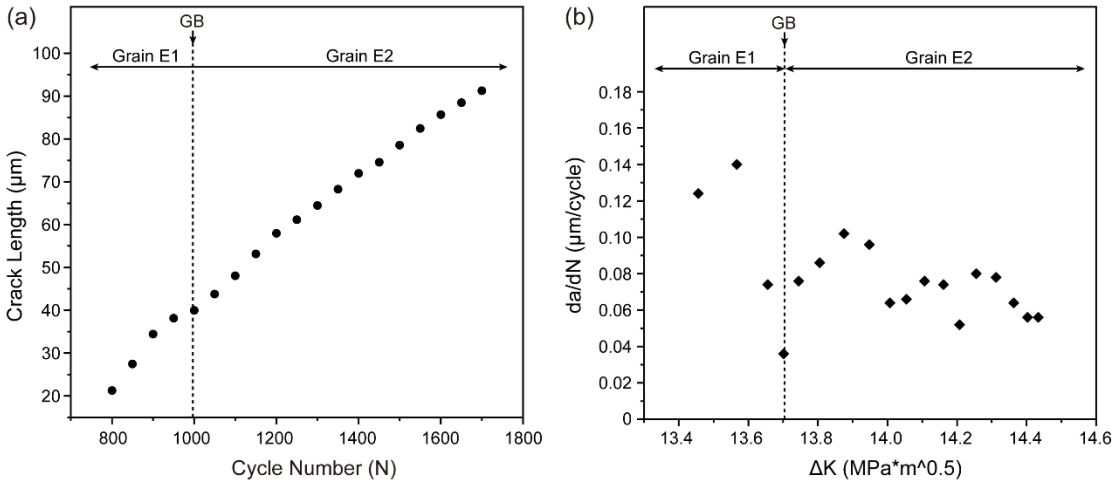


Fig. 3-19. (a) Crack length versus cycle number, and (b) da/dN versus ΔK in Sample E.

Table 3-3 summarises the crystallographic cracks within the differing grains in samples A, B, C, D and E showing the stage of crack growth within the microstructure (given by the crack deflection locations or the grain boundaries shown in Fig. 3-7), the nature of the crack growth (whether prism, basal or pyramidal as well as Burgers vector or non-Burgers vector direction with respect to surface crack growth direction), and the measured growth rate. A crack growth stage is taken to be one for which the

crystallography remains unchanged and hence the average crack growth rate for given crystallography can be estimated. For Samples A, B, D and E, the rate differences between stages chosen were found to be modest since the nature of the crack growth did not change significantly for a given sample as shown in the Table 3-3.

Table 3-3. Surface crystallographic crack growth rates (***b*** indicates corresponding Burgers vector direction, and non-***b*** indicates normal to Burgers vector respectively for surface crack growth).

Sample	**Crack Growth Stage**	**Crystallographic Crack Type**	**Measured Growth Rate (µm/cycle)**	**Normalised Growth Rate (wrt lowest A)**
A	– D1	Prism ***b***	0.052	1.0
	D1 – D2	=	0.087	1.7
	D2 – D3	=	0.064	1.2
	D3 – D4	=	0.100	1.9
B	Grain B2	Prism non-***b***	0.41	7.9
	Grain B3	=	0.67	12.9
	Grain B4	=	0.51	9.8
C	D1 – D2	Basal ***b***	0.69	13.3
	D2 – D3	Prism non-***b***	0.63	12.1
	D3 – D4	Pyramidal ***b***	0.20	3.8
	D4 – D5	Prism non-***b***	0.54	10.4
D	Grain D1	Prism non-***b***	0.22	4.2
	Grain D2	=	0.38	7.3
	Grain D3	=	0.61	11.7
E	Grain E1	Prism ***b***	0.094	1.8
	Grain E2	=	0.073	1.4

The very interesting result is that the lowest fatigue growth rates occur for prismatic surface cracks growing in the Burgers vector direction. For the other Burgers vector direction surface cracks, next in rank is Burgers pyramidal cracks, followed by apparently high growth rates of basal Burgers cracks. All other measured cases are for prism surface crack growth normal to the Burgers vectors which grow at a rate nearly an order of magnitude higher than that for prism Burgers cracks. It is also interesting to note that the crack growth rates for prism cracks normal to Burgers vector are reasonably consistent both within an individual sample (C) and across samples (B, C and D), for a given (approximately constant) applied peak stress. Importantly, in assessing crack growth rates in the context of fatigue lives, it becomes apparent that the path taken by a crack, and hence the crystallographies that it encounters during its growth, have a profound effect on fatigue life, and must in addition play a significant role in the experimental scatter often obtained for short crack growth.

Recent modelling studies in fatigue utilising discrete dislocation and crystal plasticity modelling have focused on the local stored energy established by dislocations which interact, entangle and form structures. At the discrete dislocation length scale, this is termed the dislocation configurational energy density when calculated with respect to an area determined by the dislocation density (Zheng et al., 2019). An approximately equivalent calculation of this quantity, but at the crystal plasticity length scale, has been established and applied to address crack growth in a zirconium alloy in (Wilson et al., 2019). Here it was demonstrated that the stored energy density was sensitive to the microstructure (including for intragranular cracks).

An investigation of fatigue crack growth in single- and bicrystals of zirconium has also been carried out with these models to address fatigue crack path and rate of growth at a crystallographic scale. Crack growth was argued to occur on those crystal planes which contained the highest slip accumulation in directions which gave rise to the highest local stored energy density. Crack growth was allowed to occur only when a critical value of stored energy density was achieved. The studies revealed that intragranular single crystal fatigue crack growth along prism slip planes could give rise to oscillating 'zig-zag' paths as the cracks grow in to the previously strained but uncracked regions. The key crystallographic orientation giving rise to this is that in a grain in Sample A considered above which shows intragranular crack path change in good agreement with the model results in (Wilson and Dunne, 2019). Other crystal orientations leading to prism slip lead to intragranular crack growth but without oscillations.

The modelling also addressed the case of crack growth in a grain orientated with its c-axis parallel to crack growth. In this instance, the propagation path with the highest slip accumulation and direction corresponding to the highest stored energy density at the crack tip was found to be within a prism plane but normal to the Burgers vector direction (ie parallel to the crystal c-axis). The experimental Sample D (and others) in the present work appear to show this type of crack path behaviour.

The present work has enabled crack growth rates within single crystals and their paths to be measured. The experimental measurements here suggest the fatigue cracks

growing along prism Burgers vector directions (e.g. Sample A) are several times slower than those growing along non-Burgers vector directions (e.g. Sample D) within a prism plane (see Table 3). This result is not only supported by experimental fracture toughness studies on other HCP structure materials (Bowen, 1978; Umakoshi et al., 1996) but also predicted nicely by the stored energy density model in (Zheng et al., 2019) and results from the differing slip fields established ahead of a crack growing along differing crystallographic planes. This in turn alters the stored energy density accumulation and hence the rate of crack propagation along the differing crystal planes. In addition, the measured rates of crack growth in the present work correspond well with independent measurements in the literature, albeit for commercially pure polycrystal zirconium, for Stage I (short) crack growth (Li et al., 2015).

Further modelling work (Wilson et al., 2019) utilising the stored energy also addressed crack propagation observations in HCP titanium and zirconium polycrystals, BCC ferritic steel polycrystals, and FCC nickel oligocrystals. Explicit model representations of the experimental microstructures demonstrated that the observed complex microstructurally-sensitive crack paths could be captured by the model. The present study provides quantitative measurements of crack growth in zircaloy-4 single crystals demonstrating strong anisotropy resulting from the HCP crystallography which is quite different to that observed in cubic (BCC and FCC) systems. Crack propagation is observed along prismatic planes both parallel and normal to the <a> Burgers vector, as well as along basal and pyramidal <c+a> planes. In particular, rates of crack growth are anisotropic with differing rates observed in prismatic planes for crack growth in the <a>

Burgers vector and in-plane normal <c> directions respectively.

3.7. Twinning

Plastic deformation in materials with a HCP structure is accommodated by both slip and twinning. Twinning is commonly observed in cyclic loading in HCP alloys, and fatigue cracks have been found to preferentially nucleate at twins in magnesium (Uematsu et al., 2016) and titanium (Ng et al., 2004). However, direct observation of twinning which is associated with crack propagation is rarely reported. Mine et al (Mine et al., 2011) reported on the activation of $\{01\bar{1}2\}$ micro-twins parallel to basal planes during crack growth in single crystal titanium. However, no crystallographic evidence of twinning was given. Wu et al (Wu et al., 2010) used in-situ neutron diffraction to investigate the twinning and de-twinning behaviour during fatigue crack propagation in a magnesium alloy. Although their results showed twinning-detwinning behaviour by detecting a normalized intensity lattice strain fluctuation around the fatigue crack tip, the twinning map and orientation relationship with the matrix were not known.

Twinning is observed in Sample A at cycle 3300 as shown in Fig. 3-20. Fig. 3-20 (a) and (b) are enlarged SEM and IPFX images of Fig. 3-10 (a) and (b) showing the twins near the crack tip in Grain A2. As the c-axis of Grain A2 is aligned with the Z-direction these twinning plates shows interesting growth directions which are very close to the crack propagation directions. Two twin variations with different crystallographic orientations are detected as Twin 1 and Twin 2. Twin 1 and Twin 2 are identified as $\{10\bar{1}2\}$ $<\bar{1}011>$ tensile type twinning, and they are two twin variations with different

crystallographic orientations. They share the same misorientation angle between twinning and the parent of around 86 degrees, but have different twinning planes and directions as shown in Fig. 3-20 (c) and (d) respectively. The crystallographic orientations of twins and parent with the Euler angles are presented by hexagons, and the twinning planes and directions are marked as green planes and arrows, respectively.

Twinning is also observed in Sample C. Fig. 3-21 (a) shows the crack tip area where the crack bifurcates into two branches after D7 in Sample C. Fig. 3-21 (b) is the corresponding IPFX image of Fig. 3-21 (a) presenting large twinning plates which are located at two sides of the crack path around the crack tip. As these twinning plates are sharp when most removed from the crack, they probably nucleate close to the crack path and grow into the parent grain. Fig. 3-21 (c) and (d) are two enlarged pictures from Fig. 3-21 (b) marked by dashed black and yellow rectangles. The profiles in Fig. 3-21 (e) and (f) display the relationship between the reference angle along point A to B and C to D in Fig. 3-21 (c) and Fig. 3-21 (d) including Twin 1 and Twin 2 respectively. In particular, the crystallographic orientations of the twins and parent with the Euler angles are presented in Fig. 3-21 (e) and (f) with the twinning planes and directions marked in green. The misorientation angle of the twins and parent is around 86 degrees, which determines the twinning in Sample C as the same type with that found in Sample A.

The twinning behaviour in blocky alpha microstructures is addressed with the crystallographic orientation relationship, twinning plane and direction, and local grain slip system. The twinning in the crack area is likely to be dependent on the local stress

state, and has strong dependence on local microstructures. With the crack growth, the stress at the crack tip increases. When the local stress reaches the twinning CRSS, twins nucleate and grow, giving a higher density of twins for longer crack lengths. In addition, a twinning assisted mechanism is argued to explain twin production along the crack tip in Sample C. When the crack length is small, the Mises stress at the crack tip is relatively low. The slip can accommodate the deformation at the plastic zone. However, with significant crack growth resulting in the increase of stress ahead of the crack tip, the slip is no longer able to accommodate the deformation so as to drive twinning. Although the twins in Sample A are not seen to assist crack growth directly, they are believed to be strongly interacting with the crack propagation. The details of the interactions require further investigation.

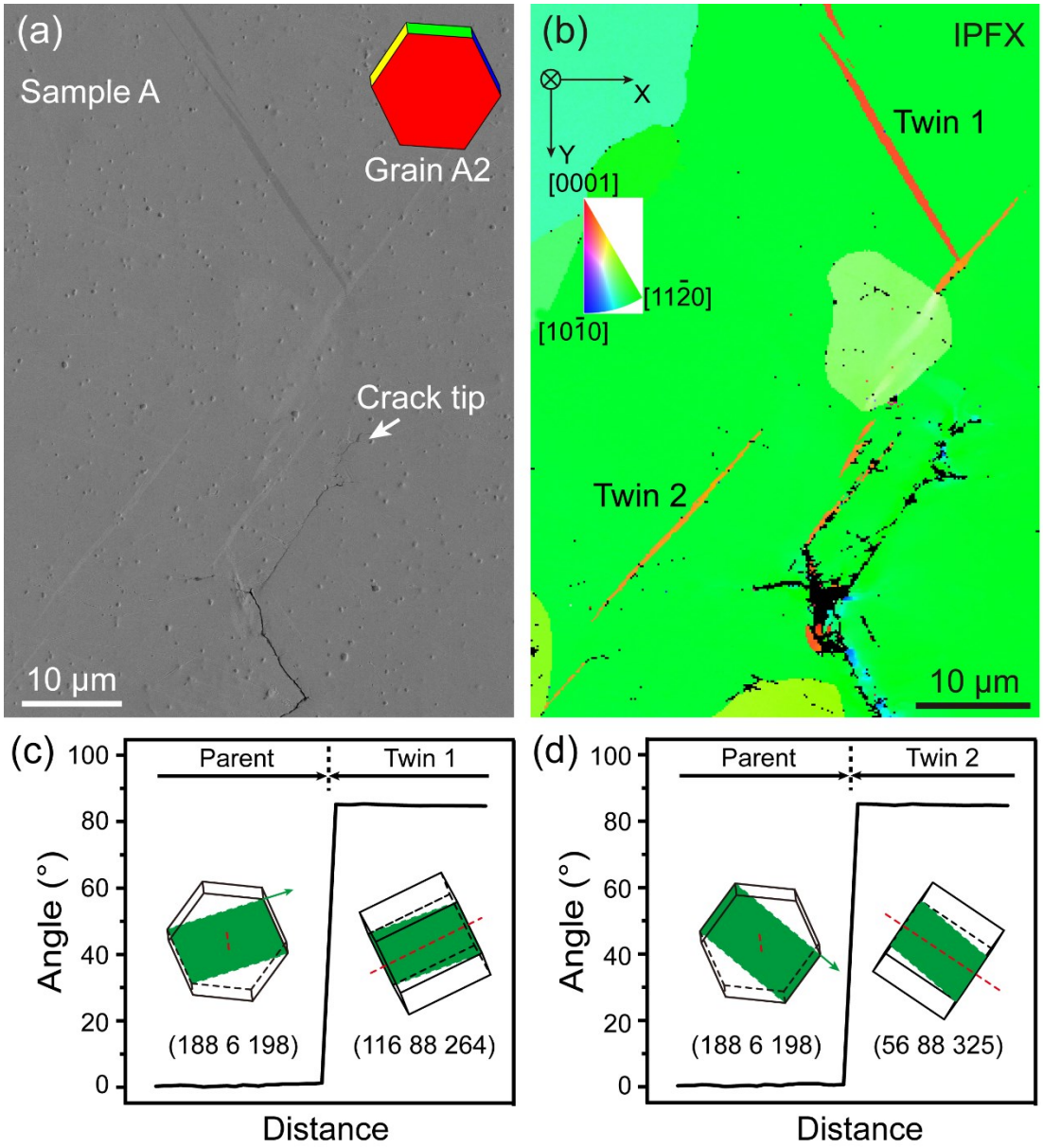


Fig. 3-20. (a) SEM image of crack tip area in Sample A; (b) IPFX image of the same area as (a); (c) the crystallographic orientation of the Twin 1 and parent; (d) the crystallographic orientation of the Twin 2 and parent.

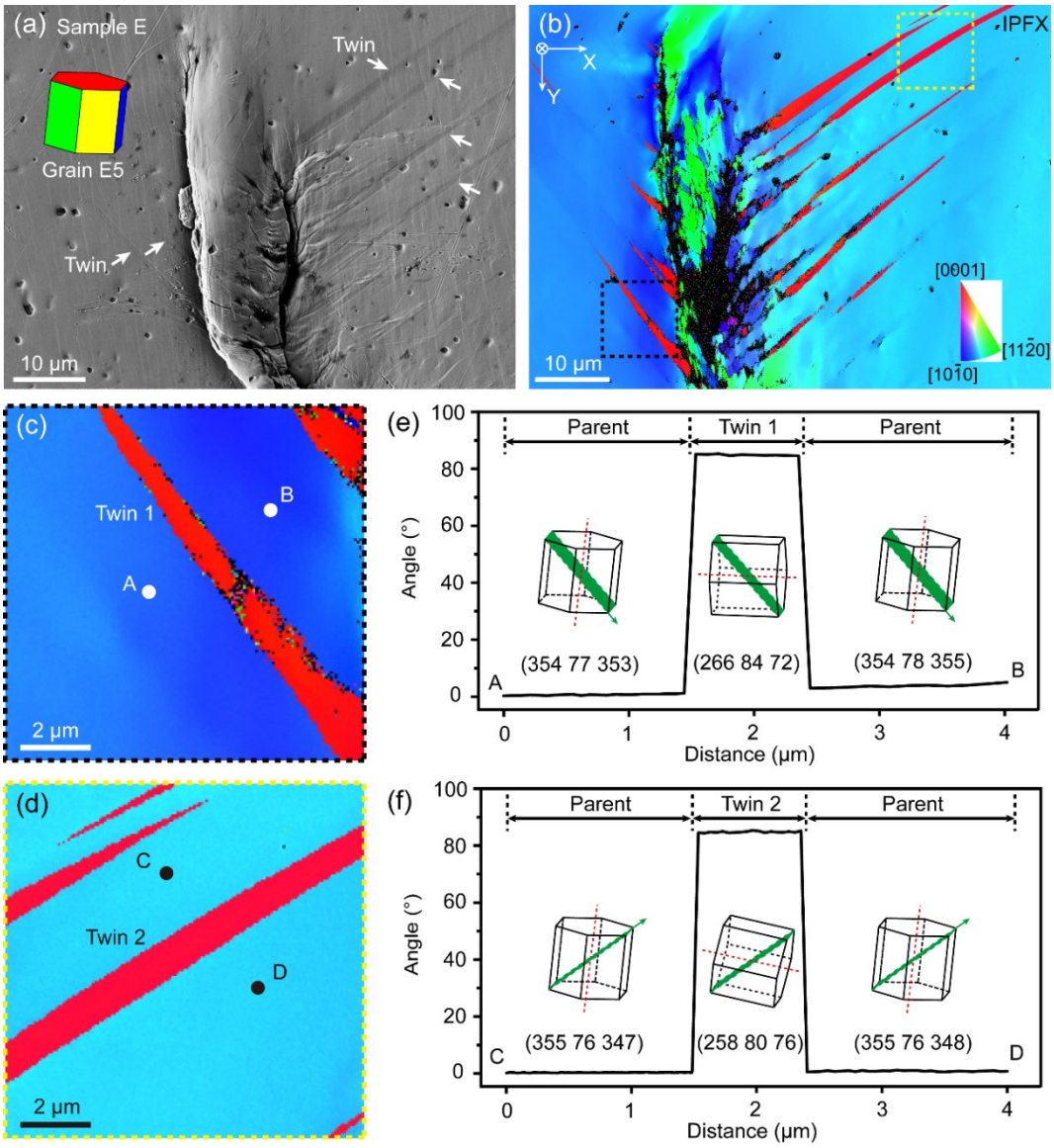


Fig. 3-21. (a) SEM image of crack tip area in Sample C; (b) IPFX image of the same area as (a); (c) enlarged image of the black dashed rectangular area in (b); (d) enlarged image of the yellow dashed rectangular area in (b); (e) crystallographic orientations of the twin and parent in (c); (f) crystallographic orientations of the twin and parent in (d).

3.8. Conclusions

Microstructural-sensitive short fatigue crack growth in alpha Zircaloy-4 has been investigated in experiments with SEM and EBSD characterisation and three-point bend

testing by exploiting blocky alpha grain size. The key conclusions can be drawn as follows:

(1) Short crack growth in HCP Zr has been found to be microstructurally sensitive and to be entirely crystallographic in nature. Crack propagation along prismatic, pyramidal and potentially basal planes has been observed where the 2D surface growth direction is parallel to the corresponding system Burgers vector. In addition, surface propagation within prism planes but normal to the direction of the system Burgers vector has also been observed.

(2) Crystallographic-specific crack growth rates show consistency both within a single polycrystal sample and across samples for given load, providing evidence of repeatability. Non-Burgers vector prism surface crack growth rate (~0.4 μm/cycle) was found to be remarkably higher than that for Burgers vector prism surface crack growth (~0.1 μm/cycle).

(3) Short crack growth is coupled with slip activation which has a strong effect on crack path and crack growth rate. Prism slip is associated with prism Burgers vector surface crack growth, while prism and <c+a> pyramidal slip activation are both observed in Non-Burgers vector prism surface crack growth.

(4) Tortuous crack paths are observed, even though always crystallographic. Zig-zag paths can be generated along alternating prism slip directions when cracks grow normal to the HCP crystal c-axis. Straight crack paths are observed within prism planes in

single- and polycrystals when the growth direction is parallel to the predominant c-axis direction.

(5) Several $\{10\bar{1}2\}$ $<\bar{1}011>$ twins are observed in the region of the crack tip in Samples A and C, which likely arises from slip inhibition and hence stress localisation. Twinning near the crack tip is speculated to assist the crack growth when the slip is not sufficient to accommodate the plastic deformation at the crack tip zone.

4. Strain rate sensitivity of Zircaloy-4 at room temperature

4.1. Introduction

Strain rate sensitivity, which describes the effect of strain rate on flow stress has been widely investigated in recent decades. For most polycrystalline metals, higher strain rates account for larger flow stress. The strain rate sensitive index, m is defined as

$$m = \frac{\partial \ln \sigma}{\partial \ln \dot{\varepsilon}} \qquad (4\text{-}1)$$

where σ is the flow stress of the material at a given strain and temperature and $\dot{\varepsilon}$ strain rate. From this relationship the flow stress is highly dependent on the strain rate when the value of m is high, and a low value m indicates less dependence on strain rate.

Extensive experimental work by (Campbell and Ferguson, 1970; Khan and Liu, 2012) has shown that the stress increases slowly with the logarithm of strain rate at low strain rates (10^{-5} to 10^{2} s^{-1}) while the strain rate sensitivity increases greatly at high strain rate (above 10^{3} s^{-1}) for rate sensitive metals such as aluminium, copper and steel. It is argued that dislocation motion is controlled by thermal activation mechanisms at low strain rates but by drag mechanism at high strain rates (Granoto, 1973; Regazzoni et al., 1987). Recent studies in titanium from Zheng et al (Zheng et al., 2016a) found that the dislocation nucleation and mobility mechanism could explain rate-sensitive behaviour for strain rates in the range 10^{2} to 10^{5} s^{-1} while thermally-activated dislocation escape was considered to be the predominant mechanism of rate dependent behaviour for low

strain rates (< 10^2 s^{-1}). Thus, the thermal activation mechanism is argued to be relevant to address the strain rate sensitivity at low strain rates in zirconium alloys.

The strain rate sensitivity of HCP metals shows anisotropic responses to the variation of strain rate due to multiple deformation mechanisms such as different slip system activations in crystallographic structure or twinning. Wang et al (Wang et al., 2018) studied the effect of strain rate sensitivity on mechanical behaviour of magnesium alloys involving multiple and coupled deformation mechanisms indicating that in these alloys, the different deformation mechanisms have their own strain rate sensitivities. Differing rate sensitivities with respect to the grain orientations in magnesium alloys (Tang et al., 2015) and zirconium alloys (Skippon et al., 2019) have also been obtained via X-ray diffraction detection. Titanium alloys (alpha phase) also show anisotropic rate-dependent response with the intrinsic strain rate sensitivity of basal slip different to that for prismatic slip (Jun et al., 2016b; Zhang et al., 2016).

The studies on strain rate sensitivity in zirconium are mainly focused on temperature and environment dependence. It is well known that the strain rate sensitivity of zirconium does not increase monotonically with temperature. Lee (Lee, 1970) studied the strain rate dependent plastic flow over a range of temperatures from room temperature to 500 °C in several zirconium alloys showing that when the strain rate was lower than 10^{-3} s^{-1} the strain rate sensitivity of Zircaloy-2 at 400 °C was observed to be lower than that at 200 °C. The depression of strain rate sensitivity over a broad temperature range is argued to be attributed to dynamic strain aging (Lee et al., 2001;

Tiwari et al., 1972). Hayes and Kassner (Hayes and Kassner, 2006) studied the creep behaviour of zirconium alloys over a broad range of stresses and temperatures, and they found irradiation appeared to increase the creep strength of zirconium. Piercy (Piercy, 1968) found that the in-reactor creep rate of a cold-worked zirconium alloy is due to dislocation climb caused by the super-saturation of vacancies and interstitials that is introduced by irradiation.

The plastic deformation of zirconium at room temperature was thought not to be sensitive to strain rate (Lee, 1972). Storer et al (Storer et al., 2016) carried out an indentation test to study the viscoplastic 'creep' in zirconium at room temperature. They found Zircaloy-4 was not rate dependent with no significant influence from loading rates on the value of the stress exponent during indentation creep at room temperature. However, the strain rate sensitivities in these works were obtained via macroscopic experimental test without considering the effect of local microstructures. Rate dependence can be obvious in a local area in which plastic strain localisation is dominant.

In this study, a three-point bend creep test coupling with in-situ DIC strain measurement was developed to study the rate dependent behaviour of Zircaloy-4 at room temperature. Blocky alpha microstructure Zircaloy-4 containing a notch has been used to investigate the microstructural sensitivity of strain rate sensitivity coupling with crystal plasticity finite element (CPFE) modelling carried out independently by (Liu et al., 2020). Quantities including local strain, local stress and strain rate were addressed from the

experiment. The experimental measurements are used to facilitate the calibration of the crystal plasticity slip rule and to enable full-field microstructure CPFE models to be developed (Liu et al., 2020). Detailed comparisons of experimental and simulation results (taken from (Liu et al., 2020)) are then presented in order to extract understanding of strain rate sensitivity in the Zircaloy-4. In addition, it is important to understand the strength of the strain rate sensitivity in this alloy since it has a potentially profound effect on material response to stress hold periods in fatigue loading cycles. This is a key issue for subsequent work since it determines whether a stress hold can be incorporated within the fatigue loading cycles to facilitate DIC strain measurement at peak load; a low strain rate sensitivity would imply very little change to measured strains during the stress hold, but moderate or high strain rate sensitivity would lead to substantive strain evolution by creep at peak stress holds, thus introducing major implications for the nature of the loading cycles and the fatigue response investigated. This is addressed briefly later in the relevant chapter.

4.2. Methods

4.2.1. Crystal plasticity and thermal activation slip rule

Rate-dependent CPFE modelling is applied to simulate the creep behaviour of Zircaloy-4 by implementing the crystal plasticity slip rules into the user material subroutine UMAT for ABAQUS standard/explicit analysis. A brief summary of the modelling method is therefore presented, and while the CPFE modelling was carried out by other researcher (Yang Liu, and detailed in (Liu et al., 2020)). These results rely on the

experimental and mechanistic data obtained as part of the work presented in this thesis. The total deformation gradient $\boldsymbol{F}$ is split into elastic deformation gradient $\boldsymbol{F}^e$ and plastic deformation gradient $\boldsymbol{F}^p$,

$$\boldsymbol{F} = \boldsymbol{F}^e \boldsymbol{F}^p \qquad (4\text{-}2)$$

The plastic velocity gradient is given by $\boldsymbol{L}^p$

$$\boldsymbol{L}^p = \dot{\boldsymbol{F}}^p (\boldsymbol{F}^p)^{-1} = \sum_i \dot{\gamma}^i \, \boldsymbol{s}^i \otimes \boldsymbol{n}^i \qquad (4\text{-}3)$$

in which $\boldsymbol{s}^i$ is the line vectors along slip direction and $\boldsymbol{n}^i$ the normal vector of slip plane in slip system *i*. '⊗' refers to the Kronecker product. The slip rule $\dot{\gamma}^i$ is now introduced as follows.

Plastic deformation of crystalline materials has been established as a thermally activated process, and the thermal activation mechanisms controlling dislocation mobility with respect to applied stress and temperature are of key importance in slip behaviour (Evans and Rawlings, 1969). The dislocation motion can be hindered by different natures of barriers such as forest dislocations, small second phases and intrinsic lattice resistance. Thermal activation processes can help the dislocations overcome the energy barriers of these obstacles.

The dislocation slip rate process for the i^{th} slip system can be based on the thermal activation of pinned dislocations overcoming the barrier and escaping from the obstacles. The shear strain rate $\dot{\gamma}$ is proportional to the mobile dislocation density ρ_m,

the average dislocation velocity v_g and the Burgers vector b (Cottrell and Dexter, 1953):

$$\dot{\gamma} = \rho_m v_g b \qquad (4\text{-}4)$$

The average velocity can be expressed as (Granato et al., 1964)

$$v_g = \frac{d\upsilon b}{2l} \exp\left(-\frac{\Delta G}{kT}\right) \qquad (4\text{-}5)$$

where υ is the frequency of attempts (successful or otherwise) of dislocations to jump energy barriers, l the pinning distance, d the length of thermal activation event, k the Boltzman constant, T the temperature and ΔG the Gibbs free energy. The frequency of successful jumps to escape obstacles (such as forest dislocations, solute atoms and small precipitates) of only forward activation was first introduced by Gibbs (Gibbs, 1969). The schematic diagram of a dislocation escaping an obstacle from the corresponding energy barrier is shown in Fig. 4-1. More recently, Dunne (Dunne et al., 2007) considered both forward and backward activation events to obtain a slip rule. The Gibbs free energy is equal to the difference between the Helmholtz free energy and the work done by the stress,

$$\Delta G = \Delta F - \tau \Delta V \qquad (4\text{-}6)$$

where ΔF is the Helmholtz free energy or thermal activation energy, τ the shear stress and ΔV the activation volume. Thus, the shear strain rate on the ith slip system for applied resolved shear stress τ^i exceeding the critical resolved shear stress τ_c^i was

then found to be

$$\dot{\gamma} = \rho_m b^2 \upsilon \exp\left(-\frac{\Delta F}{kT}\right) \sinh\left(\frac{\Delta V}{kT}\left(\tau^i - \tau_c^i\right)\right) \qquad (4\text{-}7)$$

where a further approximation is considered as $d \approx l$. From Equation (4-7) thermal activation energy ΔF and activated volume ΔV are key parameters controlling the strain rate in a specific slip system at a given temperature.

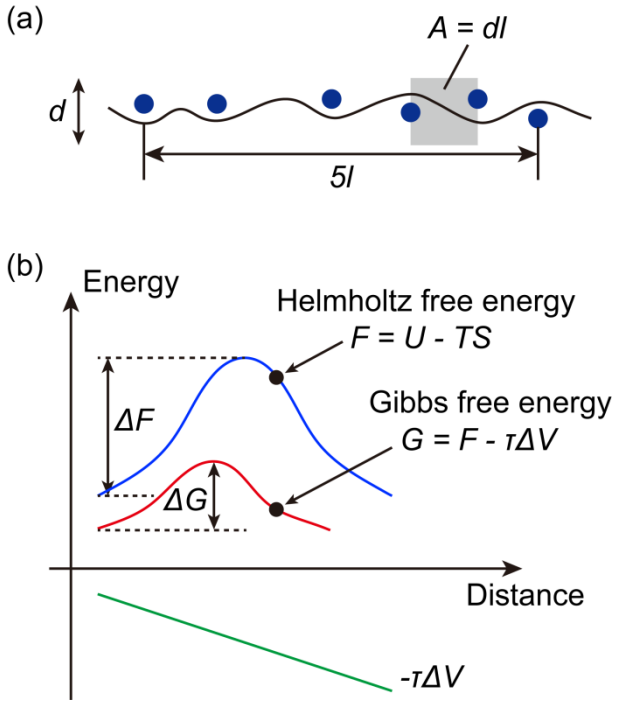


Fig. 4-1. Schematic diagram of (a) a dislocation escaping an obstacle through a thermal activation process and (b) the corresponding energy barrier curves (Dunne et al., 2007; Granato et al., 1964; Zheng et al., 2016b).

4.2.2. Experimental methods

As one of the common methods to investigate rate dependent behaviour, creep testing involves loading a tensile or compression sample to a specific stress value, then holding

at constant stress while measuring the strain evolution over time. In this study, a stress-controlled three-point bend compression was applied on an edge-notched beam sample (Sample MZ), which was originally cut by EDM from a rolled Zircaloy-4 plate. Fig. 4-2 (a) shows the optical microscope image of the edge notch, which is located at the middle bottom of the beam. The geometry of Sample MZ is detailed in Table 4-1. Heat treatment was applied on as-received fine-grain Zircaloy-4 before cutting to achieve blocky alpha microstructures as introduced in Chapter 3. The creep test was carried out through a load-controlled three-point bend testing after annealing the sample at 500 °C for 1 hour to eliminate the residual stress near the notch introduced by EDM cutting. The beam sample was firstly loaded up to 800 N with force rate 10 N/s, and then was held at a constant peak force, 800 N for 3600 s. Finally, the sample was unloaded to 0 N. The loading history with force versus time is shown in Fig. 4-2 (b).

Table 4-1. Beam geometries and notch shape of Sample MZ.

Sample	**Geometry (mm)**	**Notch Shape (μm)**
MZ	Height 3.28 Thickness 2.80 Length 12.01	Notch Height 270 Notch Width 150

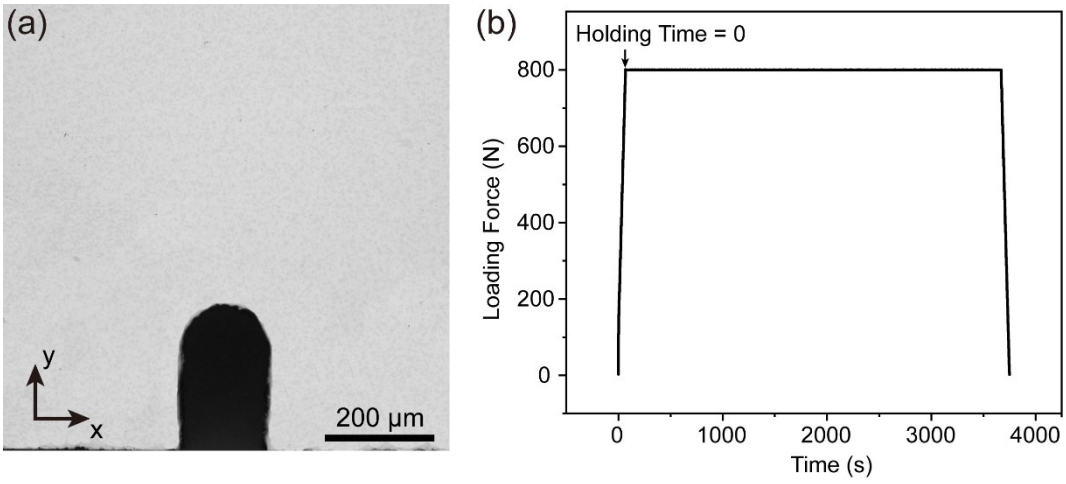


Fig. 4-2. (a) Optical microscope image of the edge notch at the middle bottom of the beam sample; (b) loading history of the three-point bend creep test.

In-situ optical microscope observation was utilised via a setup involving a Questar 100 lens and a CCD camera controlled by computer, of which the resolution can achieve around 1 μm. Speckles with size of 1 μm were sprayed on sample surface. The speckle images were recorded in-situ with a time interval of 0.5 s throughout the whole creep process. After creep testing the images corresponding to holding times at 0 s, 5 s, 10 s, 20 s, 30 s, 60 s, 120 s, 180 s, 300 s, 600 s, 1200 s, 1800 s, 2400 s, 3600 s and in the final unloaded condition for the creep test coupling with the first image from the undeformed condition were extracted for in-plane strain fields calculation by the in-house Matlab code introduced in Chapter 3.

4.3. Microstructural characterisation

Fig. 4-3 shows the SEM image (a) and inverse pole figure (IPF) (b) along the Z-direction near the notch of Sample MZ. A typical blocky alpha microstructure is

observed with large grains size of around 300 μm and small grains (< 20 μm) distributed at the grain boundaries or within large grains as island grains. The blocky alpha microstructure inherits the strong basal texture from as-received small grain materials with the c-axes of grains in Sample MZ aligned with the Z-direction. The crystallographic orientations of the main large grains (labelled as Grain M1, M2, M3, M4 and M5) are represented by hexagons as shown in Fig. 4-3 (a).

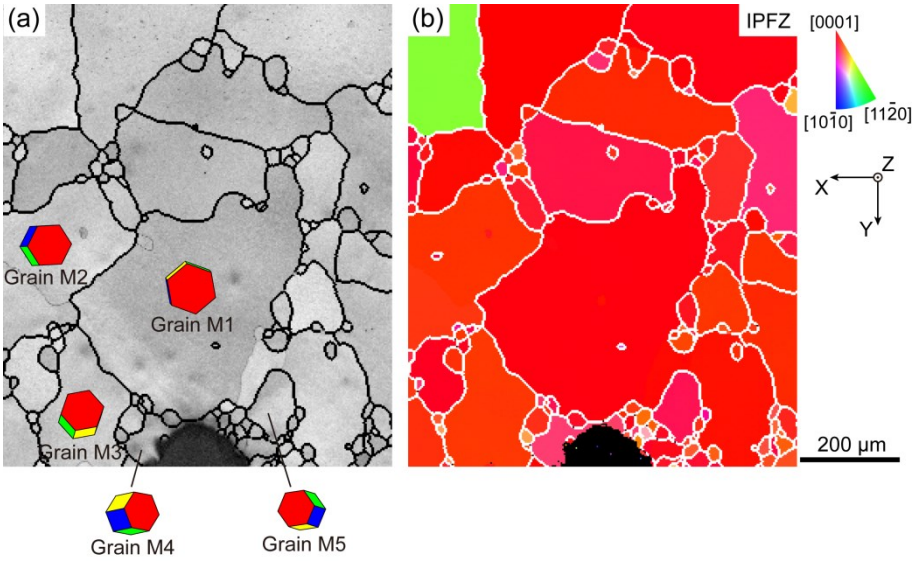


Fig. 4-3. (a) SEM image and (b) IPFZ showing grain morphologies and crystallographic orientations near the notch of Sample MZ.

4.4. Local strain evolution in creep test

In-situ optical DIC technology allows the local strain measurement throughout the creep test. Fig. 4-4 shows the total strain (xx) evolution in the ROI corresponding to the holding time from 0 s to 3600 s and in the unloaded condition in Sample MZ. The strain (xx) shows strong localisation at the notch root and develops towards two sides forming

‘wing’ bands. At the beginning of the load holding, strain (xx) is more concentrated near the notch edge, however, the development of the ‘wing’ bands becomes significant after load holding for 30 s with the strain localisation bands spreading to broader areas. After holding for 1800 s, the ‘wing’ bands stabilise and show evident asymmetry. This asymmetry is attributed to the effect of local microstructures such as grain boundaries and crystallographic orientations on slip activation.

The strain evolution during the hold period is irreversible and thus gives rise to creep and plastic strain accumulation. The strain measured in the unloaded condition is approximately equal to the plastic strain if the elastic strain is considered to be fully recovered. As shown in Fig. 4-4 (o) the plastic strain (xx) distribution, similar to the strain (xx) fields when holding, is sensitive to the local microstructures. The ‘wing’ band of plastic strain (xx) fields in the right side is interrupted by the grain boundary between Grain M1 and Grain M5.

Fig. 4-5 shows the variations of strain (xx) along a path marked as red dashed line in Fig. 4-5 (a) at different holding time corresponding to represented colour lines. The total strain (xx) gradually increases with creep time presented by the lines going up with holding time increasing. The strain (xx) variation plots show three obvious peaks as shown in Fig. 4-5 (b). The first peak corresponds to the strain localisation band at left side while the next two is attributed to strain localisation within the band at right side. The strain (xx) of the first peak along the path increases from 0.45 at holding for 0 s to 1.09 at holding for 3600 s.

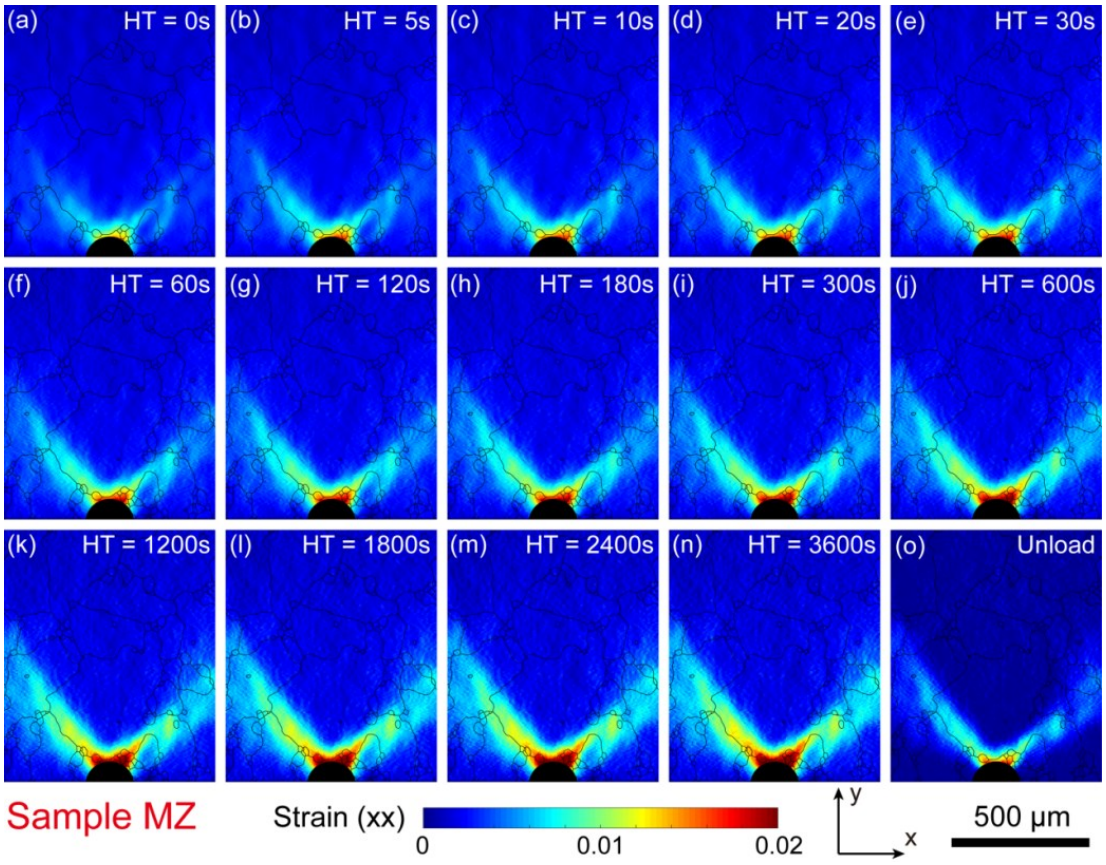


Fig. 4-4. Experimentally measured total strain (xx) evolution distributions (a-n) at holding time from 0 s to 3600 s; and (o) in the unloaded condition in Sample MZ.

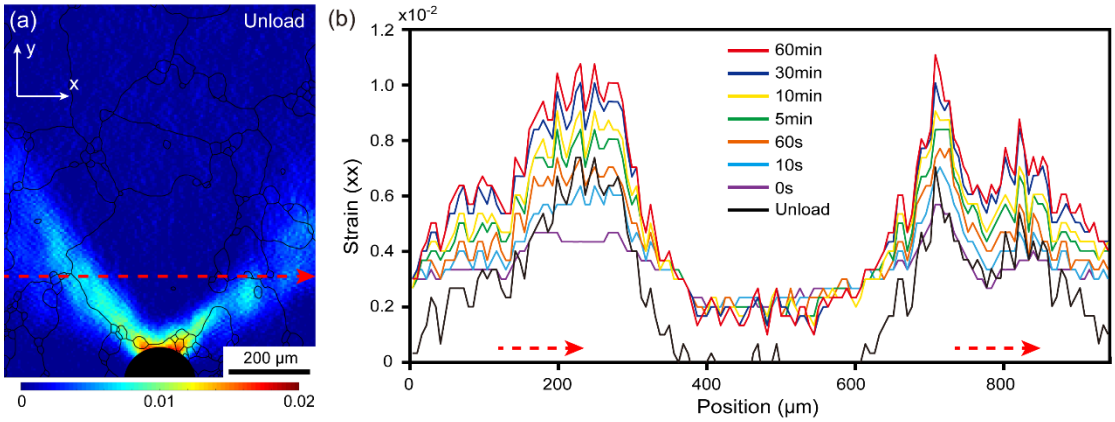


Fig. 4-5. (a) Strain (xx) field in the unloaded condition; (b) strain (xx) variations along the red dashed line marked in (a) at different hold time.

4.5. CPFE modelling of notched sample in creep and comparisons with experiment

A microstructurally faithful CPFE model was developed (Liu et al., 2020) representing the experimental results, in which the reproduction of free-surface grain morphology and crystallographic orientations in the ROI is based on the EBSD examination. Grain geometry and orientations were imported into the commercial finite element platform ABAQUS via in-house developed python scripts. Fig. 4-6 (a) shows the schematic of the finite element modelling of the three-point bend testing on an edge-notched beam sample with the load of 800 N applied on the middle area of the top surface. A sub-model, which contains the ROI was extracted to address the crystal elasto-plasticity simulation by extruding the surface geometry 50 μm in the Z-direction maintaining plane stress conditions on the free surface as shown in Fig. 4-6 (b). The gradient loads applied to the sub-model is equivalent to the load condition in the three-point bend full model by correlating the stress (xx) along a specific path. The boundary conditions of the full model and the sub-model are shown in Fig. 4-6.

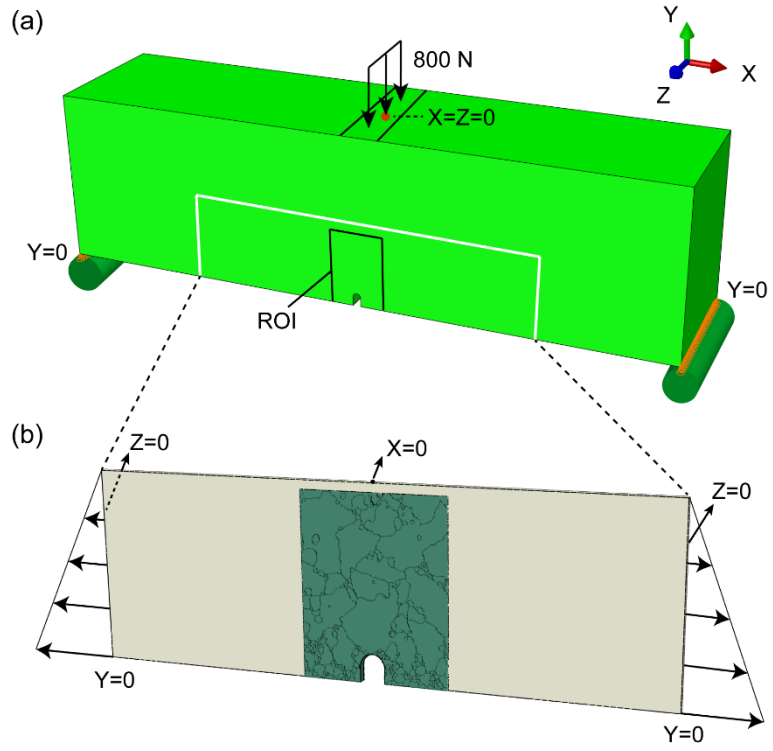


Fig. 4-6. (a) Full finite element model of three-point bend testing on an edge-notched beam sample; (b) sub-model in the truncated area of full model.

4.5.1. Slip activation

Slip activation in creep test of polycrystal Zircaloy-4 can be estimated by calculating the local Schmid Factor (SF). Herein, we are focusing on the discussion of slip activations in Grain M1, Grain M2 and Grain M3 as examples (defined in Fig. 4-3). The Euler angles of the grains were extracted from the EBSD results, and then the maximum Schmid Factors of <a> prismatic slip, basal slip, and <c+a> pyramidal slip in the individual grains were obtained as detailed in Table 4-2 (assuming a uniaxial remote stress state along the x-direction). It is concluded that the prismatic slip is the preferable slip system given the loading and crystallography according to the similar discussion in Chapter 3. However, the Schmid Factors only gives the qualitative

estimation of slip systems. The CPFE modelling helps address the slip activation in quantitative magnitudes. Fig. 4-7 shows the distributions of resolved shear strain, γ corresponding to three prismatic slips in Grain M1 from the simulation results. The slip planes and slip directions are marked in hexagons. The Prismatic Slip 1, which is marked in green, is the preferable one among the three with the highest resolved shear strain and local Schmid Factor (0.49). Prismatic Slip 1 is localised at area near the grain boundaries likely along the plastic strain bands shown in Fig. 4-4 (o).

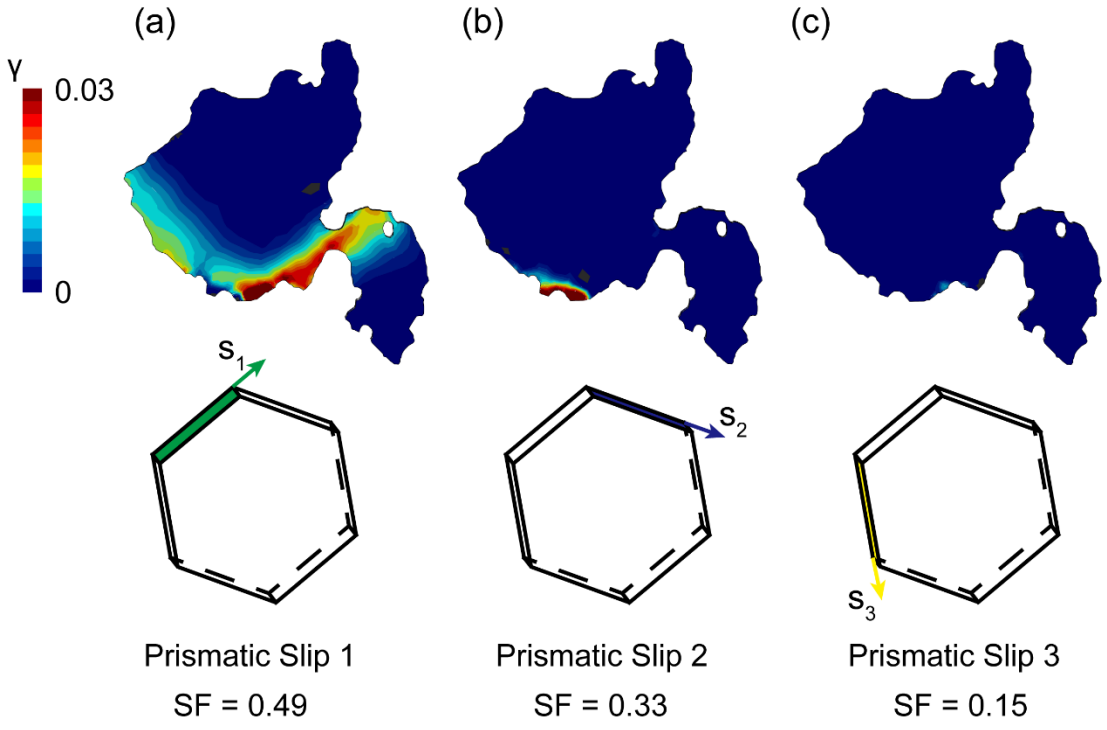


Fig. 4-7. CPFE modelling results showing distribution of the resolved shear strain γ of prismatic slip systems in Grain M1 when creep holding for 3600s: (a) Prismatic Slip 1; (b) Prismatic Slip 2; (c) Prismatic Slip 3 (Liu et al., 2020).

Table 4-2. Grain Euler angles and slip system maximum Schmid Factors in Sample MZ.

Grain	Euler Angle	Maximum Schmid Factor		
		Prismatic Slip	Basal Slip	Pyramidal Slip
M1	(218, 4, 151)	0.49	0.04	0.45
M2	(271, 12, 62)	0.44	0.2	0.49
M3	(345, 14, 356)	0.49	0.06	0.46

4.5.2. Strain evolution

The CPFE modelling results of total strain (xx) distribution when load holding for 0 s, 30 s, 300 s, 1200 s, 3600 s, and in the unloaded condition are shown in Fig. 4-8 compared with the experimental results. The numerical results of strain (xx) fields show good consistence with the experimental DIC results in both quantities and distributions indicating strong creep response at room temperature in Zircaloy-4. Fig. 4-9 (b) shows the average total strain (xx) evolution of the area in the white dashed rectangular over holding time. The average total strain (xx) increases from 0.28% to 0.43% throughout the holding time. The strain (xx) shows a rapid increase at the beginning of the creep within 180 s and then the strain rate becomes gradually lower with the holding time going on. The total strain (xx) variation at point P, which represents the hotspots of the strain (xx) fields near the notch, is shown in Fig. 4-9 (c). The strain (xx) at P increase from 1.13% to 2.23% holding from 0 s to 3600 s, which indicates a much larger creep rate than the average value.

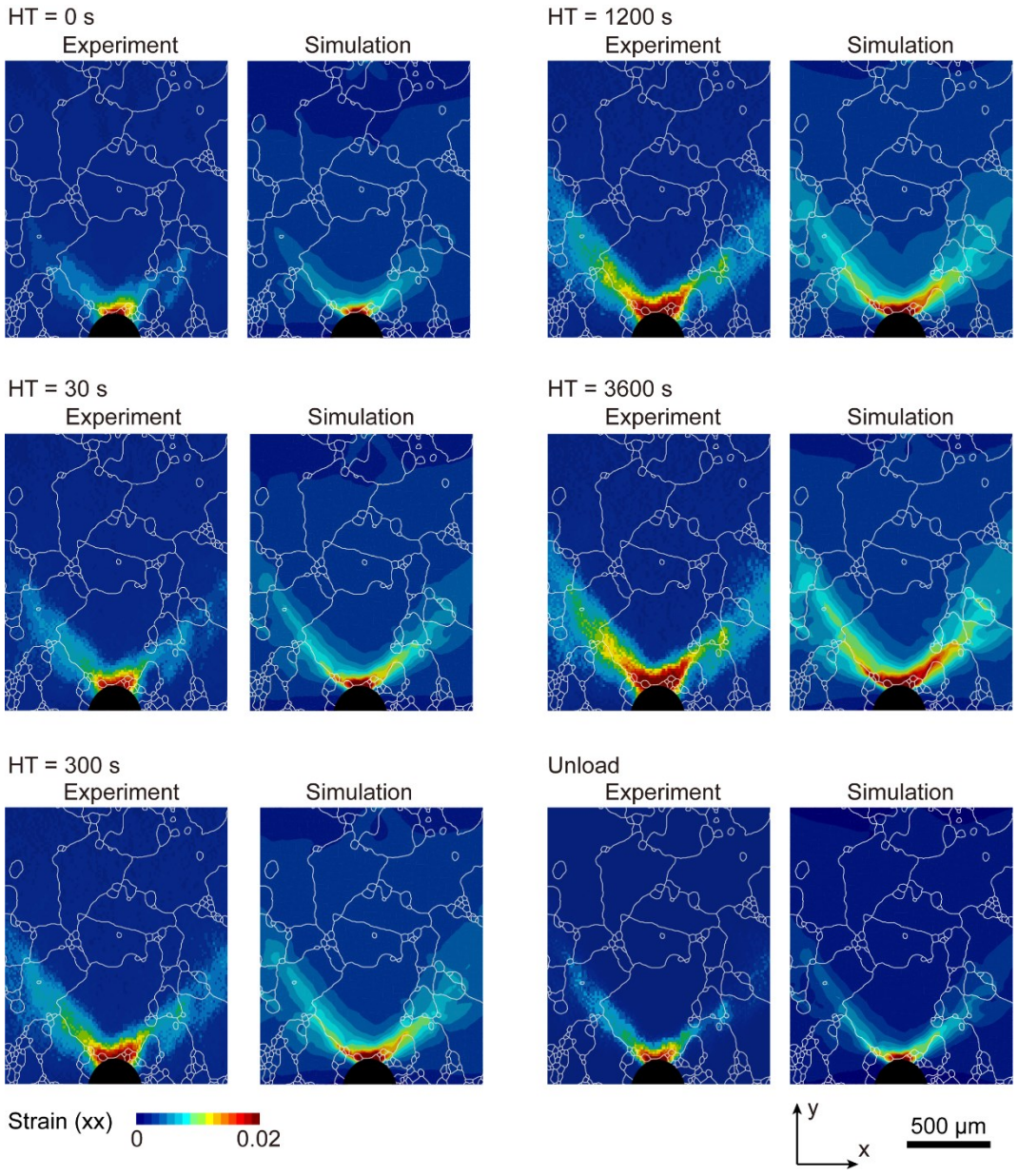


Fig. 4-8. Strain (xx) distribution near the notch from CPFE simulations compared with DIC results at different holding time frame of (a) 0 s, (b) 30 s, (c) 300 s, (d) 1200 s, (e) 3600 s and (f) in the unloaded condition.

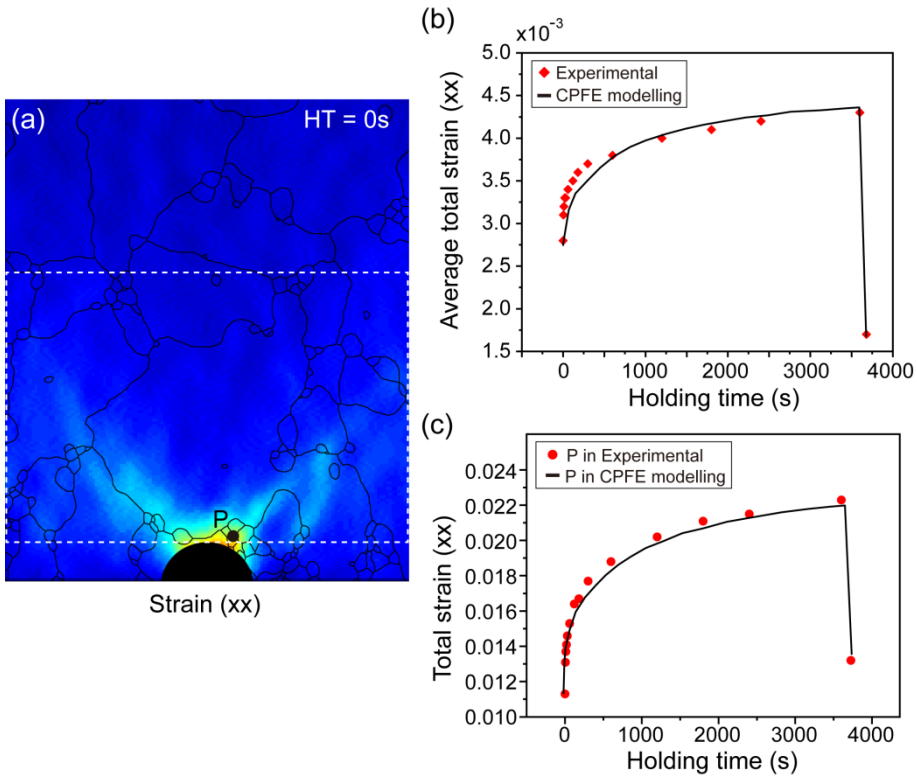


Fig. 4-9. (a) Strain (xx) field near the notch at the start of holding; (b) the average strain (xx) evolution of the white dashed area marked in (a); (c) strain (xx) evolution of point P marked in (a).

4.5.3. Stress distribution at the end of holding

Experimental DIC measurement and CPFE modelling both demonstrate considerable creep strain accumulation near the notch in Zircaloy-4. The corresponding stress redistribution which results from the inhomogeneous creep strain could have a very significant effect on local (hydrostatic) stress levels, particularly in the context of stress raisers (dominated by the notch in the present work, but also strongly affected by local microstructures such as grain boundaries). Hence an experimental measurement on local stress distribution in the ROI and subsequently comparison with simulation results

are of significance to further understand the creep behaviour in Zircaloy-4.

In three-point bend testing the applied load on the top middle of the beam sample contributes to tensile stress along the x-direction at the base. With an edge notch stress concentration, however, the stress state near the notch is not accessible by a traditional beam theory calculation. A method is introduced to determine the stress distribution near the notch from in-situ DIC total and plastic strain measurements, utilising EBSD detection for crystallographic orientation information such that comparisons can then be made with the CPFE simulation result.

According to the loading history Sample MZ was unloaded after holding for 3600 s from 800 N (peak load) to 0 N (unloaded condition) such that the strain obtained in the unloaded condition is approximately equal to the plastic strain $\boldsymbol{\varepsilon^p}$ when the residual elastic strain is ignored. The strain measured at the peak load is considered to be the total strain $\boldsymbol{\varepsilon^t}$, which is the sum of the plastic strain $\boldsymbol{\varepsilon^p}$ and the elastic strain $\boldsymbol{\varepsilon^e}$**.** Thus, the elastic strain can be extracted from the difference between the total strain and the plastic strain:

$$\boldsymbol{\varepsilon^e = \varepsilon^t - \varepsilon^p} \qquad (4\text{-}8)$$

From Hooke's law, the stress is given by

$$\boldsymbol{\sigma = D\varepsilon^e} \text{ or } \boldsymbol{\varepsilon^e = C\sigma} \qquad (4\text{-}9)$$

where $\boldsymbol{D}$ is the (global) anisotropic stiffness matrix after rotation to account for

crystallographic orientation, $\boldsymbol{C}$ the (global) compliance matrix after rotation where $\boldsymbol{C} = \boldsymbol{D}^{-1}$. The rotation matrix is determined by Euler angle obtained from EBSD examination as detailed in Appendix B.

$$\begin{pmatrix} \varepsilon_{xx}^e \\ \varepsilon_{yy}^e \\ \varepsilon_{zz}^e \\ \gamma_{xy}^e \\ \gamma_{yz}^e \\ \gamma_{zx}^e \end{pmatrix} = \begin{pmatrix} C_{11} & C_{12} & C_{13} & C_{14} & C_{15} & C_{16} \\ & C_{22} & C_{23} & C_{24} & C_{25} & C_{26} \\ & & C_{33} & C_{34} & C_{35} & C_{36} \\ & & & C_{44} & C_{45} & C_{46} \\ & & & & C_{55} & C_{56} \\ & & & & & C_{66} \end{pmatrix} \begin{pmatrix} \sigma_{xx} \\ \sigma_{yy} \\ \sigma_{zz} \\ \sigma_{xy} \\ \sigma_{yz} \\ \sigma_{zx} \end{pmatrix} \qquad (4\text{-}10)$$

Under plane stress conditions relevant to the front free surface of the sample, $\sigma_{zz}=\sigma_{xz}=\sigma_{yz}=0$. Thus (4-10) may be reduced to

$$\begin{pmatrix} \varepsilon_{xx}^e \\ \varepsilon_{yy}^e \\ \gamma_{xy}^e \end{pmatrix} = \begin{pmatrix} C_{11} & C_{12} & C_{14} \\ C_{12} & C_{22} & C_{24} \\ C_{14} & C_{24} & C_{44} \end{pmatrix} \begin{pmatrix} \sigma_{xx} \\ \sigma_{yy} \\ \sigma_{xy} \end{pmatrix} \qquad (4\text{-}11)$$

Then the stress tensor in plane stress can be written as,

$$\boldsymbol{\sigma} = \begin{pmatrix} \sigma_{xx} & \sigma_{xy} \\ \sigma_{xy} & \sigma_{yy} \end{pmatrix} \qquad (4\text{-}12)$$

Fig. 4-10 shows the distributions of elastic strain components (ε_{xx}^e, ε_{xy}^e and ε_{yy}^e) in the ROI when holding for 3600 s. The ε_{xx}^e is dominant compared to ε_{xy}^e and ε_{yy}^e with the maximum reaches 0.01 close to the notch. The stress distribution is easy to calculate from elastic strains following Hooke's law. Experimental results on the distributions of stress components (stress (xx), stress (yy) and stress (xy)) are compared to the CPFE modelling results as shown in Fig. 4-11. The simulation results present good correlation with the experimental results on stress distribution indicating a multiaxial stress state near the notch. However, the stress (yy) and stress (xy) are

apparently lower than the dominant stress (xx).

The CPFE modelling successfully captures the experimental creep results including local strain and local stress distributions in Zircaloy-4, in which the thermal activation slip rule well characterises the rate-dependent response. The crystal plasticity material properties parameters, especially the thermal activation energy ΔF and thermal activation volume ΔV, are calibrated based on the creep responses from the DIC measurement of Zircaloy-4 at 20 °C as shown in Table 4-3 (Liu et al., 2020).

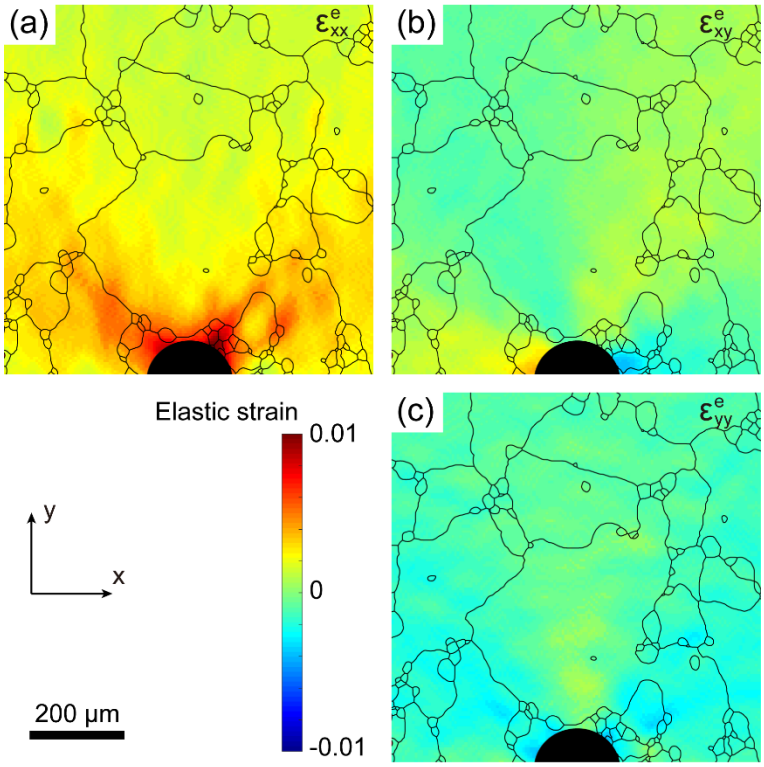


Fig. 4-10. DIC measured elastic strain component distributions of Sample MZ when holding for 3600s: (a) elastic strain (xx); (b) elastic strain (xy); (c) elastic strain (yy).

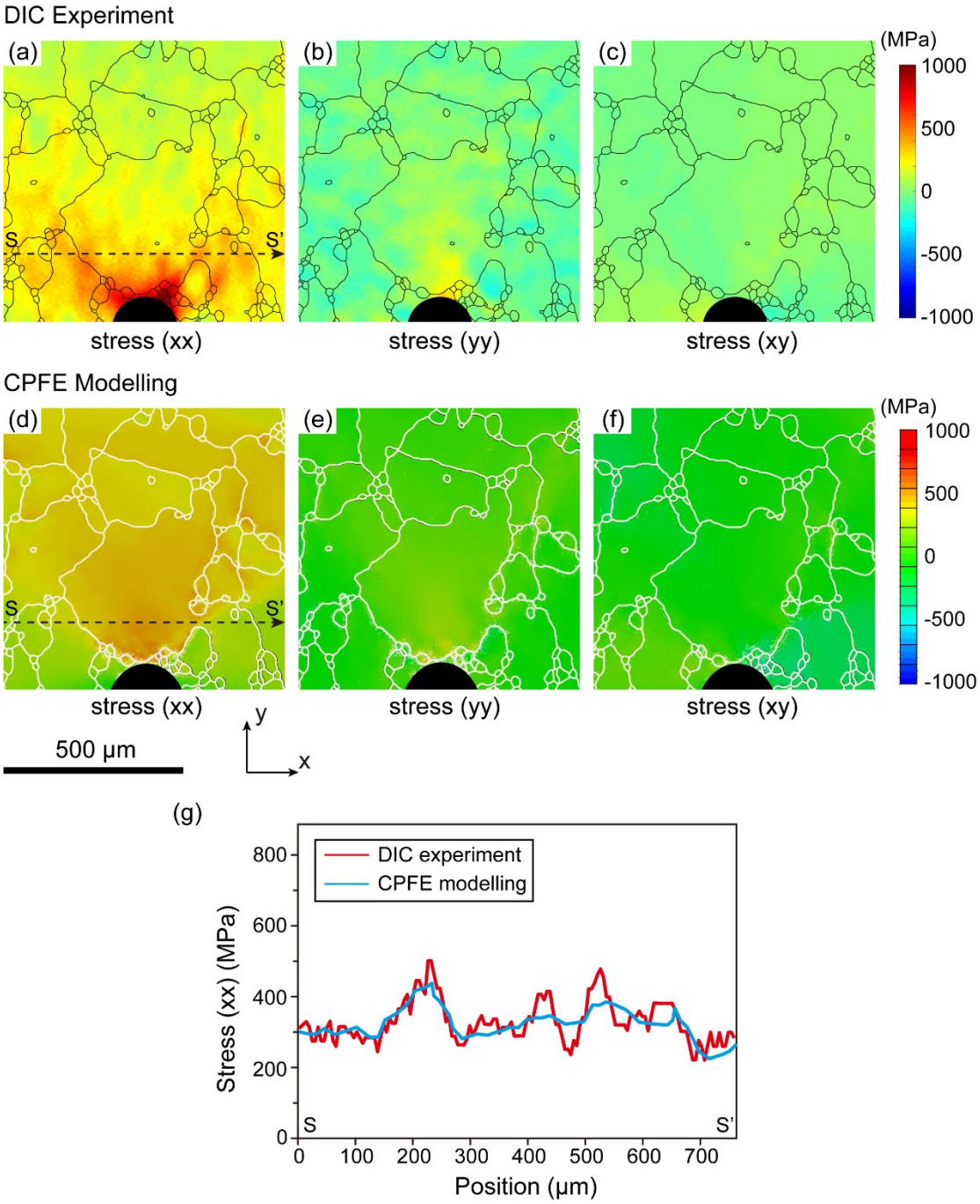


Fig. 4-11. Comparison of local stress components between DIC experiment and CPFE modelling: (a) stress (xx), (b) stress (yy) and (c) stress xy obtained from experimental results; (d) stress (xx), (e) stress (yy) and (f) stress (xy) obtained from simulation results; (g) line graph showing the stress (xx) from point S to S' as marked in (a) and (d).

Table 4-3. Plastic properties for prismatic slip of Zircaloy-4 at 20 °C (Liu et al., 2020).

τ_c (MPa)	b (μm)	ρ_m (μm^{-2})	υ (s^{-1})	k (J/K)	ΔF (eV)	ΔV (μm^3)
153	3.2×10^{-4}	0.01	1.0×10^{11}	1.38×10^{-23}	0.32	$20.93b^3$

4.6. Assessment of local strain rate sensitivity

The conventional strain rate sensitivity of polycrystalline material is described by the strain rate sensitivity index m, which accounts for the macroscopic uniaxial stress and strain rate as defined in Equation (4-1). This method is commonly used by testing a group of tensile test samples under different strain rates without considering individual microstructures in each sample. Thus the conventional strain rate sensitivity can only describe macro-scale mechanical behaviour of materials but is not able to characterise the rate dependent response on micro-level.

Recent studies on strain rate sensitivity have recognised the different deformation mechanisms such as slip versus twinning and which gives rise to differing intrinsic strain rate sensitivities for different slip systems. In particular, the intrinsic slip system strain rate sensitivity was extracted from single crystal pillar compression experiments (Jun et al., 2016b; Zhang et al., 2016). In the current study, the in-situ micro-scale strain measurement in creep test gives rise to rich data on local strain rate response coupled with grain information including morphology and orientation in Zircaloy-4. Thus it is prospective to obtain the distribution of micro-scale strain rate sensitivity (Local-SRS)

of specific slip system corresponding to the local microstructure by building up the relationship between strain rate and Local-SRS.

Regarding dislocation slip, following the previous assumptions on dislocation glide (Evans and Rawlings, 1969; Hirth and Nix, 1969), the equivalent macroscopic strain rate $\dot{\varepsilon}^i$ of an activated dislocation slip $\dot{\gamma}^i$ could be described as,

$$\dot{\varepsilon}^{p\,i} = \rho_m b^i v_g M^i = \dot{\gamma}^i M^i \qquad (4\text{-}8)$$

in which M^i is the Schmid Factor of i^{th} slip system. The equivalent stress σ^i in the remote loading direction is given,

$$\sigma^i = \frac{\tau^i}{M^i} = \frac{1}{M^i}\left[\frac{kT}{\Delta V}\sinh^{-1}\left(\frac{\dot{\varepsilon}^{p\,i}}{\eta\exp\left(-\frac{\Delta F}{kT}\right)M^i}\right) + \tau_c^i\right] \qquad (4\text{-}9)$$

where $\eta = \rho_m \nu\left(b^i\right)^2$ for convenience. Here, the relationship between σ^i and $\dot{\varepsilon}^i$ in one slip system is taken to be controlled by the thermal activation slip rule, in which τ_c^i, ρ_m, ν and b^i are fundamental physical parameters with respect to specific slip systems. Hence, the strain rate sensitivity of i^{th} slip system, m^i can be derived as (Zhang and Dunne, 2017)

$$m^i = \frac{\dot{\varepsilon}^{p\,i}}{\sqrt{\left(\eta\exp\left(-\frac{\Delta F}{kT}\right)M^i\right)^2 + \left(\dot{\varepsilon}^{p\,i}\right)^2}\left[\sinh^{-1}\left(\frac{\dot{\varepsilon}^{p\,i}}{\eta\exp\left(-\frac{\Delta F}{kT}\right)M^i}\right) + \frac{\Delta V}{kT}\tau_c^i\right]} \qquad (4\text{-}10)$$

where it is assumed to be unconstrained uniaxial and uniform deformation by single slip with no hardening. For a given slip system at certain temperature with determined ΔF and ΔV, the strain rate sensitivity is the function of strain rate, Burgers vector and

Schmid Factor. Since Schmid Factor for the preferable slip system in each grain has been obtained as shown in Table 4-2, it is possible to obtain local distributions of strain rate sensitivity with different local strain rate coupling with the microstructural information in the experimental creep test. It should be noted that it is the total strain rate which is measured from the DIC. But during the stress hold period, the macro-level stress is constant such that correspondingly, the macro elastic strain rate is zero. However, this does not imply that the local elastic strain rates are zero. However, here, the total strain rates from DIC measurements are taken to be approximately equal to the plastic strain rates, since by definition, the strain rate sensitivity depends on plasticity.

Fig. 4-12 shows the distributions of effective strain ε, strain rate $\dot{\varepsilon}$, and strain rate sensitivity, m in a selected ROI when stress holding for 5 s in (a), (e) and (i), 20 s in (b), (f) and (j), and 120 s in (c), (g) and (k) in the experimental three-point bend creep test. This ROI involves the left 'wing' of strain bands containing grains M1, M2 and M3 and the associated grain boundaries and triple junctions. The distributions of effective strains show no significant difference with that of the strain (xx).

The strain rate localises in a band which is generally consistent with the strain localisation band. This band develops along the grain boundary between Grain M1 and M3 and extends to Grain M2 due to the large amount slip activation in this area as shown in Fig. 4-7. The maximum strain rate for every holding time decreases from 2×10^{-4} s^{-1} at 5 s to 1×10^{-6} s^{-1} at 1800 s because of the saturation of slip pile-up during the creep. As a monotonic increasing function of strain rate, the Local-SRS, m for

prismatic slip shows similar distribution with strain rate. The Local-SRS reaches over 0.03 when holding for 5 s while decreases to 2×10^{-4} for 1800 s. Hence, Zircaloy-4 shows significant rate dependence with local strain rate sensitivity reaches 0.03 at room temperature with strain rate at 5×10^{-4} s^{-1} compared to other traditional rate sensitive alloys.

It is found that grain boundaries play a significant role in the distribution of Local-SRS. The Local-SRS at 5 s localises along two sides of the grain boundary between Grain M1 and Grain M3. The variation of Local-SRS along a path A - B as marked in Fig. 4-12 (a) is shown in Fig. 4-13. The Local-SRS in Grain M1 is apparently larger than that in Grain M3 with an obvious rise from A to B.

The Local-SRS obtained in this study is dependent on thermal activation energy ΔF, activated volume ΔV and Schmid Factor according to Equation (4-10), which suggests that the Local-SRS represents the intrinsic anisotropy of individual slip system (prismatic slip in Sample MZ) (Zhang et al., 2016). There is considerable experimental evidence that the intrinsic slip system strain rate sensitivity is anisotropic, which means slip systems have different strain rate sensitivity values (Jun et al., 2016b, 2016a; Wang et al., 2018). The dependence of strain rate sensitivity on texture or crystallographic orientation is primarily attributed to the differing strain rate sensitivities of the individual slip systems, which ultimately determines the macroscopic value. Skippon et al (Skippon et al., 2019) measured 'lattice rate sensitivity', which is equivalent to intrinsic slip system strain rate sensitivity, by using in-situ synchrotron x-ray diffraction

elastic strain measurement. Their result shows that the prismatic slip strain rate sensitivity is around 0.03 when the strain rate in the order of 10^{-4} which is consistent with the Local-SRS value shown in Fig. 4-12 (i).

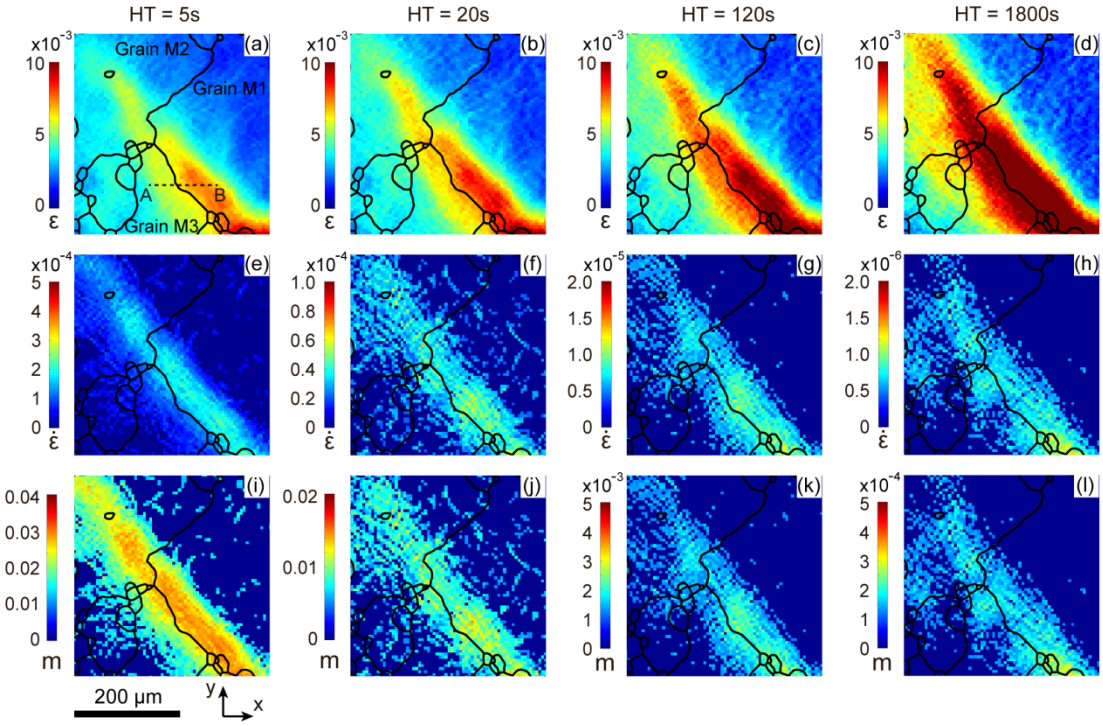


Fig. 4-12. Effective strain ε, strain rate $\dot{\varepsilon}$, and strain rate sensitivity m distribution when stress holding for (a) (e) (i) 5 s, (b) (f) (j) 20 s, (c) (g) (k) 120 s and (d) (h) (l) 1800 s in a creep test.

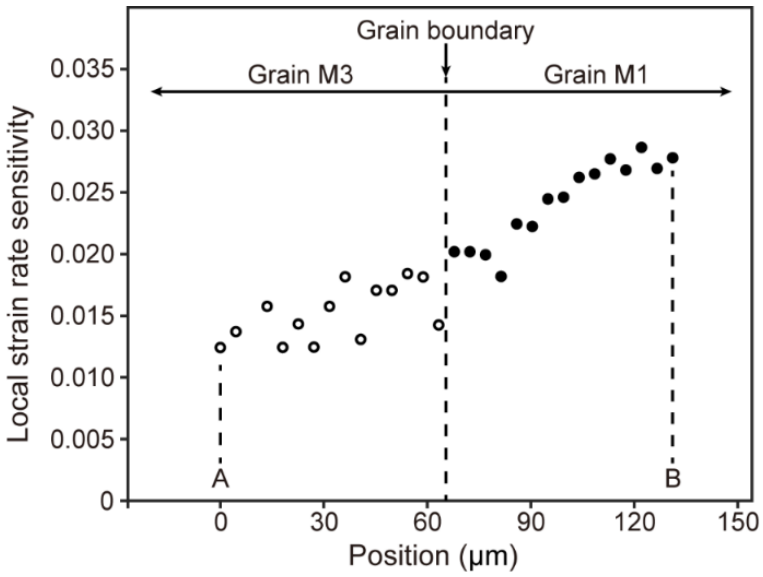


Fig. 4-13. Local strain rate sensitivity (HT = 5 s) variation along path A-B across the Grain boundary between M1 and M2.

4.7. Conclusions

The local strain evolution near an edge notch has been studied in a three-point bend creep test via in-situ DIC technique. A new approximate methodology has been used to estimate stress distribution near the notch at the end of a constant stress (creep) hold. The experimental results have been compared to CPFE modelling result with good correlation, which indicates the reliability of the new experimental method. The main conclusions are obtained as follows:

1. Strain localisation occurs near the notch in the creep test of a Zircaloy-4. The strain bands develop along grain boundaries forming a ‘wing’ shape. The plastic strain accumulation is attributed to the activation of prismatic slip.

2. The plastic deformation of zirconium is rate sensitive at room temperature. The

micro-scale strain rate sensitivity reaches approximately 0.03 when the strain rate is 5×10^{-4} s^{-1}.

3. Local strain rate sensitivity at low strain rate is controlled by the thermal activation slip rule. Local microstructure features such as grain boundary have great effect on micro-scale strain rate sensitivity.

5. Stored energy - Driving force for short crack growth

5.1. Introduction

Crack growth life estimation is of significant practical importance in fatigue life prediction strategies. Knowledge of estimating crack growth rates is the key to understanding the crack growth behaviour. Such approaches to describe crack propagation can be categorized from the parameters used for the driving forces. The early driving force for crack growth starts from Griffith-Irwin failure criterion then expands to the stress intensity factor, J-integral and CTOD which have been reviewed in Chapter 2.

A damage accumulation criteria has been proposed to model fatigue crack growth, which mostly treats crack growth as a process of continuous crack nucleation (Chowdhury and Sehitoglu, 2016; Glinka, 1982; Jiang and Feng, 2004). In this approach, a critical amount of accumulated damage is considered as a threshold for the crack to advance. Glinka (Glinka, 1982) built up a cumulative model of fatigue crack growth in which the crack growth rate is argued to depend on the width of the highly strained zone at the crack tip, and it can be calculated by means of the local stress/strain. Farukh et al (Farukh et al., 2015) applied a strain accumulation criterion to model a dwell fatigue test assuming the crack to grow when the accumulated plastic strain ahead of the crack tip reached a critical value. More recently, cumulative energy-based criteria (Golos and Ellyin, 1988; Huffman, 2016; Lefebvre and Ellyin, 1984; Skelton, 1991) have been widely used to characterise the crack growth. For example Skelton and co-

workers (Skelton, 1991; Skelton et al., 1998, 1996; Skelton and Loveday, 1997) suggested that the cumulative energy per cycle at saturation was constant such that the cyclic dissipated energy density, represented by the area of the hysteresis loop per cycle, could be considered to be the driving force to propagate a crack.

With the aim to predict the fatigue crack propagation, behaviour relationships were explored between crack growth rate and fatigue loading parameters. Over a limited range (long crack), a log-log plot of the fatigue crack growth rate, da/dN, versus the stress intensity factor range, ΔK, is empirically found to be nearly linear, known as Paris law, (Paris and Erdogan, 1963). However, this relation is not reliable for short crack growth, which is sensitive to microstructures such as crystallographic orientation and grain boundary. Not only stress intensity factor, other single parameter methods such as the J-integral or CTOD are also not reasonable to solely describe microstructurally short crack growth. Different from the long crack with the driving force dominated by principal stress, the driving force of the short crack accounts for local microstructures and the stress state near the crack tip. The main features of short crack growth are summarised as follows:

1. Microstructurally sensitive short crack is often found to grow along specific slip planes, which can be dependent on grain orientation, resulting in tortuous paths for transgranular short crack growth (Andersson and Persson, 2004; King et al., 2011).

2. The crack growth rate of short crack sees fluctuation due to microstructural obstructions such as grain boundary (King et al., 2011).

3. The stress localisation at the crack tip account for slip activation.

To identify the driving force for short crack growth, an early study from Forsyth (Forsyth, 1963) proposed that the driving force for short crack growth was maximum shear stress. Radon (Radon, 1982) proposed a damage accumulation model for fatigue crack growth in a threshold region with a plastic-strain fracture criterion assuming that crack growth can occur only when the plastic strain ahead of the crack tip reaches the fracture plastic strain. Wilkinson et al (Wilkinson et al., 1998) proposed that dislocation gliding on slip planes is argued to drive the short crack growth through the transition between interstitial dipoles and vacancy dipoles.

Although quite a few theoretical models exist for short crack growth, few experimental investigations have been performed to reveal the mechanism of fatigue crack growth at the grain length scale. In a recent experimental study on a ferritic strainless steel, Malitckii et al (Malitckii et al., 2018) demonstrated that short crack growth was driven by local shear strain and dominated by local slip system, and the crack growth rate was related closely to the shear strain localisation zone determined by a DIC measurement.

In this chapter, an experimental measurement coupling with in-situ DIC and EBSD technologies on stored energy density is utilised to provide new insights into the microstructurally-sensitive short crack growth in a textured Zircaloy-4. We will start with a detailed review of literatures on stored energy, followed by an introduction of the materials and methods applied in the experiments. In the results, a succession of micromechanical quantities relating to the fatigue tests including local strain, local

stress, cyclic dissipated energy and cyclic stored energy density are addressed in the experiments such that the driving force for the short crack growth is discussed.

5.2. Dislocation-based stored energy density criterion

Prior to investigating the driving force for the short crack growth by quantitative experimental measurements, the context and review of the literature on stored energy is first presented. In plastic deformation it is found that a small percentage of the work done in deformation of ductile material is stored in irreversible slip by dislocations, and such stored energy is proportional to the strain (Stroh, 1953). In early studies, Stroh (Stroh, 1954) proposed that the crack formation is attributed to the dislocations pile up under stress concentration. Cyclic plastic strain localization in persistent slip bands (PSBs) is a very important early feature of crack nucleation (Man et al., 2009; Sangid et al., 2011a; Sauzay and Gilormini, 2002).

A dislocation-based model was proposed by Tanaka and Mura (Tanaka and Mura, 1981) relating the stored strain energy to crack initiation, which is essentially the stored energy of dislocations. In their model the layers of dislocation dipoles on PSB can be transformed into a free surface once the stored strain energy of accumulated dislocations reaches the surface energy. Here the surface energy is defined by the Griffith energy for fracture which accounts for the debonding of two atomic planes. Considering Gibbs free energy change (ΔG) from a state of dislocation pile-up to that of virtual crack initiation, the energy balance can be written as (Mura and Nakasone, 1990)

$$\Delta G = -W_e - \frac{A}{2} N_i \delta + A\gamma_s, \qquad (5\text{-}1)$$

where W_e is elastic energy release, δ cyclic internal stored energy, A total area of virtual crack (two crack planes) and γ_s surface energy. By minimizing ΔG the critical cycle number required to crack nucleation can be estimated as the initial state of dislocation accumulation along the slip band reaches an energetically unstable state leading to the nucleation of a microcrack within the PSB (Naderi et al., 2016; Venkataraman et al., 1990).

The stored energy, which depends on the microstructural length scale, represents the energy that is stored in dislocation structures driven by plastic strain energy under fatigue process. Bhat et al (Bhat and Fine, 2001) introduced a constant energy efficiency factor demonstrating that only a small portion of the irreversible energy is stored as dislocations while the majority is converted to heat. Considering the stored energy is not distributed evenly throughout the microstructure but is primarily in the slip bands, Fine and Bhat (Bhat and Fine, 2001; Fine and Bhat, 2007) introduced a slip bandwidth t relating the stored energy to hysteresis loop parameters through the following equation:

$$\frac{d\delta}{dN} = ft\Delta\sigma\Delta\epsilon_p, \qquad (5\text{-}2)$$

where δ is stored energy, N cycle number, f energy efficiency, $\Delta\sigma$ and $\Delta\epsilon_p$ the stress and plastic strain ranges in the cycle. However, the microstructure length scale which accounts for a maximum slip bandwidth in Fine and Bhat's model was assumed

to be constant (Fine and Bhat, 2007), which is likely not true for a dynamic crack-tip.

Recently a new criterion, critical stored energy density, has been proposed by Wan et al (Wan et al., 2014) for fatigue crack nucleation in a crystal plasticity finite element model. In this model, a physically based length scale λ, which accounts for the resultant SSD and GND mean free distance, has been expressed as

$$\lambda = \frac{1}{\sqrt{\rho_{SSD}+\rho_{GND}}} \qquad (5\text{-}3)$$

The stored energy density is driven by plastic strain energy under fatigue process, and thus is given by (Wan et al., 2014)

$$G = \int \frac{|\xi \boldsymbol{\sigma} : d\boldsymbol{\epsilon_p}|}{\sqrt{\rho_{SSD}+\rho_{GND}}} \qquad (5\text{-}4)$$

where ξ, assumed to be constant (5%) during fatigue process, is the fraction of plastic deformation work stored in the material, $\boldsymbol{\sigma}$ local stress tensor, and $\boldsymbol{\epsilon_p}$ plastic strain tensor.

The stored energy density for crack nucleation therefore accounts for local stress and strain, local slip accumulation and dislocation density. This stored energy density criterion, which has common features with both Griffith fracture energy and Stroh dislocation-based nucleation argument, unifies the contributions to fatigue crack nucleation from several microstructural quantities (local slip accumulation, local stress, local strain and dislocation density) (Chen et al., 2018). Chen et al (Chen et al., 2017) successfully applied the stored energy density criterion to identify the fatigue crack

nucleation site in a group of three-point bend tests on Ni-based single and oligo crystals, in which the primary crack nucleation site and also the second nucleation site were unambiguously captured. Wan et al (Wan et al., 2016) achieved a good prediction of the fatigue life in a polycrystalline Ni alloy by utilising the stored energy density criterion.

It is argued that the stored energy density is necessary and sufficient to drive crack nucleation. On this base, Wilson et al (Wilson et al., 2019, 2018; Wilson and Dunne, 2019) extended the application of the stored energy density criterion to characterise fatigue crack growth and achieved promising progress. Wilson et al (Wilson et al., 2019) addressed short crack growth by integrated crystal plasticity eXtended Finite Element (XFEM) modelling and experimental observation in a succession of ductile metals including HCP titanium (Ti-6Al-4V) and zirconium (Zircaloy-4), a BCC ferritic steel and a FCC Ni superalloy, which provided a range of crystallographic structures, grain morphologies and loading conditions. Their results showed that the microstructurally-sensitive short crack growth was found to be controlled by crack tip stored energy density.

Stored energy density, considered as a potential driving force for short crack growth, is difficult to measure in experiments. In this study, we propose a new experimental method to calculate the stored energy density based on 2D in-situ DIC measurement in a cyclic three-point bend testing. The methods to carry out the experiments and the mathematics to achieve the calculation will be detailed in the next section.

5.3. Experimental

5.3.1. Fatigue test

Two edge-notched Zircaloy-4 beam samples (Sample AZ and BY) with large-grain polycrystal microstructures were cyclically loaded in three-point bend tests. The details of the three-point bend set-up are introduced in Chapter 3. Samples AZ and BY share similar geometries and the same loading conditions as detailed in Table 5-1. A cyclic load was applied on the top of the beam sample in the three-point bend testing with the maximum load at 800 N and stress ratio at zero.

Table 5-1. Summary of sample geometry including edge-notch shape and loading conditions in Samples AZ and BY.

Sample	Geometry (mm)	Notch Shape (μm)	Maximum Load (N)
AZ	Height 3.18 Thickness 3.02 Length 12.01	Notch Height 300 Notch Width 150	800
BY	Height 3.18 Thickness 3.01 Length 12.02	Notch Height 310 Notch Width 150	800

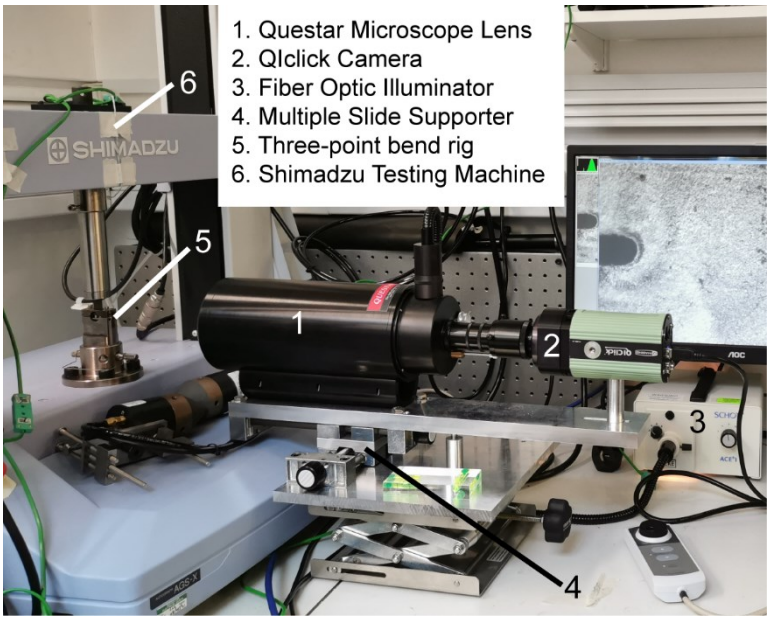


Fig. 5-1. In-situ micro-scale optical digital image correlation set-up.

5.3.2. In-situ optical DIC

In situ optical DIC test was carried out as a setup shown in Fig. 5-1, which includes a Questar microscope lens (QM-100), a QIclick versatile scientific CCD camera, a three-point bend testing rig and a three-axis sliding supporting stage. The three-point bend testing setup was applied on a Shimadzu universal testing machine. The Questar microscope lens was connected with the camera by a C-mount adaptor with a fiber optic illuminator supplying coaxial illumination. The lens was mounted on a supporting stage which allows sliding along XYZ directions, and the camera was supported by a screwed metal cylinder attached to the supporting stage to avoid wobbling. The Questar microscope with the highest resolution of 1 μm is able to recognize the sprayed diamond speckles with size of 1 μm on the sample surface when the working distance is around 150 mm.

A succession of speckle images were simultaneously captured by the camera with an interval time of 0.5 s when the cyclic three-point bend testing was going on such that the displacement of the speckles were recorded through individual cycles and over many cycles in situ. To note, according to the strain rate sensitivity of Zircolay-4 studied in Chapter 4, it would be problematic to measure the strains at peak load by interrupting the cycling. Therefore, the speckle pattern pictures were captured in real-time without stopping the cyclic loading. The interval time (0.5 s) is short enough to capture the beam positions at peak load and in the unloaded condition during a full cycle. The obtained image size was 1392 × 1040 pixels which corresponds to a real resolution of around 1 μm per pixel. The field of view is large enough to allow the movement of the region of interest (ROI), which is convenient to be cropped in the later image processing. In this way, the images recorded at the peak load and in the unloaded condition were able to be extracted out for the strain calculation by an in-house Matlab code using a cross-correlation algorithm as introduced in Appendix A. In the (second pass) cross-correlation analysis a window size of 64 × 64 pixels ROI with 95% overlapping was used such that the spatial resolution of the strain measurement was approximately 3 μm.

5.4. Short crack path and crack growth rate

5.4.1. Microstructure and crack morphology

Microstructures of Samples AZ and BY were detected via SEM and EBSD as shown in Fig. 5-2. The grain morphologies and orientations show typical blocky alpha microstructures and a strong basal texture of Zircaloy-4. The c-axes of the grains in

Sample AZ were aligned with the Z-direction, while those in Sample BY were aligned with the Y-direction. The crystallographic orientations of specific grains are presented by hexagons in Fig. 5-2 (c) and (d).

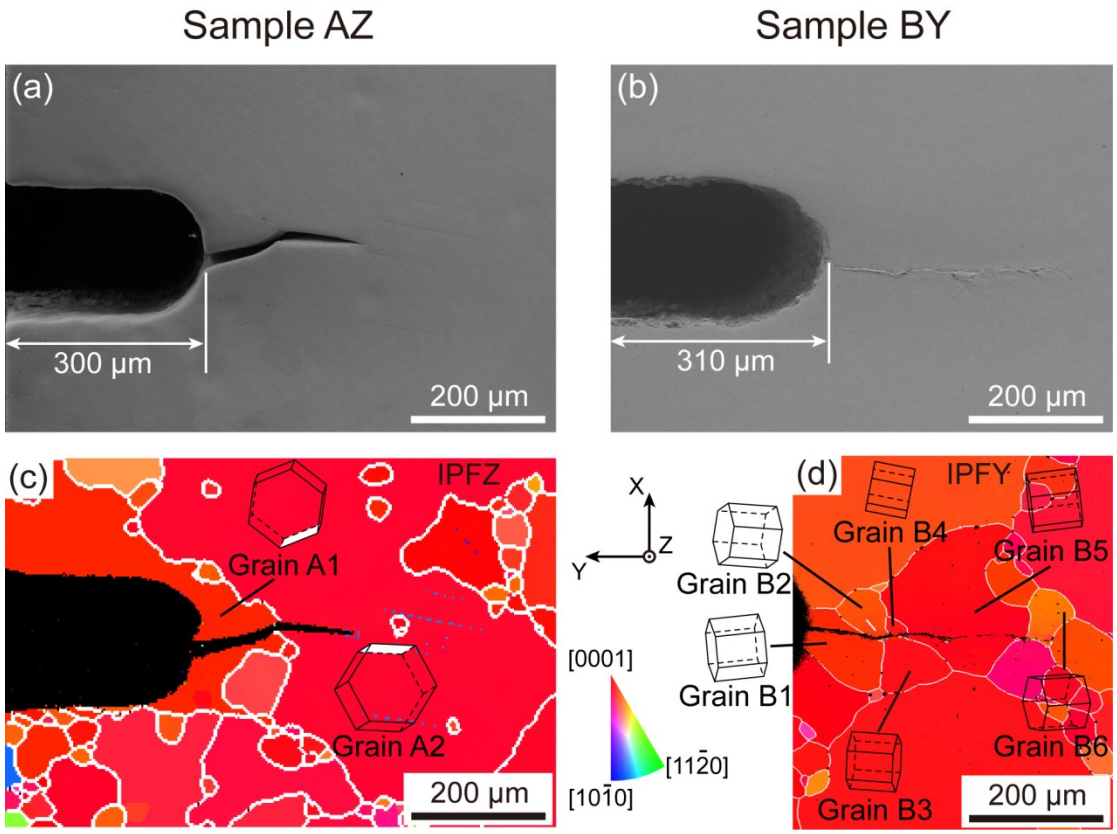


Fig. 5-2. SEM images showing notch geometries and crack paths in Sample AZ (a) and Sample BY (b); (c) IPFZ of Sample AZ; (d) IPFY of Sample BY.

Short cracks in Samples AZ and BY were observed nucleating from the edge of the notches and growing through the microstructures. The crack paths are shown in Fig. 5-2 within SEM and EBSD images after 2400 cycles for Sample AZ and 3800 cycles for Sample BY. For Sample AZ, the surface short crack goes across Grain A1 along a prismatic plane, marked in white in the hexagon. After that it goes through the grain boundary between Grain A1 and Grain A2 with an obvious deflection driving the crack

path to another prismatic plane of Grain A2 (marked in white). The surface short crack in Sample BY is also crystallographic with the crack path mostly along prismatic planes. This crack path seems more complicated than that in Sample AZ as it begins in Grain B1, and then encounters a triple junction (and probably contains a short part of the grain boundary between Grain B2 and Grain B3). After this, the crack traverses Grain B4 and Grain B5 and finally enters Grain B6. Although the surface short cracks in Samples AZ and BY both go along a prismatic plane, the path direction of the former is along the Burgers vector while the latter is perpendicular with the Burgers vector. This difference leads to the short crack propagation in textured Zircaloy-4 growing obvious anisotropically in terms of observed crack growth rates.

5.4.2. Crack growth rate

The lengths of the short cracks in Samples AZ and BY were manually measured from OM images captured at peak load at every specific cycle during the fatigue tests as the crack is fully opened at this state. The plots of crack length versus cycle number are shown in Fig. 5-3 (a) and (b) for Samples AZ and BY respectively. In Sample AZ, the crack deflection, located at the grain boundary between Grains A1 and A2, occurs before cycle 1000, and the crack length is recorded from cycle 1000 to 2400 with an interval of 200 cycles in which the whole propagation is inside a single crystal of Grain A2. The short crack growth of Sample BY is recorded from cycle 1800 to 2800 with interval of 100 cycles. The stage when the crack grows through the triple junction area is marked between two dashed red lines as shown in Fig. 5-3 (b).

The crack growth rates were then calculated from the slope of two neighbouring data points of crack length versus cycle number from Equation (3-2) with the same method used in Chapter 3. Fig. 5-3 (c) shows the crack growth rates of Samples AZ and BY versus the effective crack length, where the effective crack length is equal to the sum of the notch height and the projected crack length (the projection of crack length to the Y-direction). The trend of crack growth rate variation are marked in red and blue dashed lines for Sample AZ and BY, respectively. In this figure, two interesting features can be observed with respect to the crack growth rate:

(1) The crack growth rate in Sample BY is remarkably higher than that of Sample AZ. Particularly, the crack growth rate between the effective crack length of 380 μm and 520 μm is 0.23 μm/cycle for Sample BY compared with 0.1 μm/cycle for Sample AZ.

(2) The crack growth rate of Sample BY sees an obvious fluctuation when the crack traverses the microstructural obstructions with a rapid drop from 0.31 to 0.14 μm/cycle between cycle 2100 and 2400, in which three events (e_1, e_2 and e_3) occur including the short crack approaching, passing through, and leaving the obstructions as shown in Fig. 5-3 (d).

These two features well represent the microstructural sensitivity of short crack growth corresponding to bulk changes (texture) and local microstructure changes (grain orientation, boundary or triple junction). This chapter has the aim to quantify the driving force for short crack growth which is responsible for this behaviour and which captures

these two main features giving further understanding on the mechanisms of short crack growth.

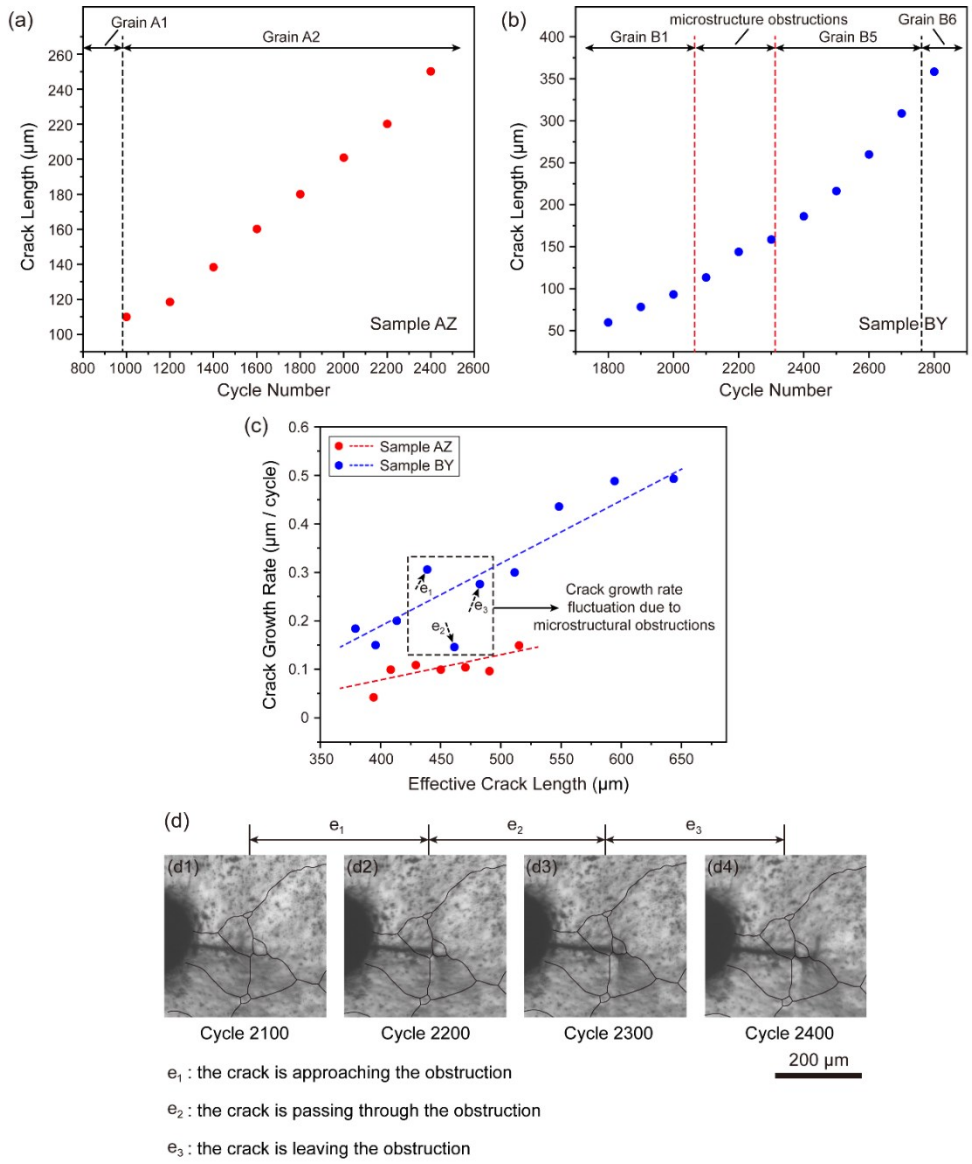


Fig. 5-3. Crack length versus cycle number in Sample AZ (a) and BY (b); (c) crack growth rate versus effective crack length in Samples AZ (red) and BY (blue); (d) optical microscope (OM) images with grain boundaries overlapping showing the events when the short crack encounters microstructural obstructions from cycle 2100 to 2400 in Sample BY.

5.5. Strain and stress distributions in the crack-tip area

5.5.1. Strain distribution

Fig. 5-4 and Fig. 5-5 show the total strain component distributions at peak load in the area near the crack-tip of Sample AZ at cycle 2200 and Sample BY at cycle 2400 corresponding to the effective crack length of about 500 μm. The strains were calculated from DIC measurements. The pictures of cracks have been included to make clear the location of the crack-tips with respect to the DIC-measured total strains, where the crack-tip is represented by a white dot. The expected predominant strain (xx) is seen to develop on both sides of the crack in a 'butterfly' shape (particularly for sample AZ) as the remote loading direction is aligned with the x-direction for both samples, and leaving the plastic wakes along both sides behind the crack-tip. However, the distribution of the total strain (xx) in Sample AZ near the crack-tip shows wider 'wings' than that in Sample BY. Total strain (yy) with negative value at the crack-tip in Sample AZ is considered to accommodate the extension strain along the x-direction. On the other hand, the total strain (xx) and strain (yy) are both positive at the crack-tip in Sample BY with very strong total shear strain at the crack-tip. The differing strain distribution is attributed to the slip activation near the crack tip with only prismatic slip activated in Sample AZ while prismatic slip, basal slip and pyramidal slip are all activated in Sample BY.

The SEM images showing slip activation in the crack-tip area of Sample AZ and BY are unfortunately absent because of the difficulty in these experiments in which the

electropolishing process for EBSD detection after DIC measurement has destroyed the slip traces on the sample surface. However, it is reasonable to refer to other equivalent observation with similar crack path and local microstructures near the crack-tip in blocky alpha Zircaloy-4 samples. Fig. 5-6 shows the SEM images of the slip traces with grain boundaries near the crack-tip in Sample PZ which is similar to the case in Sample AZ, where the crack-tip in Sample PZ is located in a large grain (Grain P1) with the c-axis aligned with the Z-direction. The grain orientation of Grain P1 is represented by a hexagon in Fig. 5-6 (c). Prismatic slip bands are observed with the traces marked in yellow and green dashed lines aligning with the intersecting lines between prismatic planes and surface plane. The slip traces shown in Fig. 5-7 refers to the cases similar to Sample BY with the c-axes aligned with the Y-direction. The grain orientations of Grain QY1 and QY2 are represented by hexagons. The prismatic slip, basal slip and <c+a> pyramidal slip system are activated near the crack-tip in Sample QY1 as shown in Fig. 5-7 (b). The slip traces of prism, basal and <c+a> pyramidal are marked with white, red and yellow dashed lines respectively. It is interesting that the shape of the curve slip traces is very similar with the strain (xx) band. Fig. 5-7 (c) and (d) show another case (Sample QY2) similar with Sample BY with a larger field of view than in Fig. 5-7 (b) near the crack-tip. The <c+a> pyramidal slip is observed to dominate the slip activation in the crack-tip area with more prismatic slip far from the crack-tip. Thus, it is argued that the <c+a> pyramidal slip plays the key role in the short crack growth in Sample BY and the similar cases.

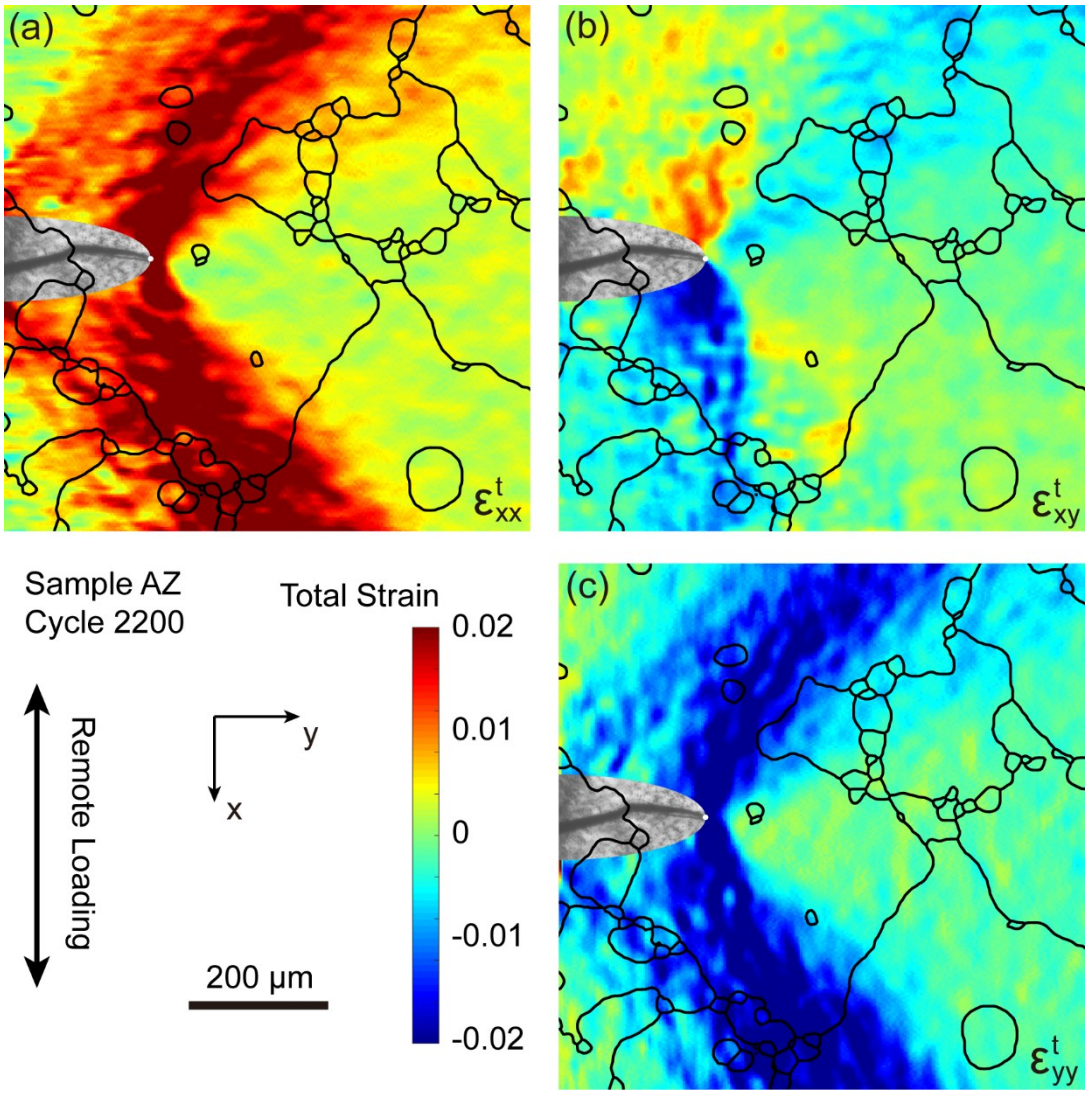


Fig. 5-4. Total strain distribution of Sample AZ in the area near the crack-tip at cycle 2200 with the effective crack length at around 500 μm: (a) total strain (xx); (b) total strain (xy); (c) total strain (yy).

It is noted that the strain components related to the z-direction, which are not accessible in the 2D DIC measurement, ought to be considerable near the crack-tip in Sample BY. It is reasonable for the prismatic slip, basal slip and pyramidal slip to achieve out-of-plane strains to accommodate the dominant extension strain (xx). However, it is

assumed that the out-of-plane strains would not directly contribute to the surface short crack growth (type I and type II). Thus, only in-plane strains are considered in this study.

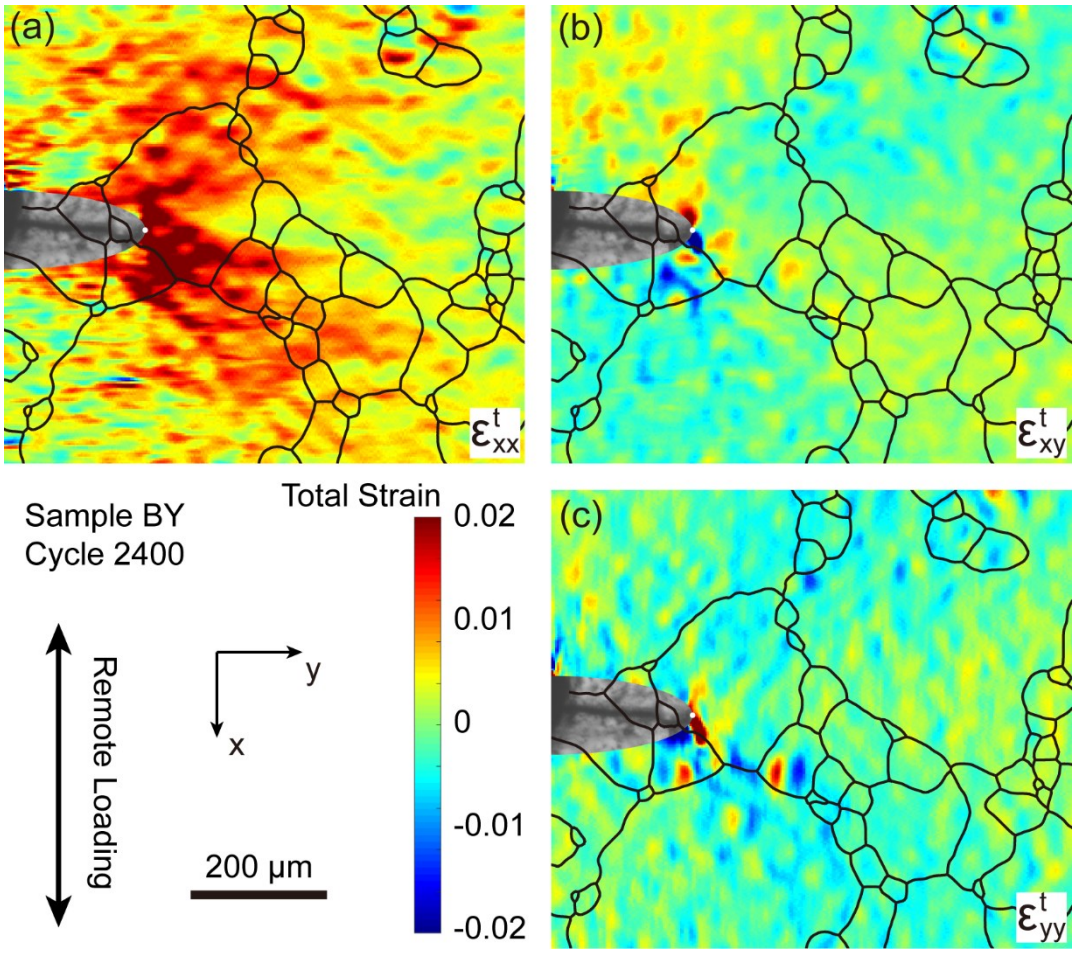


Fig. 5-5. Total strain distribution of Sample BY in the area near the crack-tip at cycle 2400 with the effective crack length at around 500 μm: (a) total strain (xx); (b) total strain (xy); (c) total strain (yy).

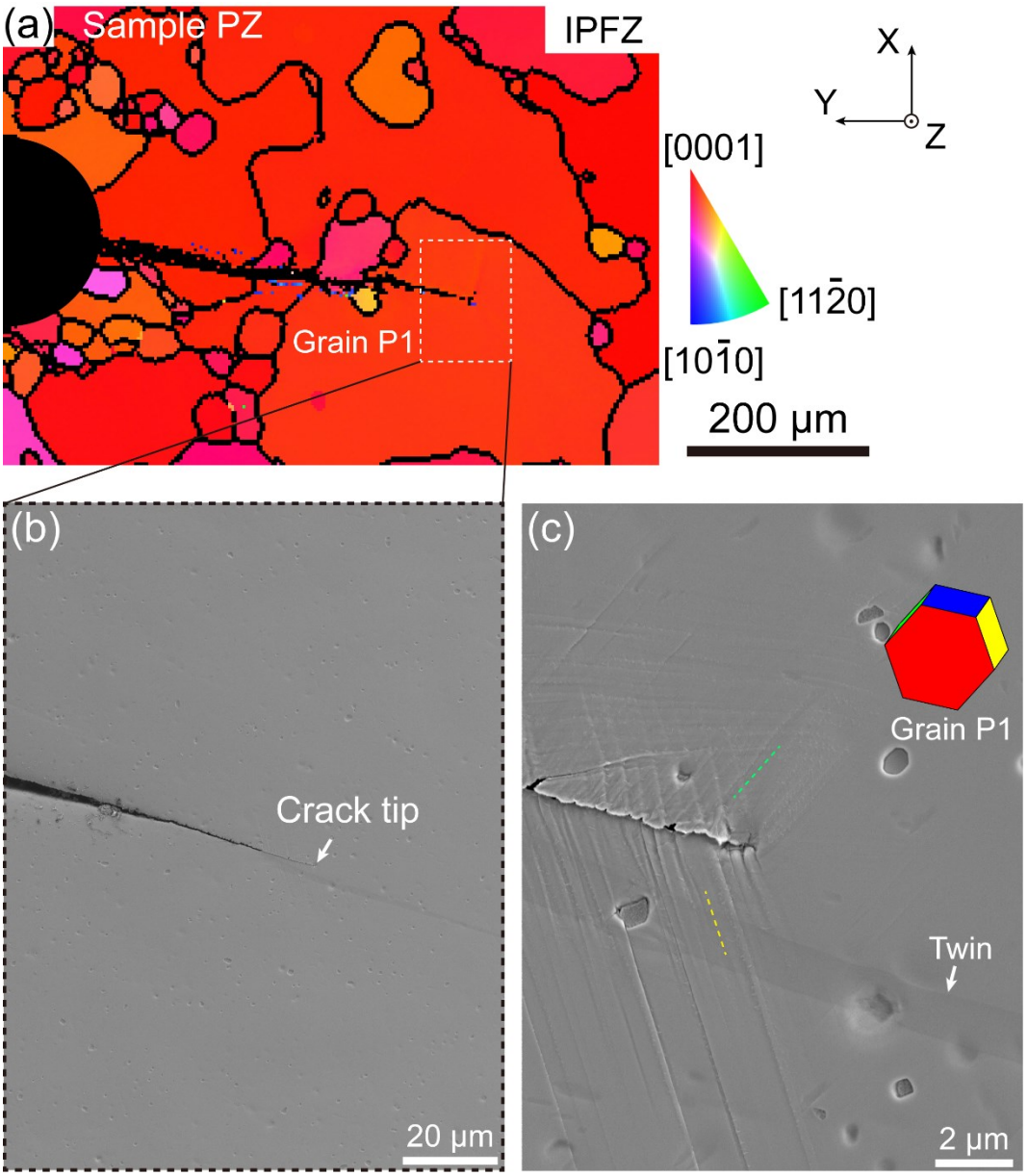


Fig. 5-6. (a) IPFZ of Sample PZ; (b) SEM image showing the area in the dashed rectangular; (c) enlarged SEM images of (b) showing the slip traces near the crack-tip.

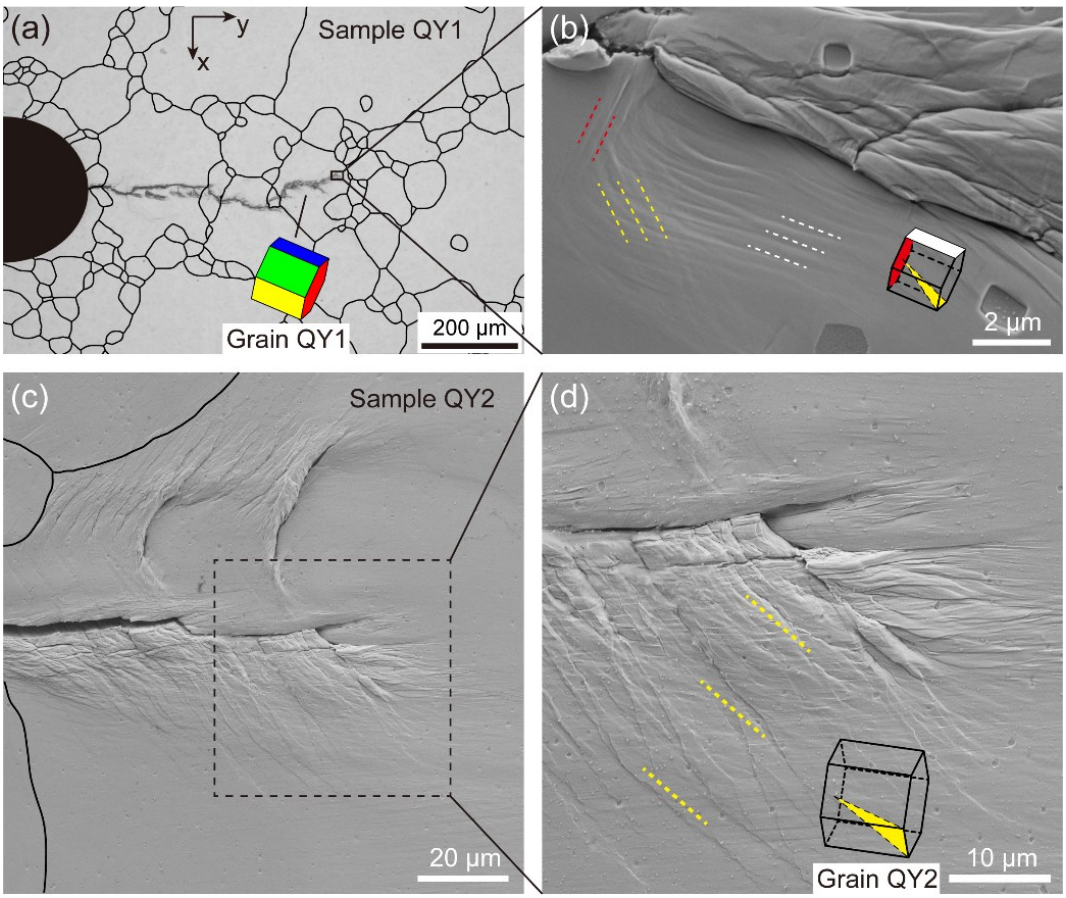


Fig. 5-7. (a) OM image of Sample QY1 showing a crack path; (b) enlarged SEM image of (a) at the crack-tip; (c) SEM image of Sample QY2; (d) enlarged SEM image of (c) at the crack-tip.

The in-situ DIC gives the possibility to measure the strain in the unloaded condition and at peak load in a full cycle as introduced in Section 4.5.3. The strain obtained in the unloaded condition is approximately equal to the plastic strain when the residual elastic strain is ignored. Meanwhile the strain at the peak load is total strain $\boldsymbol{\varepsilon^t}$ with the sum of elastic strain $\boldsymbol{\varepsilon^e}$ and plastic strain $\boldsymbol{\varepsilon^p}$. Thus the elastic strain can be extracted from the difference between total strain and plastic strain:

$$\boldsymbol{\varepsilon^e = \varepsilon^t - \varepsilon^p.} \qquad (5\text{-}5)$$

Fig. 5-8 and Fig. 5-9 show the distributions of elastic strain components (ε_{xx}^{e}, ε_{xy}^{e} and ε_{yy}^{e}) in the crack-tip area of Sample AZ and BY with grain boundaries indicated. In Sample AZ, the dominant ε_{xx}^{e} over 0.02 is concentrated at the crack-tip while ε_{yy}^{e} sees negative value indicating compressive strain in the y-direction. The elastic strain distribution at the crack-tip in Sample BY is different from that in Sample AZ. The ε_{xx}^{e} and ε_{yy}^{e} both have positive value (stretching), and the ε_{xy}^{e} is above 0.02 in Sample BY which is larger than that in Sample AZ.

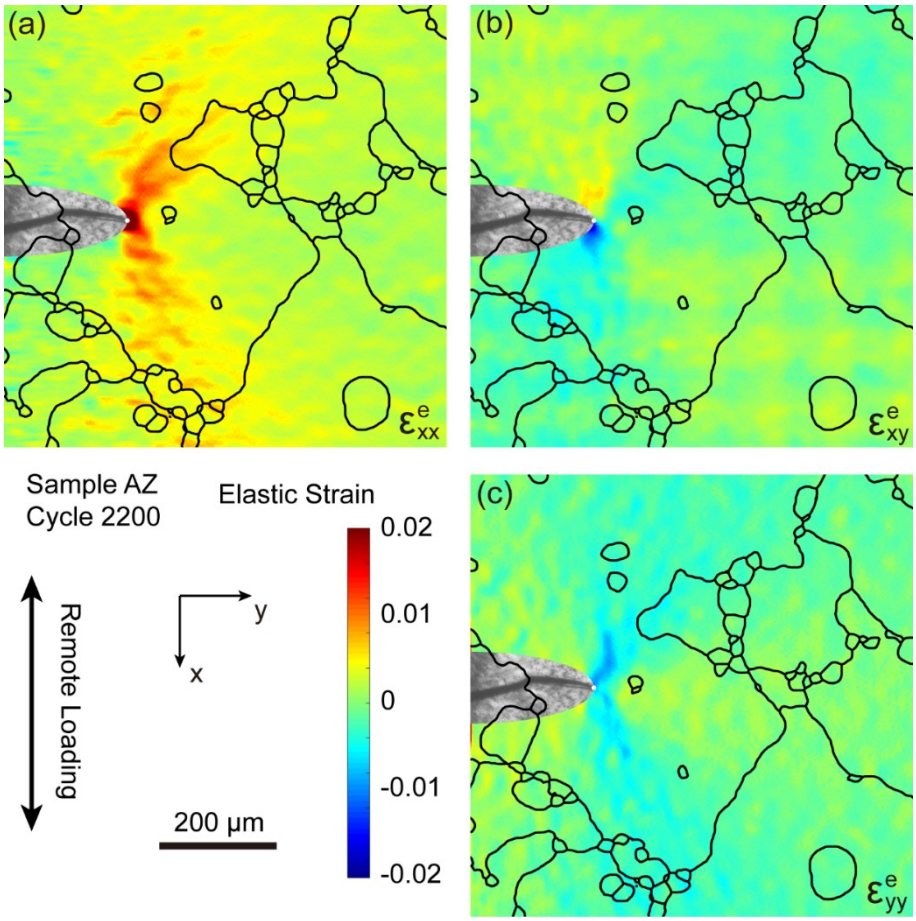


Fig. 5-8. Elastic strain distribution of Sample AZ in the area near the crack-tip at cycle 2200 with the effective crack length at around 500 μm: (a) elastic strain (xx); (b) elastic strain (xy); (c) elastic strain (yy).

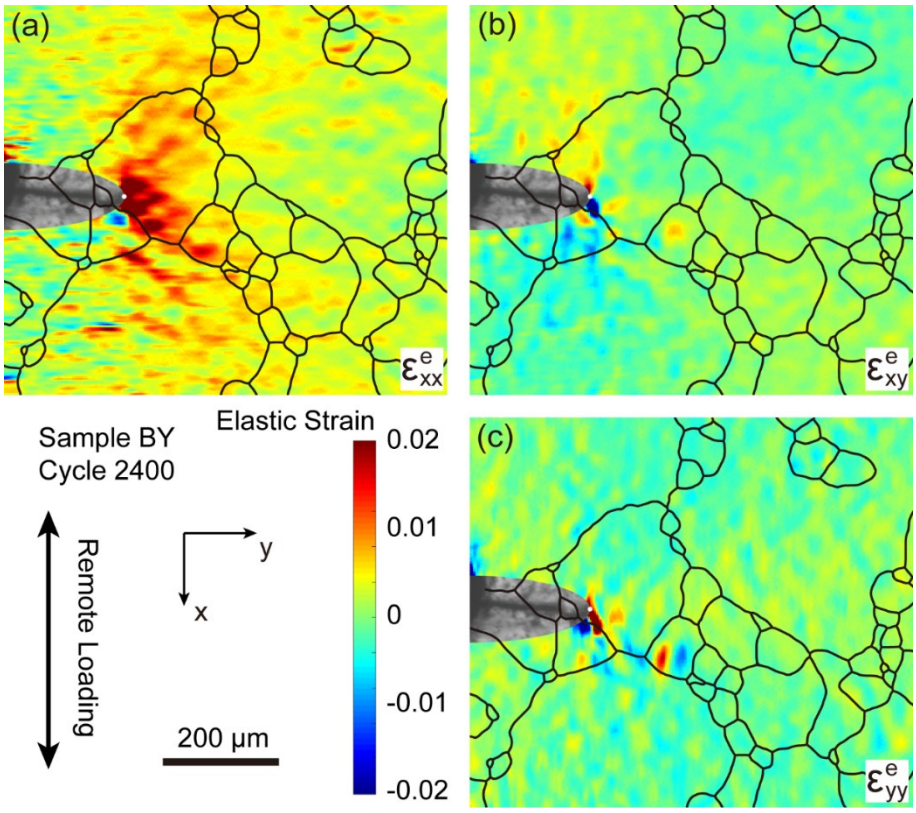


Fig. 5-9. Elastic strain distribution of Sample BY in the area near the crack-tip at cycle 2400 with the effective crack length at around 500 μm: (a) elastic strain (xx); (b) elastic strain (xy); (c) elastic strain (yy).

5.5.2. Stress distribution

The local stress distribution in the crack-tip area can be determined by the experimental method introduced in Chapter 4. As mentioned in the previous section, in-situ DIC measurement offers the possibility to determine the total strain fields at peak load and in the unloaded condition in any one full cycle such that the elastic strain can be estimated from the difference between them. Thus, the local stress can be obtained from Equation (4-11) with the grain orientations detected by EBSD.

Fig. 5-10 and Fig. 5-11 show the stress state with components σ_{xx} σ_{xy} and σ_{yy} at the crack-tip area of Sample AZ at cycle 2200 and Sample BY at cycle 2400 superposed on to the microstructures. In Sample AZ, stress (xx) reaches 2 GPa at the concentrated area around the crack tip and develops to two sides forming 'wing' bands. A significant multiaxial stress state is detected at the crack-tip in Sample AZ as stress (yy) reaches 1 GPa and the shear stress 500 MPa at the crack-tip. Sample BY also sees multiaxial stress state at the crack-tip with higher stress (yy) and stress (xy) than in Sample AZ. Similar with the elastic strain (xx) distributions, the stress (xx) distributions of Sample AZ and BY show significant differences: the stress localisation bands in Sample AZ developing wider to two sides than those in Sample BY. The differing stress responses at the crack-tip with nearly the same effective crack length between Sample AZ and BY is attributed to the crystalline anisotropy especially the crystal orientation which determines the rotation of stiffness matrix.

Stress concentrations are seen with finite stress values (over 2 GPa) measured at the crack-tip in both samples. It is worthy to note that the resolution of DIC measurement is approximately 3 μm as introduced in the method section and hence the resolution of stress fields has the same spacing resolution. Thus the experimental measurement can only approach the crack-tip as close as possible but not reach the crack-tip point with assumed stress singularity. Such high stress values are not likely achieved only by strain hardening. The slip system hardening has been taken to be of the form (G.I. Taylor, 1934; Kocks and Mecking, 2003)

$$\tau = \tau_0 + \alpha G b \sqrt{\rho_{SSD} + \rho_{GND}}, \qquad (5\text{-}6)$$

where τ is the shear stress on a given slip plane, τ_0 the critical resolved shear stress (CRSS) of specific slip system, *G* the shear modulus, *b* the magnitude of the Burgers vector, α a constant which is dependent on temperature, and ρ_{SSD} and ρ_{GND} statistically stored and geometrical necessary dislocation densities respectively. It is argued that the dislocation density, and especially the GND density, ρ_{GND} plays a significant role on the hardening, which can be termed as GND hardening. GNDs contribute to work hardening by acting as individual obstacles to slip and creating a long-range back-stress (Ashby, 1970). For plane stress conditions, yielding occurs when the Von Mises stress reaches the yield stress ($\sigma_{Von} = \sigma_{YS}$), where σ_{YS} is the uniaxial yield strength of Zircaloy-4 at around 460 MPa. In both Sample AZ and Sample BY the stress (xx) values at the crack-tip reach 2 GPa (the Von Mises stress must be higher) which apparently results in material yielding. To achieve such high stress, the GND hardening must be considerable. The GND density in the crack-tip area will be discussed in the later section. Besides the slip hardening, twining in the crack-tip area may also contribute to high stress to accommodate large-scale yielding.

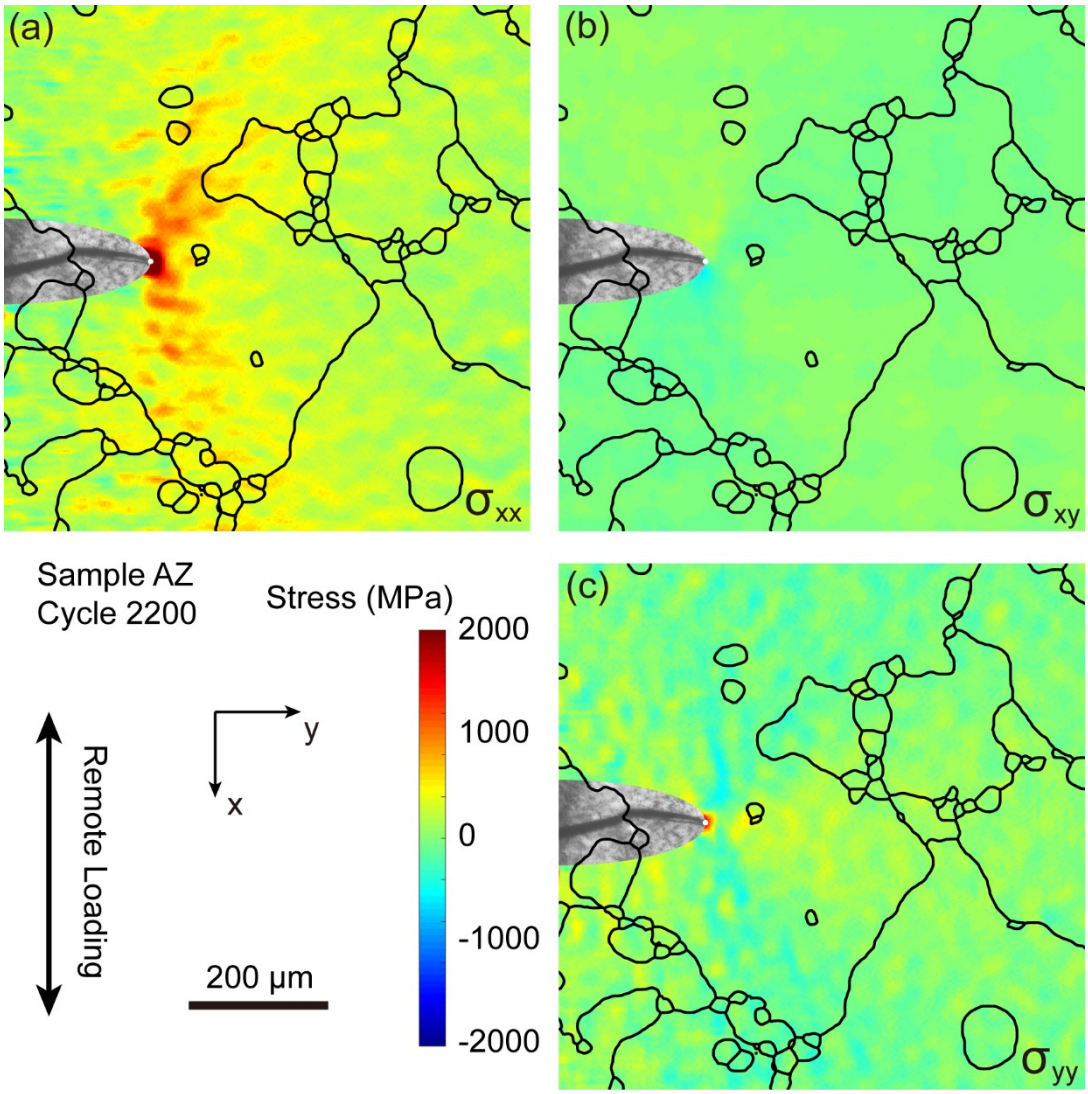


Fig. 5-10. Stress distribution of Sample AZ in the area near the crack-tip at cycle 2200 with the effective crack length at around 500 μm: (a) stress (xx); (b) stress (xy); (c) stress (yy).

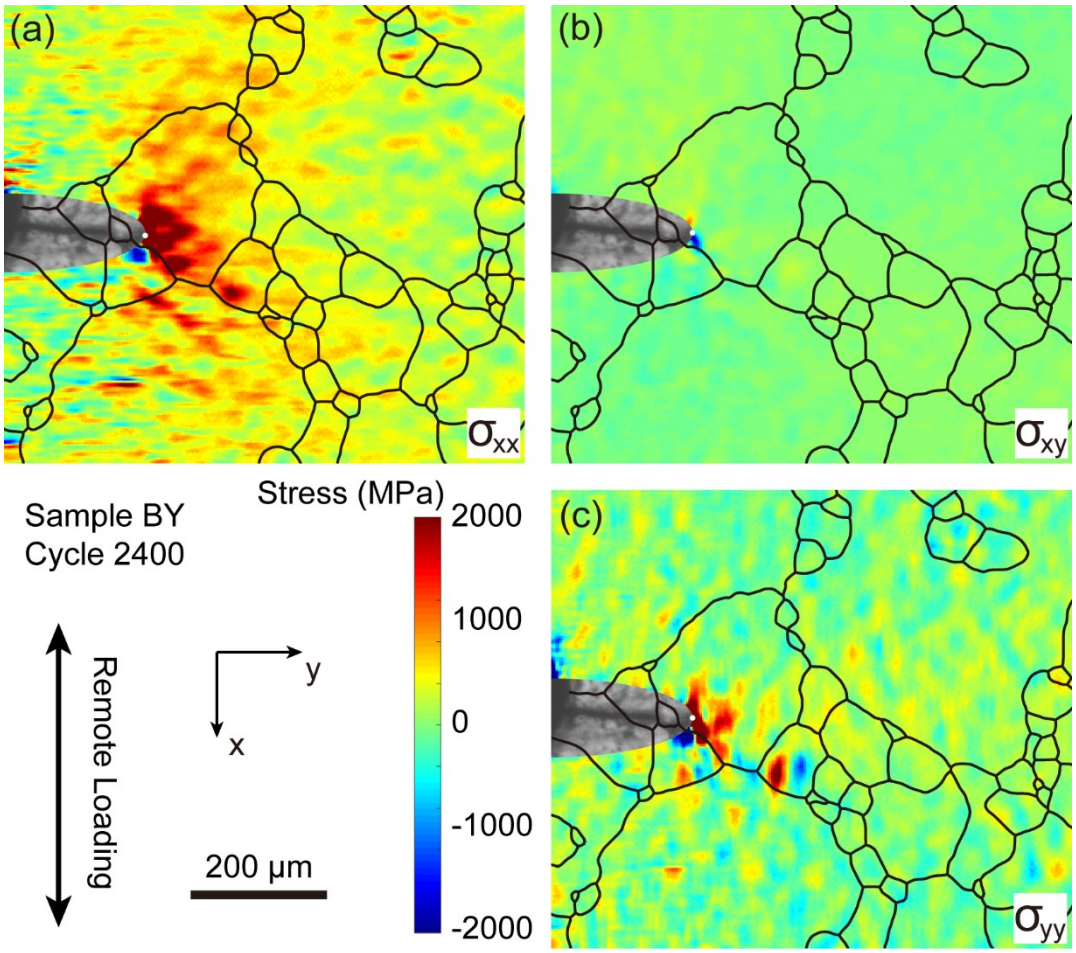


Fig. 5-11. Stress distribution of Sample BY in the area near the crack-tip at cycle 2400 with the effective crack length at around 500 μm: (a) stress (xx); (b) stress (xy); (c) stress (yy).

5.6. Strain and stress evolution in the crack-tip area during crack growth

5.6.1. Strain evolution in the crack-tip area

Effective strains are calculated to analyse the strain evolution in the short crack growth. As the strain components in the z-direction are not accessible with 2D DIC measurement, the in-plane effective strain is considered here for simplification, given by

$$\varepsilon_{eff} = \sqrt{\frac{2}{3}(\varepsilon_{xx}{}^2 + \varepsilon_{yy}{}^2 + 2\varepsilon_{xy}{}^2)} \qquad (5\text{-}7)$$

A rectangular region of interest (ROI) ahead of the crack tip (as it grows) of approximately 150 μm × 300 μm is chosen within which all the micromechanical quantities of interest are determined. This ROI is considered to cover the plastic zone of the crack growth mostly. The evolutions of effective strain in the ROI in the unloaded condition (effective plastic strain, ε_{eff}^{p}) and at peak load (effective total strain, ε_{eff}^{t}) are shown in Fig. 5-12, Fig. 5-13, Fig. 5-14 and Fig. 5-15 for samples AZ and BY. The black arrows in every sub-figure represent the locations of crack-tips at specific cycles. In Sample AZ, the strain localisation remains a consistent distribution at both sides of the crack during the crack growth. On the other hand, the distribution in Sample BY is more heterogeneous than that in Sample AZ. Sample BY shows an obvious asymmetric distribution of effective strain at the early stage (from cycle 1800 to 2100) with a higher effective strain localised to the lower side of the crack, however, more effective strain develops at the upper side after cycle 2200. It is probably because more pyramidal slip is activated after cycle 2200 at upper side with the local resolved shear stress reaches CRSS of pyramidal slip system.

Fig. 5-16 shows the average effective total strain and plastic strain in the ROI versus the effective crack length in Samples AZ and BY. All the strains increase with the crack growing except some fluctuations of effective plastic strain between 400 to 500 μm of the effective crack length in Sample BY, which is likely attributed to the obstruction by local microstructures. It is interesting that the evolutions of the effective total and plastic

strains in Sample AZ are much larger than that in Sample BY. When the effective crack length less than 450 μm the effective plastic strain of Sample AZ is lower than that in Sample BY, however, it exceeds the latter and increases to around 0.02. The evolution of the effective total strain sees similar trend with the exceeding point at around 480 μm of the effective crack length. These differing strain evolutions are attributed to plastic anisotropy mainly achieved by slip. The short crack in Sample AZ is growing inside a single crystal (Grain A2) with only prismatic slip activated near the crack-tip, while multiple slip (prismatic slip, basal slip and pyramidal slip) exist and prefer to localise close to the crack-tip in Sample BY. This is the reason why the strain (xx) localisation area in Sample BY is smaller than that in Sample AZ as shown in Fig. 5-4 and Fig. 5-5. In addition, as the crack grows in Sample AZ the prismatic slip develops more with the plastic zone expanding and moving forward without blockage within Grain A2 while the slip, especially the <c+a> pyramidal, is more difficult to be activated far from the crack-tip in Sample BY due to not enough resolved shear stress magnitude.

It is interesting that a dramatic increase of effective total strain or plastic strain is seen in Sample AZ from cycle 2200 to cycle 2400 corresponding to the effective crack length increasing from around 500 to 525 μm. Two possible explanations are proposed: (1) the crack growth is stepping into the Stage II with the local microstructures showing less influence; (2) this might result from the transformation of deformation mechanism that the effect of twinning becomes significant on the deformation near the crack-tip. Fig. 5-17 shows the SEM and EBSD images in the crack-tip area at cycle 2400 of Sample AZ. Tensile type twinning is found to activate close to the crack tip but only appear in

the right side of the dashed line. The orientation of the twins and parent grain are represented by hexagons as shown in Fig. 5-17 (b). It is argued that twinning is not likely to occur before the effective crack length reaches 500 μm in Sample AZ. Hence the prismatic slip is believed to dominate the deformation near the crack-tip before the short crack grows to 500 μm (effective crack length) while twinning gives rise to the plasticity coupling with prismatic slip after that. However, we herein focus on the contribution of prismatic slip while the effect of twinning on short crack growth needs further study in the future work.

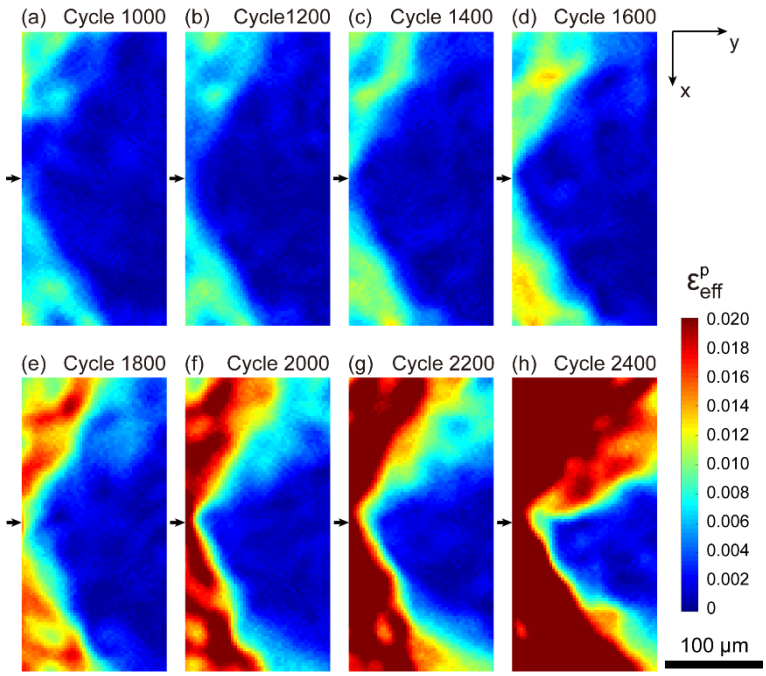


Fig. 5-12. Evolution of effective plastic strain distribution of Sample AZ in the ROI in the unloaded condition from cycle 1000 to 2400 with the effective crack length from 380 to 520 μm (The black arrow marks the crack tip).

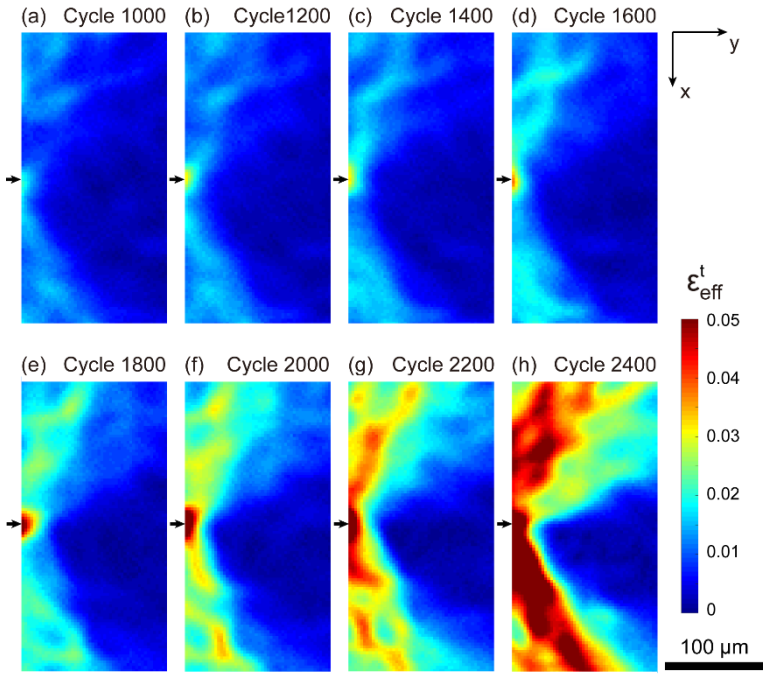


Fig. 5-13. Evolution of effective total strain distribution of Sample AZ in the ROI at peak load from cycle 1000 to 2400 with the effective crack length from 380 to 520 μm (The black arrow marks the crack tip).

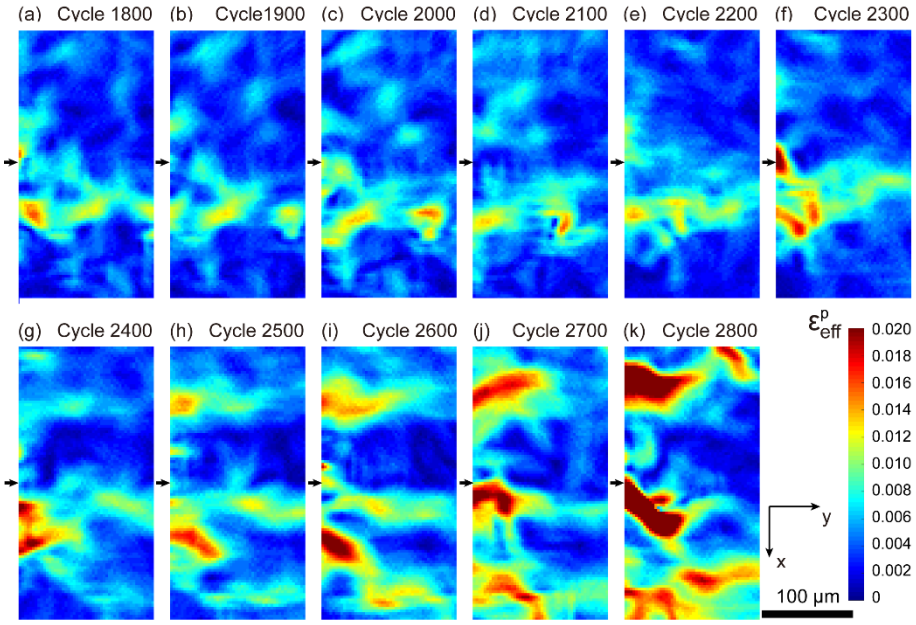


Fig. 5-14. Evolution of effective plastic strain distribution of Sample BY in the ROI in the unloaded condition from cycle 1800 to 2800 with the effective crack length from 360 to 640 μm (The black arrow marks the crack tip).

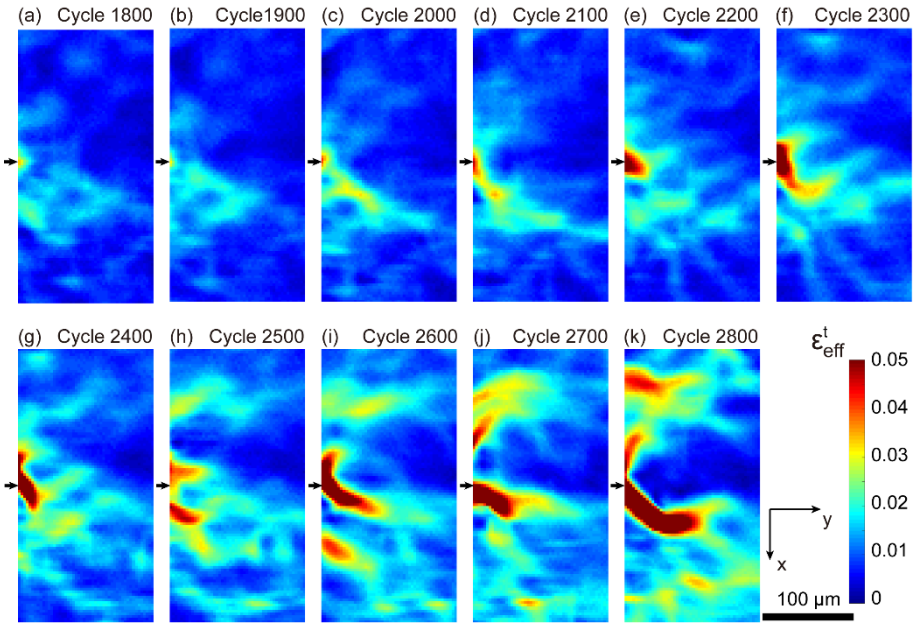


Fig. 5-15. Evolution of effective total strain distribution of Sample BY in the ROI at peak load from cycle 1800 to 2800 with the effective crack length from 360 to 640 μm (The black arrow marks the crack tip).

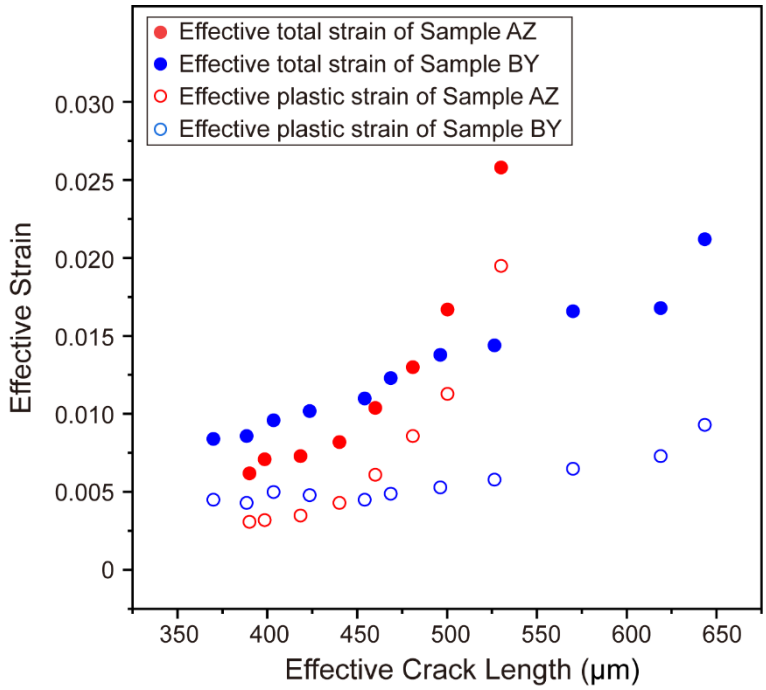


Fig. 5-16. Average effective strains of Sample AZ and BY in the crack-tip ROI area (150 μm × 300 μm) versus effective crack length.

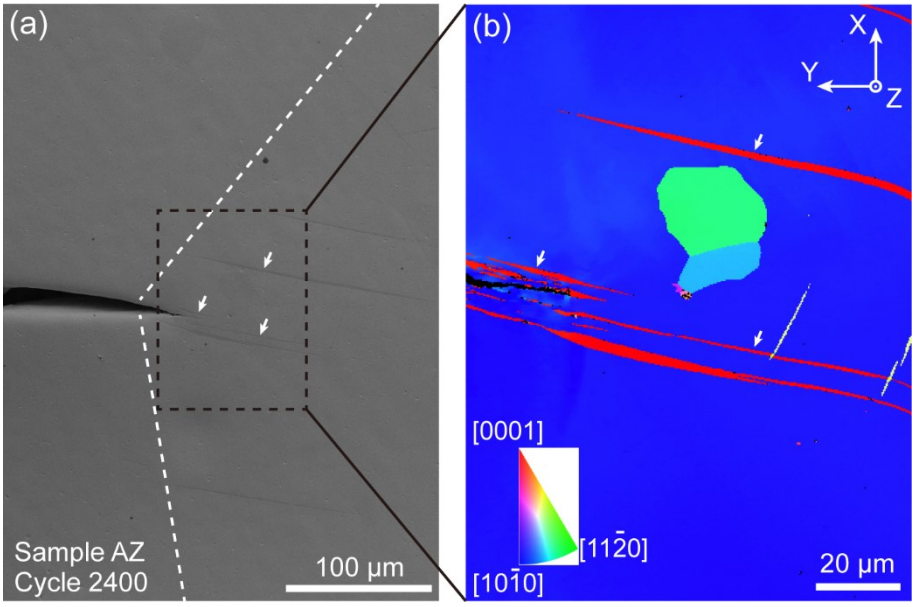


Fig. 5-17. (a) SEM image showing the crack-tip of Sample AZ at cycle 2400; (b) IPFX image showing the twinning at the crack-tip in an enlarged area in (a).

5.6.2. Stress evolution in the crack-tip area

The stress tensor is the function of elastic strain tensor and rotated stiffness matrix such that it is a mechanical response of strain coupling with the nature of crystallographic orientations. The Von Mises stresses for plane stress are calculated by

$$\sigma_{VM} = \sqrt{{\sigma_{xx}}^2 + {\sigma_{yy}}^2 - \sigma_{xx}\sigma_{yy} + 3{\sigma_{xy}}^2} \qquad (5\text{-}8)$$

Fig. 5-18 and Fig. 5-19 show the evolution of Von Mises stress distributions in the ROI of Sample AZ and BY. Stress concentrations are seen with finite stress values measured at the crack-tip in both samples. The distributions of Von Mises stresses in Sample AZ and BY show significant differences with the stress bands develops wider to two sides in Sample AZ but more converged in Sample BY.

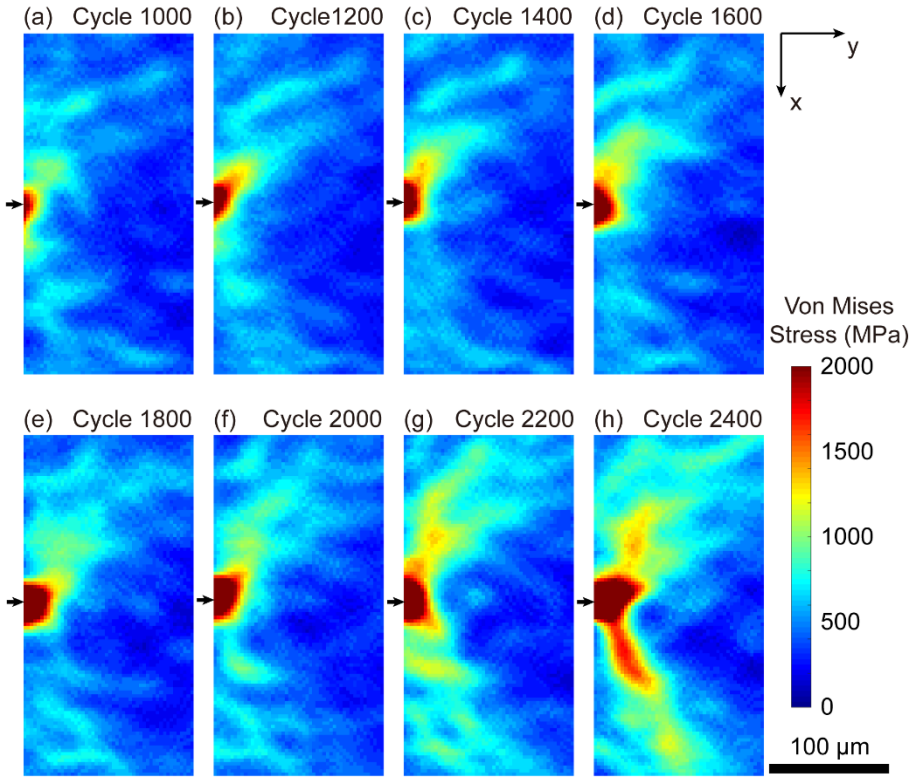


Fig. 5-18. Evolution of Von Mises stress distribution of Sample AZ in the crack-tip area at peak load from cycle 1000 to 2400 (The black arrow marks the crack tip)

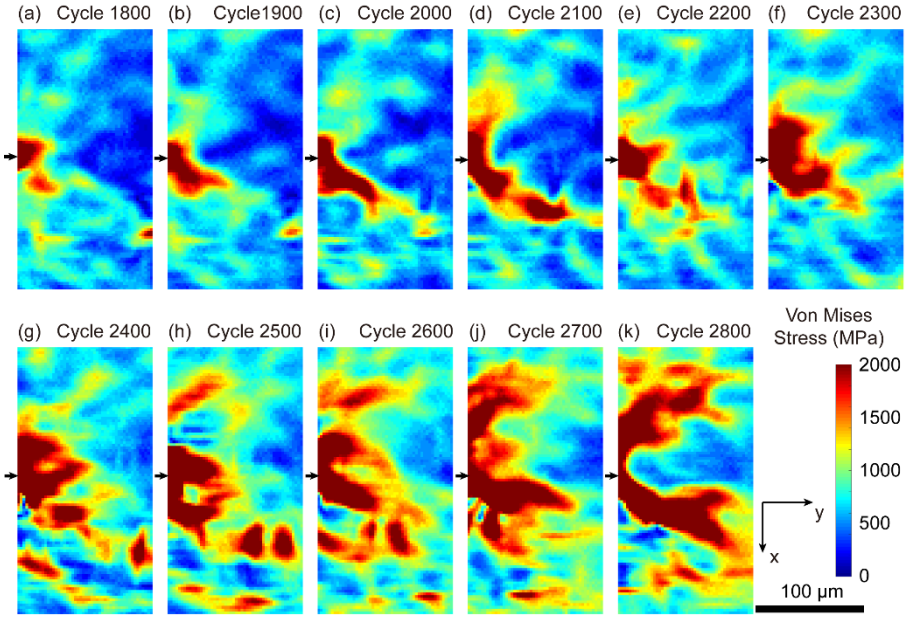


Fig. 5-19. Evolution of Von Mises stress distribution of Sample BY in the crack-tip area at peak load from cycle 1800 to 2800 (The black arrow marks the crack tip).

Fig. 5-20 shows the average Von Mises stress in the ROI versus the effective crack length in Sample AZ and BY respectively. It is not supervised to see the average Von Mises stress gradually increasing with the crack growth. The average Von Mises stress of Sample BY is remarkably higher than that of Sample AZ. This difference is attributed to crystal anisotropy with both elasticity and plasticity. Although zirconium HCP crystal is isotropic in the basal plane with $C_{11} = C_{22} = 142$ GPa, the stress response in elasticity of Sample BY is higher than that of Sample AZ under plane stress condition with zero stress components in the z-direction. However, the plasticity is argued to dominate the stress distinction between two samples since the elasticity anisotropy is not enough to achieve such high difference on stress. From Equation (5-8) it is known that the flow stress is dependent on CRSS and dislocation density in one specific slip system. The prismatic slip is activated in Sample AZ while multiple slip including prismatic, basal and <c+a> pyramidal slips are in Sample BY according to the SEM characterisation results presented earlier. In addition, the <c+a> pyramidal slip is argued to dominate slip activation associated to the short crack growth in Sample BY. The CRSS, τ_0 of <c+a> pyramidal slip (532 ± 58 MPa) is a factor of 3.5 times higher than that of prismatic slip (153 ± 30 MPa) in zirconium (Gong et al., 2015). Thus the <c+a> pyramidal slip system in Sample BY needs higher shear stress to activate than the prismatic slip system in Sample AZ. The GND density is considered to be another important factor for the hardening at the crack-tip. The GND density in the crack-tip area will be discussed in the next section. Besides the slip hardening, twinning in the crack-tip area can also contribute to high stress to accommodate large-scale yielding.

The retardation of short crack growth occurs between 425 to 500 μm of the effective crack length in Sample BY as introduced in Fig. 5-3. During this period the Von Mises stress at peak load rises gradually without showing a drop in value although it has fluctuation in increase rate as shown in Fig. 5-20. Thus, the average Von Mises stress evolution to some extent captures the feature that the short crack growth rate of Sample BY is remarkably higher than that of Sample AZ but does not intuitively present a microstructural obstruction effect on short crack growth rate, especially in Sample BY.

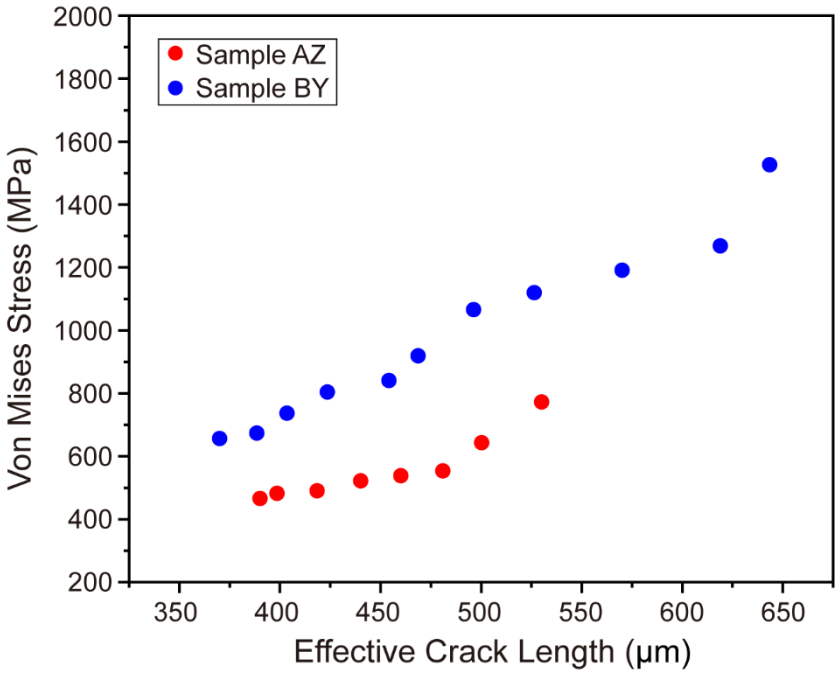


Fig. 5-20. Average Von Mises stresses at peak load in the ROI versus effective crack length of Samples AZ and BY.

5.7. GND density

As a potential contributor to work hardening and nucleation of fatigue cracks, GND density measured by EBSD has been reported in quite a few former works (Jiang et al.,

2013; Ruggles and Fullwood, 2013). However, experimental measurement of GND density in the crack-tip area is rarely reported. Wilkinson et al (Wilkinson et al., 2006) developed a method to calculate the GND density from lattice curvatures by High-resolution EBSD giving rise to the determination of plastic zone at the crack tip. Erinosho and Dunne (Erinosho and Dunne, 2016) studied the contribution from GNDs to lattice strains at a crack-tip by using a 2D CPFE modelling. During the cyclic loading on an edge cracked plate, the elastic strain is largely recovered on unloading, therefore the lattice distortion in the unloaded condition is dominated by GND development. The GND density, which is derived from plastic strain gradient, is closely tied with the crystallographic slip activation.

A methodology has been adopted to estimate the GND density in the crack-tip area from experimental plastic strain field (Xu et al., 2021). In this study, the two-dimensional strain field in the unloaded condition can be considered as the purely plastic component with the elastic part fully relaxed. Since the contributions of out-of-plane strains to surface crack growth are not considered as mentioned above the plastic strain gives

$$\boldsymbol{\varepsilon^{p}} = \boldsymbol{\varepsilon^{Unload}} = \left[\varepsilon_{xx}^{p} \quad \varepsilon_{yy}^{p} \quad \varepsilon_{xy}^{p}\right]^{\boldsymbol{T}}. \qquad (5\text{-}9)$$

Geometrically necessary dislocation (GND) carries the lattice curvature (Arsenlis and Parks, 1999) when material deforms inelastically and heterogeneously, and the GND density measures the intensity of the plastic deformation gradient. Pioneering studies including (Asaro, 1983; Ashby, 1970; Fleck et al., 1994; Fleck and Hutchinson, 1997)

provides a one-dimensional estimation of the GND density along a single slip plane, which is given by:

$$\rho_{GND} = \frac{1}{b}\frac{\partial \gamma}{\partial s} \qquad (5\text{-}10)$$

where b is the Burgers vector of the slip system, γ the shear strain and s the distance in the slip direction coordinate axis. We herein generalize Equation (5-10) into a two-dimensional case, which gives as follows:

$$\boldsymbol{\rho}_{GND} = \frac{1}{b}(\nabla \times \boldsymbol{\varepsilon^p}) \qquad (5\text{-}11)$$

Or it can be written in the form of index notation as

$$(\boldsymbol{\rho}_{GND})_{ij} = \frac{1}{b}(\boldsymbol{\varepsilon^p})_{i,j} \qquad (5\text{-}12)$$

The details of the numerical gradient algorithm is demonstrated in Appendix C. The explicit form of Equation (5-12) gives as following:

$$\begin{bmatrix} \rho_{11} & \rho_{12} \\ \rho_{21} & \rho_{22} \\ \rho_{31} & \rho_{32} \end{bmatrix} = \frac{1}{b}\begin{bmatrix} \frac{\partial \varepsilon_{xx}^p}{\partial x} & \frac{\partial \varepsilon_{xx}^p}{\partial y} \\ \frac{\partial \varepsilon_{yy}^p}{\partial x} & \frac{\partial \varepsilon_{yy}^p}{\partial y} \\ \frac{\partial \varepsilon_{xy}^p}{\partial x} & \frac{\partial \varepsilon_{xy}^p}{\partial y} \end{bmatrix} \qquad (5\text{-}13)$$

By virtue of minimizing the dislocation energy (Kysar et al., 2010), the scalar of effective GND density is given as the sum of the 2nd order norm of its components (Cheng and Ghosh, 2015):

$$\rho_{GND} = (\sum_{j=1}^{2}\sum_{i=1}^{3}\rho_{ij})^{1/2} \qquad (5\text{-}14)$$

The algorithm for determining the GND density assumes the DIC region covers a single phase, single crystal microstructure, and all slip systems share the same Burgers vector. Especially, The <a> prismatic slip Burgers vector (b = 0.323 nm) is applied for Sample AZ while <c+a> pyramidal slip Burgers vector (b = 0.610 nm) for Sample BY. Detailed microstructure information from EBSD analysis (including crystallographic orientation and grain boundary) would refine the GND density calculation by virtue of incorporating the slip system knowledge. The estimation algorithm proposed herein nonetheless indicatively provides a mechanism-based estimated measurement of the GND density magnitude that originates from the DIC strain analysis.

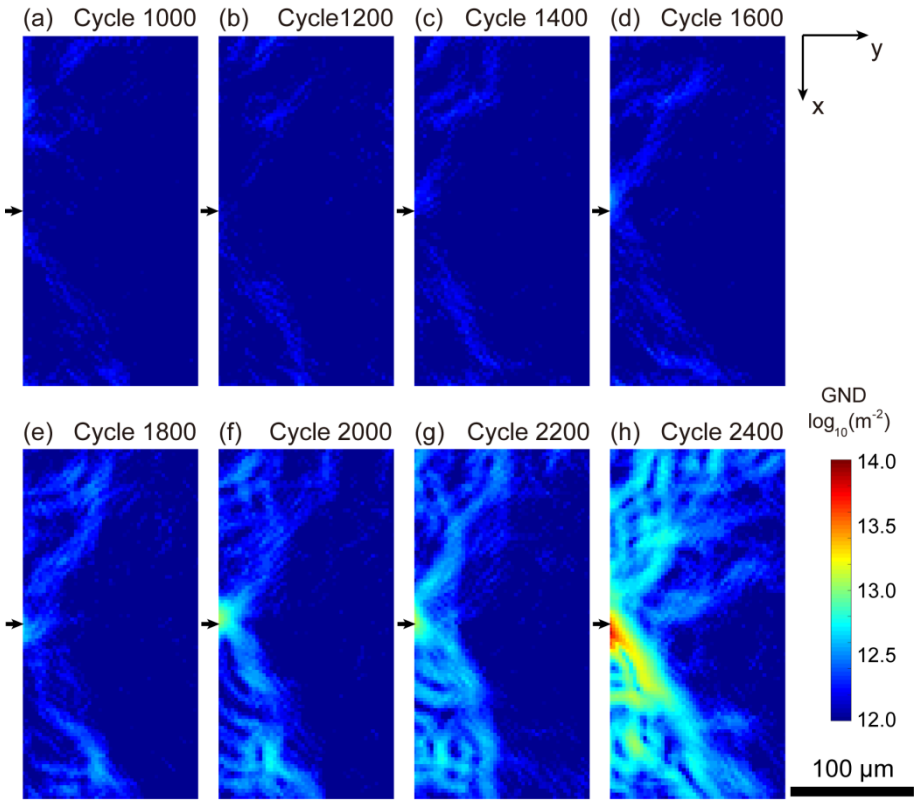


Fig. 5-21. Evolution of GND density of Sample AZ from cycle 1000 to 2400 (The black arrow marks the crack tip).

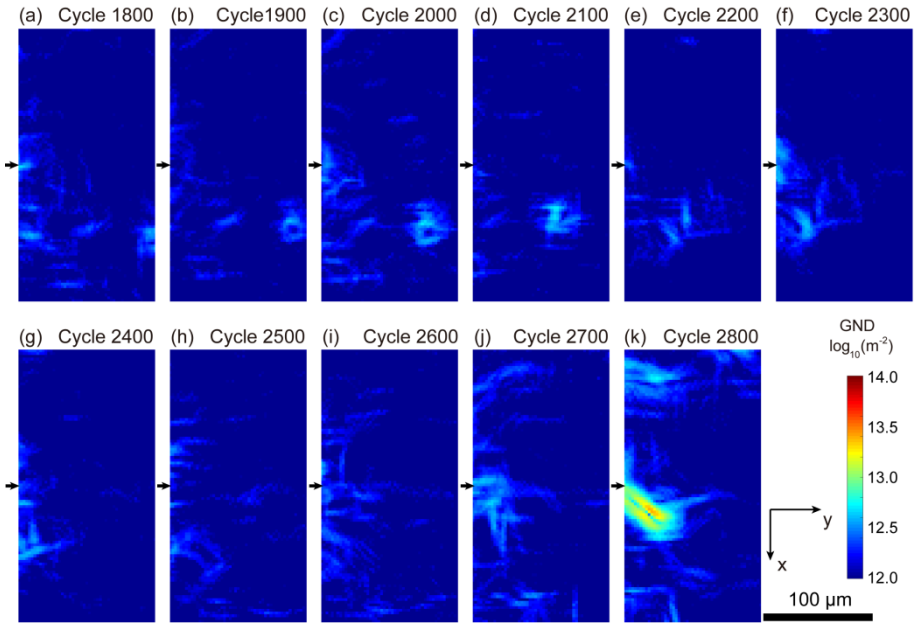


Fig. 5-22. Evolution of GND density of Sample BY from cycle 1800 to 2800 (The black arrow marks the crack tip).

The GND density of Sample AZ and BY in the ROI has been calculated with the method introduced above and the GND density distributions are shown in Fig. 5-21 and Fig. 5-22. In Sample AZ, the GND density concentrates at the crack-tip and develops following the plastic strain localisation bands, which are attributed to the activation of the prismatic slip. However, the GND density in Sample BY appears more dispersed in the ROI with no developing trend or localisation bands except the situation at cycle 3800 where it becomes more localised at the crack tip. The variations of the ROI average GND density corresponding to the effective crack length in the ROI of Sample AZ and BY are shown in Fig. 5-23 (a). The average GND density appears to remain stable in Sample BY before cycle 3600 followed by a slight rise while AZ shows a gradual increase from cycle 1000 to 2400. Before the effective crack length at around 450 μm, the average GND density is very close for two samples. After that the

difference becomes obvious with Sample AZ larger than Sample BY. Fig. 5-23 (b) shows the local GND density evolution of a zoom in area (about 15 × 15 μm^2) ahead of the crack tip. The trend is similar with the average GND density in the ROI.

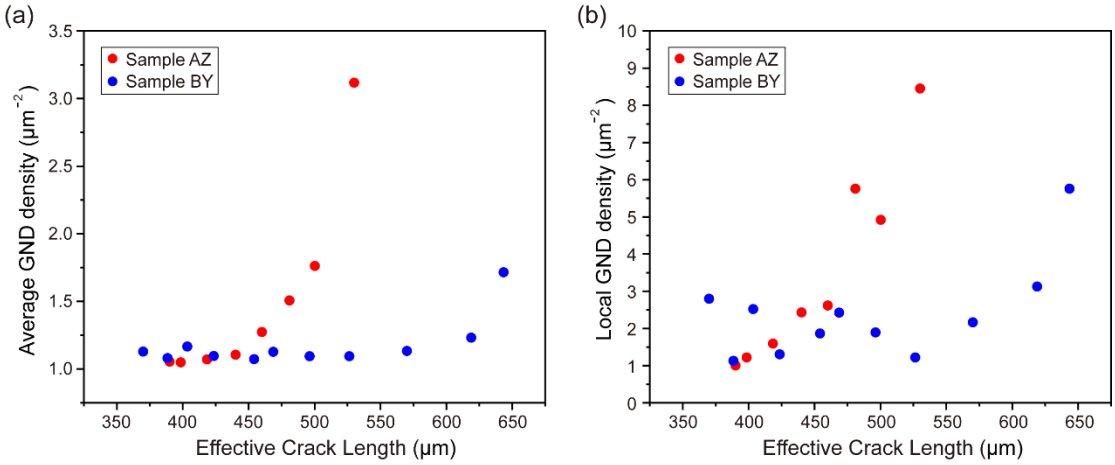


Fig. 5-23. (a) Average GND density in the ROI and (b) local GND density ahead of the crack-tip versus effective crack length.

5.8. Cyclic stored energy density

Mechanical quantities including effective total strain, effective plastic strain, peak stress and GND density at the crack-tip have been addressed at the specific cycles during the short crack growth. However, none of them is found to capture both texture effect and local-microstructure effect of short crack growth in Sample AZ and BY. As reviewed in Section 5.2, a dislocation-based stored energy density criterion has been proposed to be the driving force for short crack growth. The (accumulated) stored energy density G, which is a function of stress, strain and dislocation density, successfully predicts the location of crack initiation and the life to achieve it (Chen et al., 2018; Wan et al., 2014).

Differing from crack nucleation in which the stored energy density is concentrated at a stationary location (hotspot), crack growth is dynamic with the crack-tip moving constantly except for occasional blockage due to microstructural obstacles such as high-angle grain boundary. Hence it is worthy to address the variation of stored energy density per cycle (ie. cyclic stored energy density) rather than the accumulated stored energy density.

Equation (5-4) suggests the cyclic stored energy density is based on the cyclic dissipated energy, which is the area of the cyclic hysteresis loop, but with the important distinction that it depends explicitly on the GND density. Dissipated energy has also been argued to be a potential criterion to describe crack growth (Cojocaru and Karlsson, 2009; Korsunsky et al., 2007). In CPFE modelling work from Korsunsky et al (Korsunsky et al., 2007) the dissipated energy criterion shows good correlation and sensitivity with experimental results. However, so far no experimental determination of energy-based quantities for short crack growth with microstructural sensitivity has yet been carried out. In this section, both cyclic dissipated energy density and stored energy density are calculated and compared for the discussion on the driving force for short crack growth. The numerical method is introduced as follows.

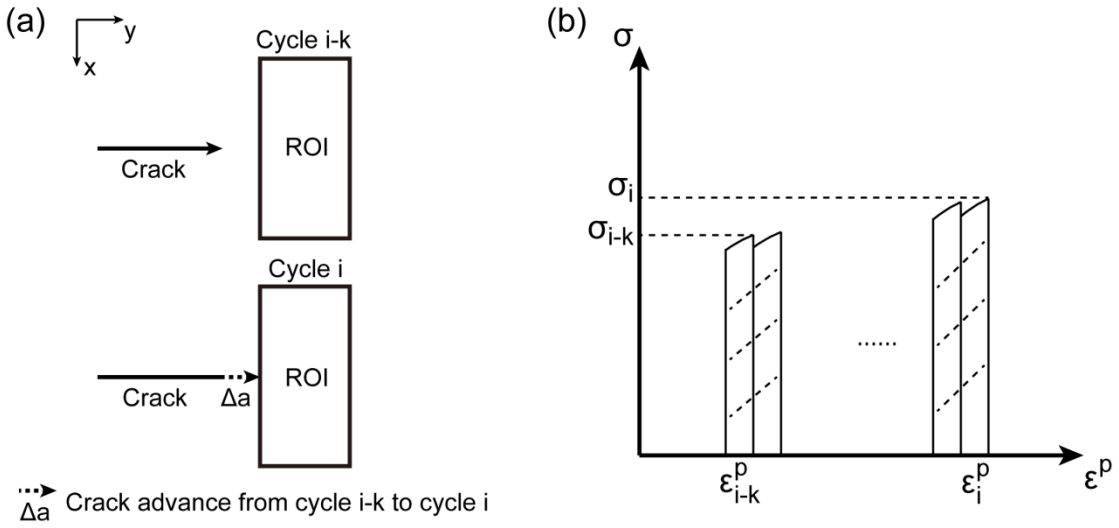


Fig. 5-24. Schematic of cyclic dissipated energy density calculation: (a) the crack growth from cycle i-k to cycle i with a crack advance Δa; (b) the stress at peak load versus accumulated plastic strain in the ROI.

Fig. 5-24 (a) shows the schematics of crack growth from cycle i-k to cycle i with a crack advance Δa represented by a dashed arrow, which means the crack-tip grows ahead with Δa in k cycles. The location of the ROI (marked as rectangular) is next to the crack-tip at cycle i but with the distance Δa from the crack-tip at cycle i-k, which means the calculation is looking at the same area.

For a point (x, y) in the ROI, the plastic strain tensor is obtained from DIC. Therefore, the difference of the accumulated plastic strain during k cycles can be obtained with the plastic strain at cycle i subtracting that at cycle i-k. With the stress tensor at peak load for point (x, y) obtained from the method introduced above, the accumulation of dissipated energy from cycle i-k to cycle i in the ROI, $U(x,y)$ can be integrated as

illustrated in the schematic in Fig. 5-24 (b) showing the peak stress versus accumulated plastic strain:

$$U(x,y) = \int_{i-k}^{i} \boldsymbol{\sigma}(x,y) : d\boldsymbol{\varepsilon^p}(x,y) = \frac{1}{2}(\boldsymbol{\sigma}_i + \boldsymbol{\sigma}_{i-k}) : (\boldsymbol{\varepsilon}_i^p - \boldsymbol{\varepsilon}_{i-k}^p) \qquad (5\text{-}15)$$

The dissipated energy per cycle can be written as,

$$\dot{U}(x,y) = \frac{U(x,y)}{k} \qquad (5\text{-}16)$$

where k is the number of cycles. Actually the expression calculates the dissipated energy at cycle i-k from the area which is shown by the rectangle and is in the same location as that for cycle i (so that the area is not at the crack tip but ahead of it), and then subtracts off that energy which comes from the 'history' (cycle i-k) of deformation as the crack approaches.

With both cyclic dissipated energy and GND density, the cyclic stored energy density can be obtained,

$$\dot{G}(x,y) = \frac{|\xi \dot{U}(x,y)|}{\sqrt{\rho_{SSD}+\rho_{GND}}} \qquad (5\text{-}17)$$

It is argued that $\rho_{GND} \gg \rho_{SSD}$ with large lattice distortion near the crack-tip such that the contribution of ρ_{SSD} to the total dislocation density can be neglected. Hence, the cyclic stored energy density gives

$$\dot{G}(x,y) \approx \frac{|\xi \dot{U}(x,y)|}{\sqrt{\rho_{GND}}} \qquad (5\text{-}18)$$

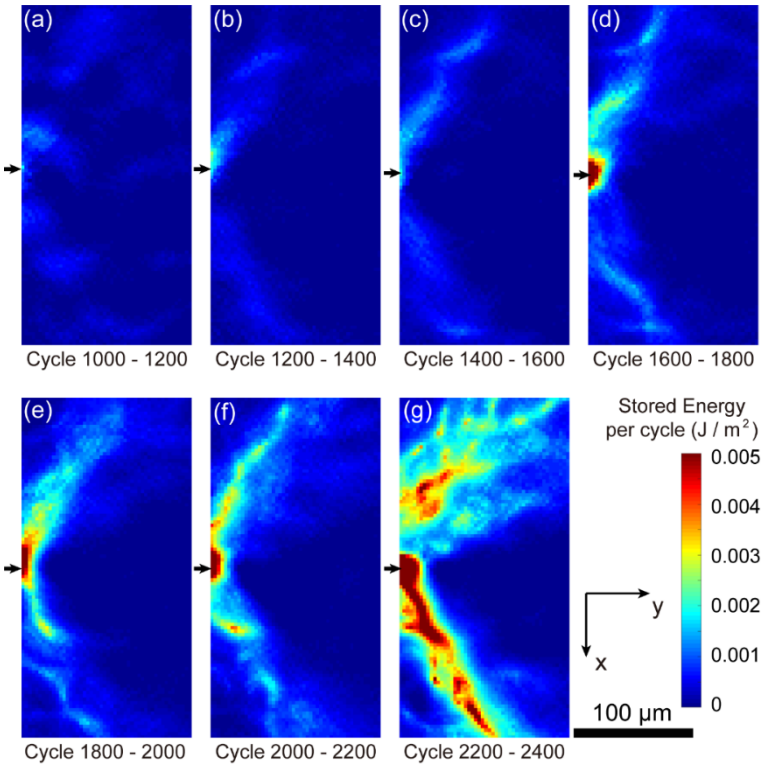


Fig. 5-25. Evolution of cyclic stored energy density distribution in the ROI of Sample AZ

(The black arrow marks the crack tip).

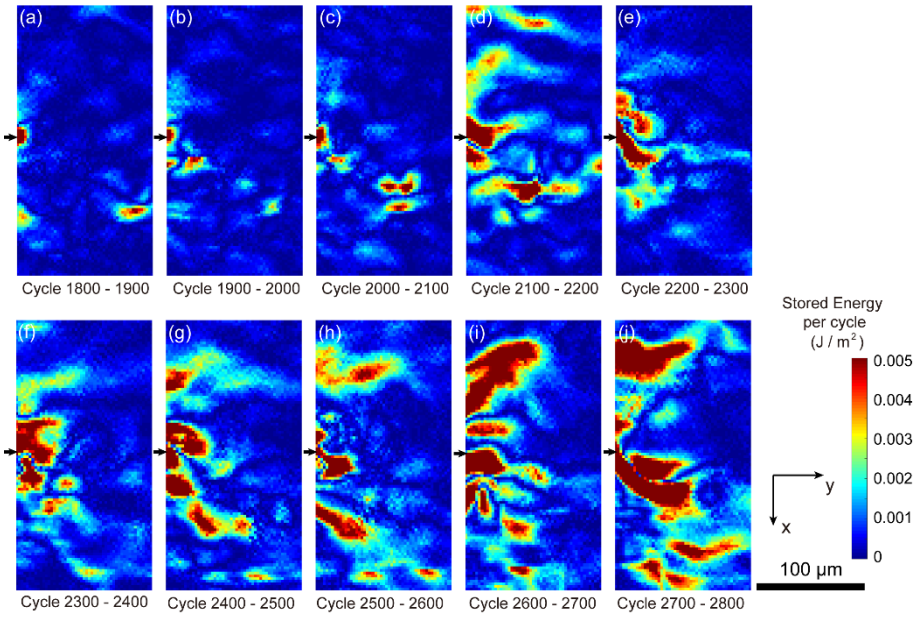


Fig. 5-26. Evolution of cyclic stored energy density distribution in the ROI of Sample BY

(The black arrow marks the crack tip).

Fig. 5-25 and Fig. 5-26 show the evolution of cyclic stored energy density distribution in the ROI of Sample AZ and BY, respectively. The cyclic stored energy density in the ROI sees concentration at the crack-tip in both Sample AZ and BY, however, it shows clear bands developing from crack-tip to two sides in Sample AZ, while it distributes with some dispersed hotspots in Sample BY. A hotspot zone can be identified in front of the crack-tip and usually along the slip bands in both Sample AZ and BY with the highest cyclic stored energy density. The energy stored density within dislocation structures produced by slip in these hotspot zones is argued to provide the mechanistic driving force for the creation of new free surfaces (ie crack surfaces) once the stored energy exceeds the surface energy, thus driving the short crack growth (Wilson et al., 2018; Zheng et al., 2019).

Fig. 5-27 (a) and (b) show the average cyclic dissipated energy density and stored energy density in the ROI versus effective crack length of Sample AZ and BY. The colour red and blue corresponding to Sample AZ and BY. Both the average cyclic dissipated energy density and stored energy density successfully capture the crack growth rate fluctuation near the effective crack length at 450 μm corresponding to the range between cycle 2100 and 2300 due to the microstructural obstacles. Although both quantities reflect the difference on crack growth rate with Sample BY higher than Sample AZ without considering the data of Sample AZ marked by a dashed circle, the trend of cyclic stored energy density performs better in describing the crack growth rate than that of the cyclic dissipated energy density. For example, cyclic dissipated energy density of Sample BY is about 2.5 times of Sample AZ before the effective crack length

at 420 μm, however, the multiple is lower than 2 after 450 um which largely deviates the average multiple at 2.3 between Sample BY and AZ.

Besides the average value in the ROI, which is a relatively large area with 150 μm × 300 μm, the cyclic dissipated energy density and stored energy density at a local point within the hotspot zone are calculated and plotted in Fig. 5-28 versus the effective crack length. This local point is identified around 5 μm away from the crack-tip and the value is averaged with neighbouring data points in 3×3 grids. The trend of the two local quantities have been marked in dashed lines. Fig. 5-28 (a) shows the evolution of the local cyclic dissipated energy density and that Sample AZ exceeds Sample BY at around 480 μm of the effective crack length, which is not following the trend of the crack growth rates. On the contrary, local cyclic stored energy density captures both two features of the crack growth rates with consistent multiplication between Sample BY and Sample AZ and the rate fluctuation occurring between 420 μm and 500 μm of the effective crack length in Sample BY. Therefore, the consideration of cyclic stored energy density as a mechanistic driver for short crack growth is argued to be more appropriate than that of cyclic dissipated energy and other micromechanical quantities such as local stress and strain.

Independent CPFE simulation and theory work on crack tip stored energy density can be found in (Xu et al., 2021). A converged stored energy density value was obtained from the CPFE modelling. In the theory work, the stored energy density was obtained by spatially integrating over slip line length ahead of the crack tip for a single active

slip system in theoretical calculation. It is found that the stored energy density is a non-singular quantity, which has unique advantage to be the driving force for short crack growth in contrast to stress, strain and dissipated energy (all singular at crack tips). In addition, the crack tip stored energy density is related to the classical stress intensity factor. From both the simulation and theoretical results, the stored energy density, as a potential driving force for short crack growth, is microstructure-governed and quantitatively reflects both the crystallographic orientation-dependent short crack growth rate and the effect of local microstructures. Our study firstly measures the cyclic stored energy density at crack-tip in experiment, which substantially underpins interpretations of CPFE simulation and theoretical results.

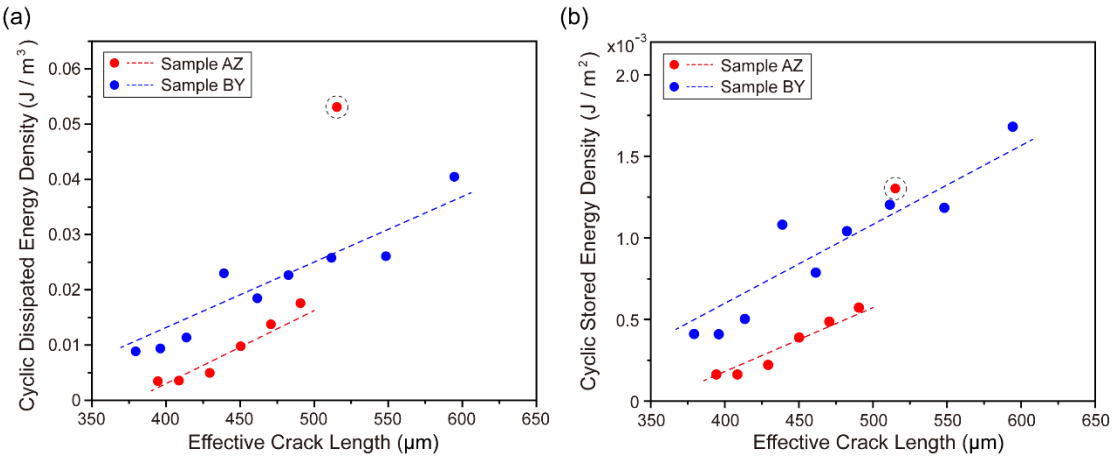


Fig. 5-27. (a) Average cyclic dissipated energy density in the ROI versus effective crack length; (b) average cyclic stored energy density in the ROI versus effective crack length.

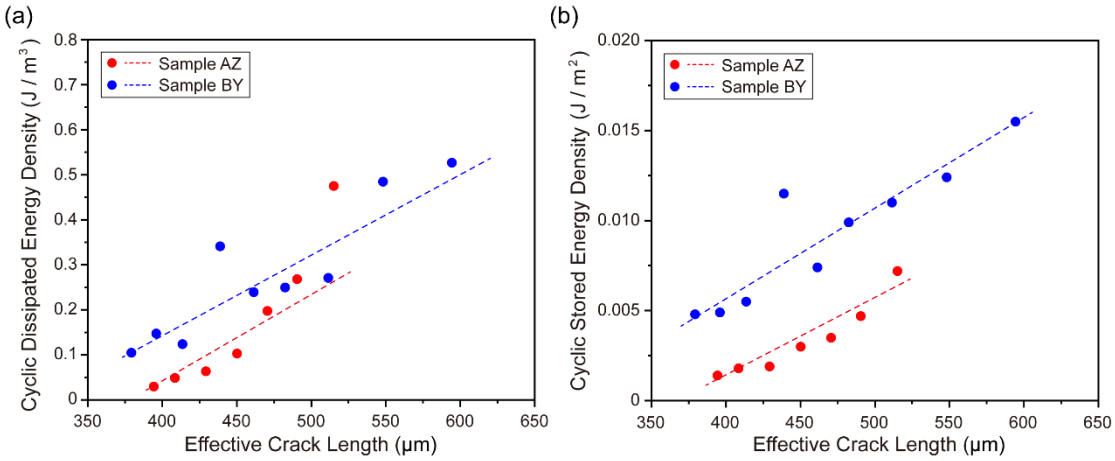


Fig. 5-28. (a) Local cyclic dissipated energy density and (b) local cyclic stored energy density at the crack-tip versus effective crack length.

5.9. Conclusions

Microstructurally-sensitive short crack growth in textured Zircaloy-4 has been investigated in three-point bend tests with SEM, EBSD and in-situ DIC techniques. The main conclusions are as follows:

(1) The short crack growth rate in Zircaloy-4 is sensitive to texture (c-axis direction) and local microstructures. In c//y crystals, which have the c-axes aligned with the y-direction, the crack growth rate is remarkably higher than that in c//z crystals (c-axes aligned with the z-direction). Crack growth retardation is detected when the short crack growing through the c//y crystals due to microstructural obstructions.

(2) Local stress and strain are found to concentrate in the crack-tip area. The dominant strain (xx) localised at the crack-tip and develops towards two sides of the crack. The average peak stress when the short crack grows in c//y crystals is larger than that in c//z crystals compared at the same effective crack length.

(3) A micromechanical quantity cyclic stored energy density, which accounts for local stress, local plastic strain, and GND density, captures the crack growth rate attributed to effect of both texture and local microstructures. The cyclic stored energy density is found to be a potential driving force for short crack growth.

6. Conclusion and future work

Short crack growth in textured Zircaloy-4 has been investigated in this thesis. A blocky alpha microstructure with grain size of ~ 400 μm was achieved by 800 °C heat treatment for two weeks from equiaxed fine-grain in Zircaloy-4 to allow the transgranular short crack growth to be conveniently observed. The interaction between short cracks and local microstructures has been characterised by SEM and EBSD examination.

It was found that the short crack growth was microstructurally sensitive and entirely crystallographic in nature. The crack paths were observed along crystal planes: The 2D surface short crack growth was observed growing along prismatic, pyramidal and potentially basal planes when the growth direction is parallel to the corresponding system Burgers vector, while along only prismatic planes when the growth direction is perpendicular to the Burgers vector. In addition, the non-Burgers vector prism surface crack growth rate is found remarkably (2 ~ 5 times) higher than that for Burgers vector prism surface crack growth.

The local microstructural obstructions such as grain boundaries and triple junctions have a profound effect on the short crack growth rate. The crack growth rate sees an obvious fluctuation when passing these obstructions. On the other hand, short cracks contribute to an interaction with local microstructures in the plastic zone. Slip and twinning are activated due to the local stress state at the crack tip. Prism slip is associated with prism Burgers vector surface crack growth, while prism and <c+a> pyramidal slip activation are both observed in non-Burgers vector prism surface crack

growth. Tensile type twinning is observed in the area near the crack-tip, which is speculated to assist the crack growth when the slip is not sufficient to accommodate the plastic deformation.

To further understand the driving force for short crack growth, a novel experimental design has been conducted to measure a succession of micro-mechanical quantities including strain, stress and GND density in the crack-tip area. This goal was challenged by the rate dependence of Zircaloy-4 in plastic deformation at room temperature, which was discovered in a creep test. The result shows that the strain rate sensitivity of Zircaloy-4 at room temperature is around 0.03 with strain rate at 5×10^{-4} s^{-1}. Such high strain rate sensitivity would result in substantive strain evolution by creep at peak stress hold.

Therefore, a real-time in-situ DIC technique was developed in which the data (speckle pattern pictures) were collected without stopping or holding at the peak load. The strain fields in the crack tip area have been obtained by post-processing the speckle pattern images. It was found that the dominant strain (xx) concentrates at the crack-tip and develops towards two sides of the crack. By extracting the elastic strain from the difference between total strain and plastic strain with the residual strain neglected in the unloaded condition, the local peak stresses were calculated via multiplying the rotated stiffness matrix with the elastic strain tensor. The average peak stress of non-Burgers vector prism surface crack growth is larger than that of Burgers vector prism surface crack growth compared at the same effective crack length. All the features of the short

crack growth rate resulting from the local microstructural effects are similarly picked up, and followed reasonably closely by cyclic stored energy density, which accounts for local stress, local plastic strain, and GND density. Thus, the stored energy density was found to be a potential driving force for short crack growth.

Future work

The present study has successfully addressed a series of micro-scale quantities including local stress, local strain, GND density and stored energy density at the short crack-tip via DIC and EBSD techniques. The stored energy has been proposed as potential driving force for short crack growth. With all the work has been finished to date, a plan for future work has been addressed and will be considered.

Tensile type twinning has been observed during the short crack growth as introduced in Chapter 3 and Chapter 5. It is found that twinning occurs when slip is not enough to accommodate the plastic deformation at the crack tip. Twinning is thought to have profound effect on the crack growth when the amount of twinning is considerable especially in the crack-tip area. More detailed crystallographic characterisation can be achieved by transmission electron microscopy (TEM). In addition, High resolution-EBSD allows residual stress field in the twinning area to be obtained such that the mechanism of the formation of twins near the crack-tip can be investigated from a full-field stress state analysis. Twins are probably introduced by crack growth, meanwhile, thought to interact the crack path and crack growth rate, which makes the transgranular crack growth more complicated.

Critical stored energy density has been successfully applied as a criterion for crack nucleation by (Wan et al., 2014) and (Chen et al., 2018) based on CPFE simulation. In this study, the stored energy density can be calculated firstly by experiments such that it is worthy to valid this criterion for crack nucleation by directly measuring the stored energy density in experiment. Microstructural information including grain morphology and crystallographic orientation can be obtained by EBSD detection as introduced in this work.

The present study has focused on microstructurally-sensitive short crack growth, however, the development of crack-tip strain and stress field during the transition period towards Stage II crack, which is insensitive to local microstructures, is of interest. The traditional method used in this work is applicable to measure the crack growth rate. Meanwhile, all the micro-scale quantities can be obtained via in-situ DIC measurement and EBSD examination, which are useful to further understanding the behaviour of crack growth in the transition stage.

References

Abdolvand, H., Daymond, M.R., Mareau, C., 2011. Incorporation of twinning into a crystal plasticity finite element model: Evolution of lattice strains and texture in Zircaloy-2. Int. J. Plast. 27, 1721–1738. https://doi.org/10.1016/j.ijplas.2011.04.005

Aigner, R., Pusterhofer, S., Pomberger, S., Leitner, M., Stoschka, M., 2019. A probabilistic Kitagawa-Takahashi diagram for fatigue strength assessment of cast aluminium alloys. Mater. Sci. Eng. A 745, 326–334. https://doi.org/10.1016/j.msea.2018.12.108

Akhtar, A., 1973a. Compression of zirconium single crystals parallel to the c-axis. J. Nucl. Mater. 47, 79–86. https://doi.org/10.1016/0022-3115(73)90189-X

Akhtar, A., 1973b. Basal slip in zirconium. Acta Metall. 21, 1–11. https://doi.org/10.1016/0001-6160(73)90213-7

Akhtar, A., Teghtsoonian, A., 1971. Plastic deformation of zirconium single crystals. Acta Metall. 19, 655–663. https://doi.org/10.1016/0001-6160(71)90019-8

Anderson, T.L., 1996. Fracture Mechanics - Fundamentals and Applications, CRC Press, Taylor & Francis Group.

Andersson, H., Persson, C., 2004. In-situ SEM study of fatigue crack growth behaviour in IN718. Int. J. Fatigue 26, 211–219. https://doi.org/10.1016/S0142-1123(03)00172-5

Armas, A.F., Alvarez-Armas, I., Moscato, G., 1996. Dynamic strain aging influence on the cyclic behavior of zircaloy-4. Scr. Mater. 34, 281–285. https://doi.org/10.1016/1359-6462(95)00502-1

Arsenlis, A., Parks, D.M., 1999. Crystallographic aspects of geometrically-necessary and statistically-stored dislocation density. Acta Mater. 47, 1597–1611. https://doi.org/10.1016/S1359-6454(99)00020-8

Asaro, R.J., 1983. Crystal plasticity. J. Appl. Mech. Trans. ASME 50, 921–934. https://doi.org/10.1115/1.3167205

Ashby, M.F., 1970. The deformation of plastically non-homogeneous materials. Philos. Mag. 21, 399–424. https://doi.org/10.1080/14786437008238426

Bair, J., Asle Zaeem, M., Tonks, M., 2015. A review on hydride precipitation in zirconium alloys. J. Nucl. Mater. https://doi.org/10.1016/j.jnucmat.2015.07.014

Basquin, O.H., 1910. The exponential law of endurance tests. Proc. Am. Soc. Test. Mater. 10, 625–630.

Bauschinger, J., 1886. A study of the effects of cyclic thermal stresses on a ductile metal, in: Materials Forum.

Bhat, S.P., Fine, M.E., 2001. Fatigue crack nucleation in iron and a high strength low alloy steel. Mater. Sci. Eng. A 314, 90–96. https://doi.org/10.1016/S0921-5093(00)01918-3

Blochwitz, C., Jacob, S., Tirschler, W., 2008. Grain orientation effects on the growth of short fatigue cracks in austenitic stainless steel. Mater. Sci. Eng. A 496, 59–66. https://doi.org/10.1016/j.msea.2008.04.050

Boas, V.W., Schmid, E., 1936. Zur Temperaturabhangigkeit der Kristallplastizitat. 463–470.
Bowen, A.W., 1978. The influence of crystallographic orientation on the fracture toughness of strongly textured Ti-6Al-4V. Acta Metall. 26, 1423–1433. https://doi.org/10.1016/0001-6160(78)90157-8
Brett, S., Doherty, R.D., 1978. Loss of solute at the fracture surface in fatigued aluminium precipitation-hardened alloys. Mater. Sci. Eng. 32, 255–265. https://doi.org/10.1016/0025-5416(78)90139-8
Brown, L.M., 2013. Cracks and extrusions caused by persistent slip bands. Philos. Mag. 93, 3809–3820. https://doi.org/10.1080/14786435.2013.798048
Bruck, H.A., McNeill, S.R., Sutton, M.A., Peters, W.H., 1989. Digital image correlation using Newton-Raphson method of partial differential correction. Exp. Mech. 29, 261–267. https://doi.org/10.1007/BF02321405
Campbell, J.D., Ferguson, W.G., 1970. The temperature and strain-rate dependence of the shear strength of mild steel. Philos. Mag. 21, 63–82. https://doi.org/10.1080/14786437008238397
Cann, C.D., Sexton, E.E., 1980. Electron Optical Study of Hydride Precipitation and Growth At Crack Tips in Zirconium. Acta Metall. 28, 1215–1221. https://doi.org/10.1016/0001-6160(80)90076-0
Carroll, J.D., Abuzaid, W., Lambros, J., Sehitoglu, H., 2013. High resolution digital image correlation measurements of strain accumulation in fatigue crack growth. Int. J. Fatigue 57, 140–150. https://doi.org/10.1016/j.ijfatigue.2012.06.010
Castelluccio, G.M., McDowell, D.L., 2012. Assessment of small fatigue crack growth driving forces in single crystals with and without slip bands. Int. J. Fract. 176, 49–64. https://doi.org/10.1007/s10704-012-9726-y
Chapetti, M.D., 2003. Fatigue propagation threshold of short cracks under constant amplitude loading. Int. J. Fatigue 25, 1319–1326. https://doi.org/10.1016/S0142-1123(03)00065-3
Chen, B., Jiang, J., Dunne, F.P.E., 2018. Is stored energy density the primary meso-scale mechanistic driver for fatigue crack nucleation? Int. J. Plast. 101, 213–229. https://doi.org/10.1016/j.ijplas.2017.11.005
Chen, B., Jiang, J., Dunne, F.P.E., 2017. Microstructurally-sensitive fatigue crack nucleation in Ni-based single and oligo crystals. J. Mech. Phys. Solids 106, 15–33. https://doi.org/10.1016/j.jmps.2017.05.012
Chen, D.J., Chiang, F.P., Tan, Y.S., Don, H.S., 1993. Digital speckle-displacement measurement using a complex spectrum method. Appl. Opt. 32, 1839. https://doi.org/10.1364/ao.32.001839
Cheng, A.S., Laird, C., 1981. Fatigue Life Behavior of Copper Single Crystals. Part I: Observations of Crack Nucleation. Fatigue Fract. Eng. Mater. Struct. 4, 331–341. https://doi.org/10.1111/j.1460-2695.1981.tb01130.x
Cheng, J., Ghosh, S., 2015. A crystal plasticity FE model for deformation with twin nucleation in magnesium alloys. Int. J. Plast. 67, 148–170. https://doi.org/10.1016/j.ijplas.2014.10.005
Chowdhury, P., Sehitoglu, H., 2016. Mechanisms of fatigue crack growth - A critical

digest of theoretical developments. Fatigue Fract. Eng. Mater. Struct. 39, 652–674. https://doi.org/10.1111/ffe.12392
Christian, J.W., Mahajan, S., 1995. Deformation twinning. Prog. Mater. Sci. 39, 1–157. https://doi.org/10.1007/BF00550122
Ciavarella, M., Monno, F., 2006. On the possible generalizations of the Kitagawa-Takahashi diagram and of the El Haddad equation to finite life. Int. J. Fatigue 28, 1826–1837. https://doi.org/10.1016/j.ijfatigue.2005.12.001
Clausen, B., Tomé, C.N., Brown, D.W., Agnew, S.R., 2008. Reorientation and stress relaxation due to twinning: Modeling and experimental characterization for Mg. Acta Mater. 56, 2456–2468. https://doi.org/10.1016/j.actamat.2008.01.057
Cockeram, B. V., Kammenzind, B.F., 2018. The increase in fatigue crack growth rates observed for Zircaloy-4 in a PWR environment. J. Nucl. Mater. 499, 111–125. https://doi.org/10.1016/j.jnucmat.2017.11.015
Coffin, L.F., 1954. A study of the effects of cyclic thermal stresses on a ductile metal. Trans. Am. Soc. Mech. Eng. 76, 931–950.
Cojocaru, D., Karlsson, A.M., 2009. Assessing plastically dissipated energy as a condition for fatigue crack growth. Int. J. Fatigue 31, 1154–1162. https://doi.org/10.1016/j.ijfatigue.2008.12.009
Cottrell, A.H., Dexter, D.L., 1953. Dislocations and Plastic Flow in Crystals. Oxford Univ. Press. New York 22, 242–243. https://doi.org/10.1119/1.1933704
Cottrell, A.H., Hull, D., 1957. Extrusion and intrusion by cyclic slip in copper. Proc. R. Soc. London. Ser. A. Math. Phys. Sci. 242, 211–213. https://doi.org/10.1098/rspa.1957.0170
Cox, B., 1990. Environmentally-induced cracking of zirconium alloys - A review. J. Nucl. Mater. 170, 1–23. https://doi.org/10.1016/0022-3115(90)90321-D
Dunne, F.P.E., Rugg, D., Walker, A., 2007. Lengthscale-dependent, elastically anisotropic, physically-based hcp crystal plasticity: Application to cold-dwell fatigue in Ti alloys. Int. J. Plast. 23, 1061–1083. https://doi.org/10.1016/j.ijplas.2006.10.013
Dutton, R., Nuttall, K., Puls, M.P., Simpson, L.A., 1977. Mechanisms of Hydrogen Induced Delayed Cracking in Hydride Forming Materials. Met. Trans A 8 A, 1553–1562. https://doi.org/10.1007/BF02644858
E647-93, 1993. Standard Method for Measurement of Fatigue Crack Growth Rates. Am. Soc. Test. Mater. Philadelphia, PA.
Edwards, L., Zhang, Y.H., 1994. Investigation of small fatigue cracks-I. Plastic deformation associated with small fatigue cracks. Acta Metall. Mater. 42, 1413–1421. https://doi.org/10.1016/0956-7151(94)90160-0
El Haddad, M. H., Smith, K.N., Topper, T.H., 1979. Fatigue crack propagation of short cracks. Am. Soc. Mech. Eng. 101, 42–46.
El Haddad, M.H., Topper, T.H., Smith, K.N., 1979. Prediction of non propagating cracks. Eng. Fract. Mech. 11, 573–584. https://doi.org/doi.org/10.1016/0013-7944(79)90081-X
Elber, W., 1970. Fatigue Crack Closure Under Cyclic Tension. Eng. Fract. Mech. 2, 37–44. https://doi.org/10.1016/0013-7944(70)90028-7

Erinosho, T.O., Dunne, F.P.E., 2016. Lattice strains at cracks in single crystal titanium: Elastic distortion and GND contributions. Int. J. Solids Struct. 80, 237–245. https://doi.org/10.1016/j.ijsolstr.2015.11.007

Essmann, U., Gösele, U., Mughrabi, H., 1981. A model of extrusions and intrusions in fatigued metals I. Point-defect production and the growth of extrusions. Philos. Mag. A Phys. Condens. Matter, Struct. Defects Mech. Prop. 44, 405–426. https://doi.org/10.1080/01418618108239541

Evans, A.G., Rawlings, R.D., 1969. The Thermally Activated Deformation of Crystalline Materials. Phys. Status Solidi 34, 9–31. https://doi.org/10.1002/pssb.19690340102

Ewing, J.A., Humfrey, B.A., 1903. The fracture of metals under repeated alternations of stress. Philos. Trans. R. Soc. London 200, 241–250. https://doi.org/10.1098/rsta.1903.0006

Farukh, F., Zhao, L., Jiang, R., Reed, P., Proprentner, D., Shollock, B., 2015. Fatigue crack growth in a nickel-based superalloy at elevated temperature - experimental studies, viscoplasticity modelling and XFEM predictions. Mech. Adv. Mater. Mod. Process. 1, 1–13. https://doi.org/10.1186/s40759-015-0003-4

Fatemi, A., Kurath, P., 1988. Multiaxial Fatigue Life Predictions Under the Influence of Mean-Stresses. J. Eng. Mater. Technol. 110, 380–388.

Fatemi, A., Socie, D.F., 1988. A critical plane approach to multiaxial fatigue damage including out‐of‐phase loading. Fatigue Fract. Eng. Mater. Struct. 11, 149–165. https://doi.org/10.1111/j.1460-2695.1988.tb01169.x

Feltner, C.E., Laird, C., 1967a. Cyclic stress-strain response of F.C.C. metals and alloys-I Phenomenological experiments. Acta Metall. 15, 1621–1632. https://doi.org/10.1016/0001-6160(67)90137-X

Feltner, C.E., Laird, C., 1967b. Cyclic stress-strain response of F.C.C. metals and alloys-II Dislocation structures and mechanisms. Acta Metall. 15, 1633–1653. https://doi.org/10.1016/0001-6160(67)90138-1

Fine, M.E., Bhat, S.P., 2007. A model of fatigue crack nucleation in single crystal iron and copper. Mater. Sci. Eng. A 468–470, 64–69. https://doi.org/10.1016/j.msea.2006.09.127

Fleck, N.A., Hutchinson, J.W., 1997. Strain Gradient Plasticity. Adv. Appl. Mech. 33, 295–361. https://doi.org/10.1016/S0065-2156(08)70388-0

Fleck, N.A., Muller, G.M., Ashby, M.F., Hutchinson, J.W., 1994. Strain gradient plasticity: Theory and experiment. Acta Metall. Mater. 42, 475–487. https://doi.org/10.1016/0956-7151(94)90502-9

Forsyth, P.J.E., 1963. Fatigue damage and crack growth in aluminium alloys. Acta Metall. 11, 703–715. https://doi.org/10.1016/0001-6160(63)90008-7

Forsyth, P.J.E., 1953. Exudation of material from slip bands at the surface of fatigued crystals of an Aluminium-Copper alloy. Nature 171, 172–173.

G.I. Taylor, 1934. The mechanism of plastic deformation of crystals. Part I.-Theoretical. Proc. R. Soc. London. Ser. A 145, 388–404. https://doi.org/10.1098/rspa.1934.0107

Gao, Y., Stölken, J.S., Kumar, M., Ritchie, R.O., 2007. High-cycle fatigue of nickel-

base superalloy René 104 (ME3): Interaction of microstructurally small cracks with grain boundaries of known character. Acta Mater. 55, 3155–3167. https://doi.org/10.1016/j.actamat.2007.01.033
Gerspach, F., Bozzolo, N., Wagner, F., 2009. About texture stability during primary recrystallization of cold-rolled low alloyed zirconium. Scr. Mater. 60, 203–206. https://doi.org/10.1016/j.scriptamat.2008.09.031
Gibbs, G.B., 1969. Thermodynamic analysis of dislocation glide controlled by dispersed local obstacles. Mater. Sci. Eng. 4, 313–328. https://doi.org/10.1016/0025-5416(69)90026-3
Glinka, G., 1982. A cumulative model of fatigue crack growth. Int. J. Fatigue 4, 59–67. https://doi.org/10.1016/0142-1123(82)90061-5
Golos, K., Ellyin, F., 1988. A total strain energy density theory for cumulative fatigue damage. J. Press. Vessel Technol. Trans. ASME 110, 36–41. https://doi.org/10.1115/1.3265565
Gong, J., Benjamin Britton, T., Cuddihy, M.A., Dunne, F.P.E., Wilkinson, A.J., 2015. <a> Prismatic, <a> basal, and <c+a> slip strengths of commercially pure Zr by micro-cantilever tests. Acta Mater. 96, 249–257. https://doi.org/10.1016/j.actamat.2015.06.020
Goodman, J., 1899. Mechanics applied to engineering. London: Longmans Green.
Gough, H.J., 1933. Crystalline structure in relation to failure of metals - especially by fatigue. Proc. Am. Soc. Test. Mater.
Granato, A. V., Lücke, K., Schlipf, J., Teutonico, L.J., 1964. Entropy factors for thermally activated unpinning of dislocations. J. Appl. Phys. 35, 2732–2745. https://doi.org/10.1063/1.1713833
Granoto, A.V., 1973. Metallurgical effects at high strain rates. Pergamon.
Griffith, A.A., 1921. The phenomena of rupture and flow in solids. Philos. Trans. R. Soc. A Math. Phys. Eng. Sci. 221, 163–198.
Hansson, P., Melin, S., 2010. Grain boundary influence on short fatigue crack growth rate. Int. J. Fract. 165, 199–210. https://doi.org/10.1007/s10704-010-9512-7
Hasegawa, T., Yakou, T., Kocks, U.F., 1986. Forward and reverse rearrangements of dislocations in tangled walls. Mater. Sci. Eng. 81, 189–199. https://doi.org/10.1016/0025-5416(86)90262-4
Hasija, V., Ghosh, S., Mills, M.J., Joseph, D.S., 2003. Deformation and creep modeling in polycrystalline Ti-6Al alloys. Acta Mater. 51, 4533–4549. https://doi.org/10.1016/S1359-6454(03)00289-1
Hassan, T., Kyriakides, S., 1994. Ratcheting of cyclically hardening and softening materials: I. Uniaxial behavior. Int. J. Plast. 10, 149–184. https://doi.org/10.1016/0749-6419(94)90033-7
Hayes, T.A., Kassner, M.E., 2006. Creep of zirconium and zirconium alloys. Metall. Mater. Trans. A Phys. Metall. Mater. Sci. 37, 2389–2396. https://doi.org/10.1007/BF02586213
Hickman, B.S., 1969. The formation of omega phase in titanium and zirconium alloys: A review. J. Mater. Sci. 4, 554–563. https://doi.org/10.1007/BF00550217
Hirth, J.P., Nix, W.D., 1969. An analysis of the thermodynamics of dislocation glide

35, 177–188. https://doi.org/10.1119/1.1933704
Ho, H.S., Risbet, M., Feaugas, X., 2015. On the unified view of the contribution of plastic strain to cyclic crack initiation: Impact of the progressive transformation of shear bands to persistent slip bands. Acta Mater. 85, 155–167. https://doi.org/10.1016/j.actamat.2014.11.020
Holzapfel, C., Schäf, W., Marx, M., Vehoff, H., Mücklich, F., 2007. Interaction of cracks with precipitates and grain boundaries: Understanding crack growth mechanisms through focused ion beam tomography. Scr. Mater. 56, 697–700. https://doi.org/10.1016/j.scriptamat.2006.12.025
Huffman, P.J., 2016. A strain energy based damage model for fatigue crack initiation and growth. Int. J. Fatigue 88, 197–204. https://doi.org/10.1016/j.ijfatigue.2016.03.032
Hutchinson, J.W., 1968. Singular behaviour at the end of a tensile crack in a hardening material. J. Mech. Phys. Solids 16, 13–31.
Inglis, C.E., 1913. Stresses in a plate due to the presence of cracks and sharp corners. Trans. Inst. Nav. Archit. 55, 219–241.
Irwin, G.R., 1961. Plastic zone near a crack and fracture toughness. Sagamore Res. Conf. Proc.
Irwin, G.R., 1957. Analysis of Stresses and Strains Near the End of a Crack Traversing a Plate. J. Appl. Mech. 24, 361–364.
Irwin, G.R., 1956. Onset of fast crack propagation in high strenght steel and aluminum alloys. Nav. Res. Lab.
Irwin, G.R., 1948. Fracture Dynamics, Fracturing of Metals, American Society for Metals. Cleveland.
Jiang, J., Britton, T.B., Wilkinson, A.J., 2013. Measurement of geometrically necessary dislocation density with high resolution electron backscatter diffraction: Effects of detector binning and step size. Ultramicroscopy 125, 1–9. https://doi.org/10.1016/j.ultramic.2012.11.003
Jiang, J., Zhang, T., Dunne, F.P.E., Britton, T. Ben, 2016. Deformation compatibility in a single crystalline Ni superalloy. Proc. R. Soc. A Math. Phys. Eng. Sci. 472. https://doi.org/10.1098/rspa.2015.0690
Jiang, Y., Feng, M., 2004. Modeling of fatigue crack propagation. J. Eng. Mater. Technol. Trans. ASME 126, 77–86. https://doi.org/10.1115/1.1631026
Jiang, Y., Sehitoglu, H., 1994a. Cyclic ratchetting of 1070 steel under multiaxial stress states. Int. J. Plast. 10, 579–608. https://doi.org/10.1016/0749-6419(94)90015-9
Jiang, Y., Sehitoglu, H., 1994b. Multiaxial cyclic ratchetting under multiple step loading. Int. J. Plast. 10, 849–870. https://doi.org/10.1016/0749-6419(94)90017-5
Jun, T.S., Armstrong, D.E.J., Britton, T.B., 2016a. A nanoindentation investigation of local strain rate sensitivity in dual-phase Ti alloys. J. Alloys Compd. 672, 282–291. https://doi.org/10.1016/j.jallcom.2016.02.146
Jun, T.S., Zhang, Z., Sernicola, G., Dunne, F.P.E., Britton, T.B., 2016b. Local strain rate sensitivity of single α phase within a dual-phase Ti alloy. Acta Mater. 107,

298–309. https://doi.org/10.1016/j.actamat.2016.01.057
Kang, G., 2008. Ratchetting: Recent progresses in phenomenon observation, constitutive modeling and application. Int. J. Fatigue 30, 1448–1472. https://doi.org/10.1016/j.ijfatigue.2007.10.002
Kaschner, G.C., Gray, G.T., 2000. The influence of texture and interstitial impurities on the mechanical behavior of zirconium. Metall. Mater. Trans. A 31A, 1997–2003. https://doi.org/10.1063/1.55659
Kaschner, G.C., Tomé, C.N., Beyerlein, I.J., Vogel, S.C., Brown, D.W., McCabe, R.J., 2006. Role of twinning in the hardening response of zirconium during temperature reloads. Acta Mater. 54, 2887–2896. https://doi.org/10.1016/j.actamat.2006.02.036
Kearns, J.J., 2001. On the relationship among "f" texture factors for the principal planes of zirconium, hafnium and titanium alloys. J. Nucl. Mater. 299, 171–174. https://doi.org/10.1016/S0022-3115(01)00686-9
Kearns, J.J., 1965. Thermal Expansion and Preferred Orientation in Zircaloy 4500, 37.
Kerr, M., Daymond, M.R., Holt, R.A., Almer, J.D., 2010. Mapping of crack tip strains and twinned zone in a hexagonal close packed zirconium alloy. Acta Mater. 58, 1578–1588. https://doi.org/10.1016/j.actamat.2009.10.064
Khan, A.S., Liu, H., 2012. Variable strain rate sensitivity in an aluminum alloy: Response and constitutive modeling. Int. J. Plast. 36, 1–14. https://doi.org/10.1016/j.ijplas.2012.02.001
Kiener, D., Guruprasad, P.J., Keralavarma, S.M., Dehm, G., Benzerga, A.A., 2011. Work hardening in micropillar compression: In situ experiments and modeling. Acta Mater. 59, 3825–3840. https://doi.org/10.1016/j.actamat.2011.03.003
King, A., Ludwig, W., Herbig, M., Buffire, J.Y., Khan, A.A., Stevens, N., Marrow, T.J., 2011. Three-dimensional in situ observations of short fatigue crack growth in magnesium. Acta Mater. 59, 6761–6771. https://doi.org/10.1016/j.actamat.2011.07.034
Kitagawa, H., Takahashi, S., 1976. Applicability of fracture mechanics to very small cracks or the cracks in the early stage. Proc 2nd Int conf mech Behav. mater - ICM2 627–31.
Kocks, U.F., Mecking, H., 2003. Physics and phenomenology of strain hardening: the FCC case. Prog. Mater. Sci. 48, 171–273. https://doi.org/10.4324/9781315279015
Korsunsky, A.M., Dini, D., Dunne, F.P.E., Walsh, M.J., 2007. Comparative assessment of dissipated energy and other fatigue criteria. Int. J. Fatigue 29, 1990–1995. https://doi.org/10.1016/j.ijfatigue.2007.01.007
Kysar, J.W., Saito, Y., Oztop, M.S., Lee, D., Huh, W.T., 2010. Experimental lower bounds on geometrically necessary dislocation density. Int. J. Plast. 26, 1097–1123. https://doi.org/10.1016/j.ijplas.2010.03.009
Lee, D., 1972. Strain rate dependent hardening in zirconium and zirconium-niobium alloy. Can. Metall. Q. 11, 113–117. https://doi.org/10.1179/cmq.1972.11.1.113
Lee, D., 1970. The Strain Rate Dependent Plastic Flow Behavior of Zirconium and Its Alloys. Metall. Mater. Trans. A Phys. Metall. Mater. Sci. 1, 1607–1616.

Lee, K.W., Kim, S.K., Kim, K.T., Hong, S.I., 2001. Ductility and strain rate sensitivity of Zircaloy-4 nuclear fuel claddings. J. Nucl. Mater. 295, 21–26. https://doi.org/10.1016/S0022-3115(01)00509-8

Lefebvre, D., Ellyin, F., 1984. Cyclic response and inelastic strain energy in low cycle fatigue. Int. J. Fatigue 6, 9–15. https://doi.org/10.1016/0142-1123(84)90003-3

Li, L., Zhang, Z., Shen, G., 2015. Influence of grain size on fatigue crack propagation and acoustic emission features in commercial-purity zirconium. Mater. Sci. Eng. A 636, 35–42. https://doi.org/10.1016/j.msea.2015.03.046

Lin, X., Haicheng, G., 1998. High cycle fatigue properties and microstructure of zirconium and zircaloy-4 under reversal bending. Mater. Sci. Eng. A 252, 166–173. https://doi.org/10.1016/S0921-5093(98)00688-1

Liu, Y., Wan, W., Chamaa, S.E., Wenman, M.R., Davies, C.M., Dunne, F.P.E., 2020. Creep and strain rate sensitivity in Zircaloy-4 (Under Preparation). Int. J. Plast.

Ma, B., Laird, C., 1989a. Overview of fatigue behavior in copper single crystals - II. Population, size distribution and growth kineticsw of stage I cracks for tests at constant strain amplitude. Acta Metall. 37, 337–348.

Ma, B., Laird, C., 1989b. Overview of fatigue behavior in copper single crystals-I. Surface morphology and stage I crack initiation sites for tests at constant strain amplitude. Acta Metall. 37, 325–336. https://doi.org/10.1016/0001-6160(89)90217-4

Macdonald, V., Le Boulch, D., Menibus, A.H. de, Besson, J., Auzoux, Q., Crépin, J., Le Jolu, T., 2014. Fracture of Zircaloy-4 Fuel Cladding Tubes with Hydride Blisters. Procedia Mater. Sci. 3, 233–238. https://doi.org/10.1016/j.mspro.2014.06.041

Maierhofer, J., Gänser, H.P., Pippan, R., 2015. Modified Kitagawa-Takahashi diagram accounting for finite notch depths. Int. J. Fatigue 70, 503–509. https://doi.org/10.1016/j.ijfatigue.2014.07.007

Malitckii, E., Remes, H., Lehto, P., Yagodzinskyy, Y., Bossuyt, S., Hänninen, H., 2018. Strain accumulation during microstructurally small fatigue crack propagation in bcc Fe-Cr ferritic stainless steel. Acta Mater. 144, 51–59. https://doi.org/10.1016/j.actamat.2017.10.038

Man, J., Obrtlík, K., Polák, J., 2009. Extrusions and intrusions in fatigued metals. Part 1. State of the art and history. Philos. Mag. 89, 1295–1336. https://doi.org/10.1080/14786430902917616

Manson, S.S., 1954. Behavior Of Materials Under Conditions Of Thermal Stress. NACA Rep. 1170.

Marrow, T.J., Mostafavi, M., Hashimoto, T., Thompson, G.E., 2014. A quantitative three-dimensional in situ study of a short fatigue crack in a magnesium alloy. Int. J. Fatigue 66, 183–193. https://doi.org/10.1016/j.ijfatigue.2014.04.003

McCabe, R.J., Cerreta, E.K., Misra, A., Kaschner, G.C., Tomé, C.N., 2006. Effects of texture, temperature and strain on the deformation modes of zirconium. Philos. Mag. 86, 3595–3611. https://doi.org/10.1080/14786430600684500

McDowell, D.L., Dunne, F.P.E., 2010. Microstructure-sensitive computational modeling of fatigue crack formation. Int. J. Fatigue 32, 1521–1542.

https://doi.org/10.1016/j.ijfatigue.2010.01.003
Mine, Y., Ando, S., Takashima, K., 2011. Crystallographic fatigue crack growth in titanium single crystals. Mater. Sci. Eng. A 528, 7570–7578. https://doi.org/10.1016/j.msea.2011.06.079
Miner, M.A., 1945. Cumulative damage in fatigue. J. Appl. Mech. 12, 159–164.
Molodov, D.A., Bozzolo, N., 2010. Observations on the effect of a magnetic field on the annealing texture and microstructure evolution in zirconium. Acta Mater. 58, 3568–3581. https://doi.org/10.1016/j.actamat.2010.02.027
Morris, W.L., 1980. The noncontinuum crack tip deformation behavior of surface microcracks. Metall. Trans. A 11, 1117–1123. https://doi.org/10.1007/BF02668135
Morris, W.L., James, M.R., Buck, O., 1981. Growth rate models for short surface cracks in Al 2219-T851. Metall. Trans. A, Phys. Metall. Mater. Sci. 12 A, 57–64. https://doi.org/10.1007/BF02648508
Mughrabi, H., 1978. The cyclic hardening and saturation behaviour of copper single crystals. Mater. Sci. Eng. 33, 207–223. https://doi.org/10.1016/0025-5416(78)90174-X
Mura, T., Nakasone, Y., 1990. A theory of fatigue crack initiation in solids. J. Appl. Mech. 57, 61–70. https://doi.org/10.1016/0921-5093(94)90959-8
Musinski, W.D., McDowell, D.L., 2012. Microstructure-sensitive probabilistic modeling of HCF crack initiation and early crack growth in Ni-base superalloy IN100 notched components. Int. J. Fatigue 37, 41–53. https://doi.org/10.1016/j.ijfatigue.2011.09.014
Naderi, M., Amiri, M., Iyyer, N., Kang, P., Phan, N., 2016. Prediction of fatigue crack nucleation life in polycrystalline AA7075-T651 using energy approach. Fatigue Fract. Eng. Mater. Struct. 39, 167–179. https://doi.org/10.1111/ffe.12346
Nakajima, K., Terao, K., Miyata, T., 1998. The effect of microstructure on fatigue crack propagation of α + β titanium alloys In-situ observation of short fatigue crack growth. Mater. Sci. Eng. A 243, 176–181. https://doi.org/10.1016/s0921-5093(97)00797-1
Navarro, A., de los Rios, E.R., 1988. Short and long fatigue crack growth: A unified model. Philos. Mag. A Phys. Condens. Matter, Struct. Defects Mech. Prop. 57, 15–36. https://doi.org/10.1080/01418618808204496
Ng, B.C., Simkin, B.A., Crimp, M.A., Bieler, T.R., 2004. The role of mechanical twinning on microcrack nucleation and crack propagation in a near-γ TiAl alloy. Intermetallics 12, 1317–1323. https://doi.org/10.1016/j.intermet.2004.03.015
Nielsen, R.H., Wilfing, G., 2012. Zirconium and Zirconium Compounds. https://doi.org/10.1002/14356007.a28
Northwood, D.O., 1985. The development and applications of zirconium alloys. Mater. Des. 6, 58–70. https://doi.org/10.1007/978-1-4615-4257-5_20
Orowan, E., 1948. Fracture and Strength of Solids. Rep. Prog. Phys. VII, 185–232. https://doi.org/10.1088/0034-4885/77/5/056502
Palmgren, A., 1924. Die Lebensdauer von Kugellagern. Zeitschrift des Vereins Dtsch. Ingenieure 68, 339–341.

Pan, B., Qian, K., Xie, H., Asundi, A., 2009. Two-dimensional digital image correlation for in-plane displacement and strain measurement: A review. Meas. Sci. Technol. 20. https://doi.org/10.1088/0957-0233/20/6/062001

Pandarinathan, P.R., Vasudevan, P., 1980. Low-cycle fatigue studies on nuclear reactor Zircaloy-2 fuel tubes at room temperature, 300 and 350°C. J. Nucl. Mater. 91, 47–58. https://doi.org/10.1016/0022-3115(80)90031-8

Paris, P., Erdogan, F., 1963. A critical analysis of crack propagation laws. J. Basic Eng. Trans. ASME 85, 528–533. https://doi.org/10.1115/1.3656900

Paul, S.K., Sivaprasad, S., Dhar, S., Tarafder, S., 2011. Key issues in cyclic plastic deformation: Experimentation. Mech. Mater. 43, 705–720. https://doi.org/10.1016/j.mechmat.2011.07.011

Paul, S.K., Sivaprasad, S., Dhar, S., Tarafder, S., 2010. Ratcheting and low cycle fatigue behavior of SA333 steel and their life prediction. J. Nucl. Mater. 401, 17–24. https://doi.org/10.1016/j.jnucmat.2010.03.014

Pettersson, K., 1975. Low-cycle fatigue properties of Zircaloy-2 cladding. J. Nucl. Mater. 56, 91–102. https://doi.org/10.1016/0022-3115(75)90201-9

Piercy, G.R., 1968. Mechanisms for the in-reactor creep of Zirconium alloys. J. Nucl. Mater. 26, 18–50. https://doi.org/10.1016/0022-3115(68)90157-8

Pineau, A., McDowell, D.L., Busso, E.P., Antolovich, S.D., 2016. Failure of metals II: Fatigue. Acta Mater. 107, 484–507. https://doi.org/10.1016/j.actamat.2015.05.050

Proust, G., Tomé, C.N., Kaschner, G.C., 2007. Modeling texture, twinning and hardening evolution during deformation of hexagonal materials. Acta Mater. 55, 2137–2148. https://doi.org/10.1016/j.actamat.2006.11.017

Puls, M.P., 1990. Effects of crack tip stress states and hydride-matrix interaction stresses on delayed hydride cracking. Metall. Trans. A, Phys. Metall. Mater. Sci. 21 A, 2905–2917. https://doi.org/10.1007/BF02647211

Radon, J.C., 1982. A model for fatigue crack growth in a threshold region. Int. J. Fatigue 4, 161–166. https://doi.org/10.1016/0142-1123(82)90044-5

Ramberg, W., Osgood, W.R., 1943. Description of Stress-Strain curves by three parameters, in: Washington DC: National Advisory Committee for Aeronautics.

Rapperport, E.J., 1959. Room temperature deformation porcesses in zirconium. Acta Metall. 7, 254–260.

Regazzoni, G., Kocks, U.F., Follansbee, P.S., 1987. Dislocation kinetics at high strain rates. Acta Metall. 35, 2865–2875. https://doi.org/10.1016/0001-6160(87)90285-9

Rice, J.R., 1968. A path independent integral and the approximate analysis of strain concentration by notches and cracks. J. Appl. Mech. 35, 379–386.

Rice, J.R., Rosengren, G.F., 1968. Plane strain deformation near a crack tip in a power-law hardening material. J. Mech. Phys. Solids 16, 1–12. https://doi.org/10.1016/0022-5096(68)90013-6

Ruggles, T.J., Fullwood, D.T., 2013. Estimations of bulk geometrically necessary dislocation density using high resolution EBSD. Ultramicroscopy 133, 8–15. https://doi.org/10.1016/j.ultramic.2013.04.011

Salinas-Rodriguez, A., 1995. Grain size effects on the texture evolution of α-Zr. Acta Metall. Mater. 43, 485–498. https://doi.org/10.1016/0956-7151(94)00238-D
Sangid, M.D., Maier, H.J., Sehitoglu, H., 2011a. A physically based fatigue model for prediction of crack initiation from persistent slip bands in polycrystals. Acta Mater. 59, 328–341. https://doi.org/10.1016/j.actamat.2010.09.036
Sangid, M.D., Maier, H.J., Sehitoglu, H., 2011b. An energy-based microstructure model to account for fatigue scatter in polycrystals. J. Mech. Phys. Solids 59, 595–609. https://doi.org/10.1016/j.jmps.2010.12.014
Santus, C., Taylor, D., 2009. Physically short crack propagation in metals during high cycle fatigue. Int. J. Fatigue 31, 1356–1365. https://doi.org/10.1016/j.ijfatigue.2009.03.002
Sauzay, M., Gilormini, P., 2002. Influence of surface effects on fatigue of microcracks nucleation. Theor. Appl. Fract. Mech. 38, 53–62. https://doi.org/10.1016/S0167-8442(02)00080-0
Schaef, W., Marx, M., Vehoff, H., Heckl, A., Randelzhofer, P., 2011. A 3-D view on the mechanisms of short fatigue cracks interacting with grain boundaries. Acta Mater. 59, 1849–1861. https://doi.org/10.1016/j.actamat.2010.11.051
Shamsaei, N., Fatemi, A., 2014. Small fatigue crack growth under multiaxial stresses. Int. J. Fatigue 58, 126–135. https://doi.org/10.1016/j.ijfatigue.2013.02.002
Skelton, R.P., 1991. Energy criterion for high temperature low cycle fatigue failure. Mater. Sci. Technol. (United Kingdom) 7, 427–440. https://doi.org/10.1179/mst.1991.7.5.427
Skelton, R.P., Loveday, M.S., 1997. A re-interpretation of the BCR/VAMAS low cycle fatigue intercomparison programme using an energy criterion. Mater. High Temp. 14, 53–68. https://doi.org/10.1080/09603409.1997.11689527
Skelton, R.P., Rees, C.J., Webster, G.A., 1996. Energy damage summation methods for crack initiation and growth during block loading in high-temperature low-cycle fatigue. Fatigue Fract. Eng. Mater. Struct. 19, 287–297. https://doi.org/10.1111/j.1460-2695.1996.tb00967.x
Skelton, R.P., Vilhelmsen, T., Webster, G.A., 1998. Energy criteria and cumulative damage during fatigue crack growth. Int. J. Fatigue 20, 641–649. https://doi.org/10.1016/S0142-1123(98)00027-9
Skippon, T., Cochrane, C., Daymond, M.R., 2019. Crystallographic orientation sensitive measurement of strain rate sensitivity in Zircaloy-2 via synchrotron X-ray diffraction. Int. J. Plast. 113, 1–17. https://doi.org/10.1016/j.ijplas.2018.09.003
Snowden, K.U., Stathers, P.A., 1977. The fatigue behaviour of α-zirconium and Zircaloy-2 in the temperature range 20 to 700 °C. J. Nucl. Mater. 67, 215–228.
Storer, S.C., Fitzpatrick, M.E., Hainsworth, S. V., Rist, M.A., 2016. Experimental study of room-temperature indentation viscoplastic 'creep' in zirconium. Philos. Mag. 96, 2547–2563. https://doi.org/10.1080/14786435.2016.1209310
Stroh, A.N., 1954. The formation of cracks as a result of plastic flow. Proc. R. Soc. A Math. Phys. Eng. Sci. 223, 404–414. https://doi.org/doi.org/10.1098/rspa.1954.0124

Stroh, A.N., 1953. A theoretical calculation of the stored energy in a work-hardened material. Proc. R. Soc. London. Ser. A. Math. Phys. Sci. 218, 391–400. https://doi.org/10.1098/rspa.1953.0112
Suresh, S., 1998. Fatigue of Materials, Second Edi. ed, Fatigue of Materials. Cambridge University Press, Cambridge. https://doi.org/10.1017/cbo9780511806575
Suresh, S., Ritchie, R.O., 1984. Propagation of short fatigue cracks. Int. Met. Rev. 29, 445–473. https://doi.org/10.1179/imtr.1984.29.1.445
Tada, H., Paris, P.C., Irwin, G.R., 1973. The stress analysis of cracks handbook.
Tanaka, K., Akiniwa, Y., Nakai, Y., Wei, R.P., 1986. Modelling of small fatigue crack growth interacting with grain boundary. Eng. Fract. Mech. 24, 803–819. https://doi.org/10.1016/0013-7944(86)90266-3
Tanaka, K., Mura, T., 1981. Dislocation model for fatigue crack initiation. J. Appl. Mech. 48, 97–103.
Tang, W., Halm, K.L., Trinkle, D.R., Koker, M.K.A., Lienert, U., Kenesei, P., Beaudoin, A.J., 2015. A study of stress relaxation in AZ31 using high-energy X-ray diffraction. Acta Mater. 101, 71–79. https://doi.org/10.1016/j.actamat.2015.08.072
Tenckhoff, E., 1988. Deformation mechanisms, texture, and anisotropy in Zirconium and Zircaloy. J. Chem. Inf. Model. https://doi.org/10.1017/CBO9781107415324.004
Thompson, N., Wadsworth, N., Louat, N., 1956. The origin of fatigue fracture in copper. Philos. Mag. 1, 113–126. https://doi.org/10.1080/14786435608238086
Tiwari, S.N., Lloyd, D.J., Tangri, K., 1972. Deformation of Polycrystalline Zirconium. Met. Trans 3, 2605–2612. https://doi.org/10.1007/BF02644236
Toffolon-Masclet, C., Guilbert, T., Brachet, J.C., 2008. Study of secondary intermetallic phase precipitation/dissolution in Zr alloys by high temperature-high sensitivity calorimetry. J. Nucl. Mater. 372, 367–378. https://doi.org/10.1016/j.jnucmat.2007.04.042
Tokaji, K., Ogawa, T., Harada, Y., 1987. Evaluation on limitation of linear elastic fracture mechanics for small fatigue crack growth. Fatigue Fract. Eng. Mater. Struct. 10, 281–289. https://doi.org/10.1111/j.1460-2695.1987.tb00207.x
Tokaji, K., Ogawa, T., Ohya, K., 1994. The effect of grain size on fatigue crack growth in pure titanium. Int. J. Fatigue 16, 571–578. https://doi.org/10.1111/j.1460-2695.1995.tb00861.x
Tokaji, K., Ogawa, T., Osako, S., 1988. The growth of microstructurally small fatigue cracks in a ferritic‐pearlitic steel. Fatigue Fract. Eng. Mater. Struct. 11, 331–342. https://doi.org/10.1111/j.1460-2695.1988.tb01387.x
Tome, C.N., 1991. A model for texture development dominated by deformation twinning: application to zirconium alloys. Acta Metall. 39, 2667–2680.
Tong, J., Lin, B., Lu, Y.W., Madi, K., Tai, Y.H., Yates, J.R., Doquet, V., 2015. Near-tip strain evolution under cyclic loading: In situ experimental observation and numerical modelling. Int. J. Fatigue 71, 45–52. https://doi.org/10.1016/j.ijfatigue.2014.02.013

Tong, J., Zhao, L.G., Lin, B., 2013. Ratchetting strain as a driving force for fatigue crack growth. Int. J. Fatigue 46, 49–57. https://doi.org/10.1016/j.ijfatigue.2012.01.003
Tong, V.S., 2016. EBSD CHARACTERISATION OF HETEROGENEOUS MICROSTRUCTURES IN ZIRCONIUM ALLOYS.
Tong, V.S., Britton, T. Ben, 2017. Formation of very large 'blocky alpha' grains in Zircaloy-4. Acta Mater. 129, 510–520. https://doi.org/10.1016/j.actamat.2017.03.002
Uematsu, Y., Kakiuchi, T., Tamada, K., Kamiya, Y., 2016. EBSD analysis of fatigue crack initiation behavior in coarse-grained AZ31 magnesium alloy. Int. J. Fatigue 84, 1–8. https://doi.org/10.1016/j.ijfatigue.2015.11.010
Umakoshi, Y., Nakano, T., Ogawa, B., 1996. Orientation dependence of fracture behavior of Ti3Al single crystals with D019 structure. Scr. Mater. 34, 1161–1169. https://doi.org/10.1016/1359-6462(95)00645-1
Venkataraman, G., Chung, Y.W., Nakasone, Y., Mura, T., 1990. Free energy formulation of fatigue crack initiation along persistent slip bands: calculation of SN curves and crack depths. Acta Metall. Mater. 38, 31–40. https://doi.org/10.1016/0956-7151(90)90132-Z
Wan, V.V.C., Jiang, J., MacLachlan, D.W., Dunne, F.P.E., 2016. Microstructure-sensitive fatigue crack nucleation in a polycrystalline Ni superalloy. Int. J. Fatigue 90, 181–190. https://doi.org/10.1016/j.ijfatigue.2016.04.013
Wan, V.V.C., Maclachlan, D.W., Dunne, F.P.E., 2014. A stored energy criterion for fatigue crack nucleation in polycrystals. Int. J. Fatigue 68, 90–102. https://doi.org/10.1016/j.ijfatigue.2014.06.001
Wang, H., Wu, P., Kurukuri, S., Worswick, M.J., Peng, Y., Tang, D., Li, D., 2018. Strain rate sensitivities of deformation mechanisms in magnesium alloys. Int. J. Plast. 107, 207–222. https://doi.org/10.1016/j.ijplas.2018.04.005
Ward-Close, C.M., Beevers, C.J., 1980. The influence of grain orientation on the mode and rate of fatigue crack growth in α-titanium. Metall. Trans. A 11, 1007–1017. https://doi.org/10.1007/BF02654715
Warren, M.R., Beevers, C.J., 1970. Fatigue life and twinning in alpha-zirconium. Metall. Mater. Trans. 1, 1657–1661.
Washburn, D.F., 1964. The formation of large grains in alpha Zircaloy-4 during heat treatment after small plastic deformations.
Wells, A.A., 1961. Unstable Crack Propagation in Metals: Cleavage and Fast Fracture. Proc. Crack Propag. Symp. 210–230.
Wilkinson, A.J., Britton, T. Ben, 2012. Strains, planes, and EBSD in materials science. Mater. Today 15, 366–376. https://doi.org/10.1016/S1369-7021(12)70163-3
Wilkinson, A.J., Meaden, G., Dingley, D.J., 2006. High resolution mapping of strains and rotations using electron backscatter diffraction. Mater. Sci. Technol. 22, 1271–1278. https://doi.org/10.1179/174328406X130966
Wilkinson, A.J., Roberts, S.G., 1996. A dislocation model for the two critical stress intensities required for threshold fatigue crack propagation. Scr. Mater. 35,

1365–1371. https://doi.org/10.1016/1359-6462(96)00301-6
Wilkinson, A.J., Roberts, S.G., Hirsch, P.B., 1998. Modelling the threshold conditions for propagation of stage I fatigue cracks. Acta Mater. 46, 379–390. https://doi.org/10.1016/S1359-6454(97)00290-5
Willaime, F., Massobrio, C., 1989. Temperature-induced hcp-bcc phase transformation in zirconium: A lattice and molecular-dynamics study based on an N-body potential. Phys. Rev. Lett. 63, 2244–2247. https://doi.org/10.1103/PhysRevLett.63.2244
Wilson, D., Dunne, F.P.E., 2019. A mechanistic modelling methodology for microstructure-sensitive fatigue crack growth. J. Mech. Phys. Solids 124, 827–848. https://doi.org/10.1016/j.jmps.2018.11.023
Wilson, D., Wan, W., Dunne, F.P.E., 2019. Microstructurally-sensitive fatigue crack growth in HCP, BCC and FCC polycrystals. J. Mech. Phys. Solids 126, 204–225. https://doi.org/10.1016/j.jmps.2019.02.012
Wilson, D., Zheng, Z., Dunne, F.P.E., 2018. A microstructure-sensitive driving force for crack growth. J. Mech. Phys. Solids 121, 147–174. https://doi.org/10.1016/j.jmps.2018.07.005
Wohler, A., 1860. Versuche liber die Festigkeit der Eisenbahnwagenachsen. Zeitschrift fur Bauwes.
Wood, W.A., 1958. Formation of fatigue cracks. Philos. Mag. 3, 692–699. https://doi.org/10.1080/14786435808237004
Wu, L., Agnew, S.R., Ren, Y., Brown, D.W., Clausen, B., Stoica, G.M., Wenk, H.R., Liaw, P.K., 2010. The effects of texture and extension twinning on the low-cycle fatigue behavior of a rolled magnesium alloy, AZ31B. Mater. Sci. Eng. A 527, 7057–7067. https://doi.org/10.1016/j.msea.2010.07.047
Xu, Y., Wan, W., Dunne, F.P.E., 2021. Microstructural fracture mechanics: Stored energy density at fatigue cracks. J. Mech. Phys. Solids 146, 104209. https://doi.org/10.1016/j.jmps.2020.104209
Zerbst, U., Vormwald, M., Pippan, R., Gänser, H.P., Sarrazin-Baudoux, C., Madia, M., 2016. About the fatigue crack propagation threshold of metals as a design criterion - A review. Eng. Fract. Mech. 153, 190–243. https://doi.org/10.1016/j.engfracmech.2015.12.002
Zhai, T., Jiang, X.P., Li, J.X., Garratt, M.D., Bray, G.H., 2005. The grain boundary geometry for optimum resistance to growth of short fatigue cracks in high strength Al-alloys. Int. J. Fatigue 27, 1202–1209. https://doi.org/10.1016/j.ijfatigue.2005.06.021
Zhai, T., Wilkinson, A.J., Martin, J.W., 2000. Crystallographic mechanism for fatigue crack propagation through grain boundaries. Acta Mater. 48, 4917–4927. https://doi.org/10.1016/S1359-6454(00)00214-7
Zhang, Y.H., Edwards, L., 1992. The effect of grain boundaries on the development of plastic deformation ahead of small fatigue cracks. Scr. Metall. Mater. 26, 1901–1906. https://doi.org/10.1016/0956-716X(92)90056-K
Zhang, Z., Dunne, F.P.E., 2017. Microstructural heterogeneity in rate-dependent plasticity of multiphase titanium alloys. J. Mech. Phys. Solids 103, 199–220.

https://doi.org/10.1016/j.jmps.2017.03.012
Zhang, Z., Jun, T.S., Britton, T.B., Dunne, F.P.E., 2016. Intrinsic anisotropy of strain rate sensitivity in single crystal alpha titanium. Acta Mater. 118, 317–330. https://doi.org/10.1016/j.actamat.2016.07.044
Zheng, Z., Balint, D.S., Dunne, F.P.E., 2016a. Discrete dislocation and crystal plasticity analyses of load shedding in polycrystalline titanium alloys. Int. J. Plast. 87, 15–31. https://doi.org/10.1016/j.ijplas.2016.08.009
Zheng, Z., Balint, D.S., Dunne, F.P.E., 2016b. Rate sensitivity in discrete dislocation plasticity in hexagonal close-packed crystals. Acta Mater. 107, 17–26. https://doi.org/10.1016/j.actamat.2016.01.035
Zheng, Z., Prastiti, N.G., Balint, D.S., Dunne, F.P.E., 2019. The dislocation configurational energy density in discrete dislocation plasticity. J. Mech. Phys. Solids 129, 39–60. https://doi.org/10.1016/j.jmps.2019.04.015

Appendix

Appendix A. In-plane strain measurement by cross-correlation algorithm

Speckle images were captured by optical microscope, and then processed by a cross-correlation algorithm for two-dimensional strain measurement. The basic principle of digital image correlation (DIC) is the tracking of the same features (pixels) moving across the surface of the two images captured before and after deformation. A square reference subset of (2D + 1) × (2D + 1) pixels centred at point P (x_0, y_0) from the image recorded before deformation is selected to track its corresponding location in the deformed image as schematically shown in Fig. A-1.

The cross-correlation algorithm was utilised to evaluate the similarity degree between the reference subset and the deformed subset. The matching procedure is completed through searching the peak position of the distribution of correlation coefficient:

$$S = \sum_{i=-D}^{D} \sum_{j=-D}^{D} [f(x_i, y_j) g(x'_i, y'_j)]$$

where $f(x_i, y_j)$ is the gray level value at coordinate (x_i, y_j) of the reference subset and $g(x'_i, y'_j)$ is the gray level value at (x'_i, y'_j) of the deformed subset (Bruck et al., 1989). The shifts of point P along x-axis and y-axis from the reference subset centre to the target (deformed) subset centre can be obtained when the correlation coefficient extremum is detected.

The cross-correlation algorithm was performed using two steps: the first step corrected

the average rigid body translation and the whole frame rotation of the image within 256 × 256 pixels large subset; the second step was carried out on a regular grid of the region of interest (ROI) with the subset size of 64 × 64 pixels and 95% overlapping. Cross-correlation was conducted with the spatial intensity information within the ROIs implemented in the Fourier domain (Chen et al., 1993). Band pass filtering was performed in the Fourier domain, which allowed noise to be removed by low pass (2,1) and high pass (24,12) filters (Jiang et al., 2016).

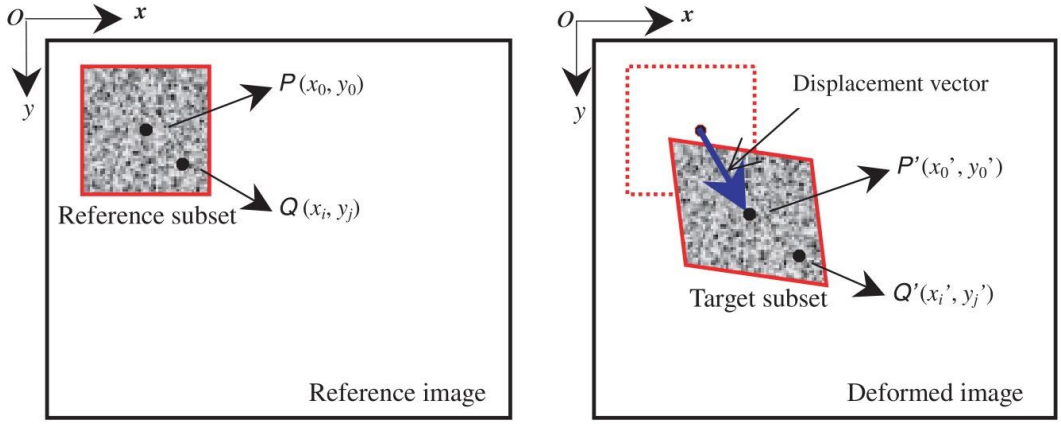


Fig. A-1 Schematic illustration of a reference square subset before and after deformation. Reprinted from (Pan et al., 2009).

Fig. A-2 shows the deformation configuration with displacements *u* and *v* along the x-axis and y-axis, respectively. The measurement of xy in-plane displacement allows four of nine components of the total deformation gradient tensor, F to be obtained by

$$\boldsymbol{F} = \begin{pmatrix} F_{11} & F_{12} & F_{13} \\ F_{21} & F_{22} & F_{23} \\ F_{31} & F_{32} & F_{33} \end{pmatrix} = \begin{pmatrix} \frac{\partial x}{\partial X} & \frac{\partial x}{\partial Y} & \frac{\partial x}{\partial Z} \\ \frac{\partial y}{\partial X} & \frac{\partial y}{\partial Y} & \frac{\partial y}{\partial Z} \\ \frac{\partial z}{\partial X} & \frac{\partial z}{\partial Y} & \frac{\partial z}{\partial Z} \end{pmatrix}$$

Another missing five components with respect to the z-direction are inaccessible (shown in red). Therefore, the Green strain can be derived from $\boldsymbol{F}$,

$$\boldsymbol{E} = \begin{pmatrix} \varepsilon_{xx} & \varepsilon_{xy} \\ \varepsilon_{xy} & \varepsilon_{yy} \end{pmatrix} = \frac{\boldsymbol{F}^T\boldsymbol{F} - \boldsymbol{I}}{2}$$

where $\boldsymbol{I}$ is the identity matrix.

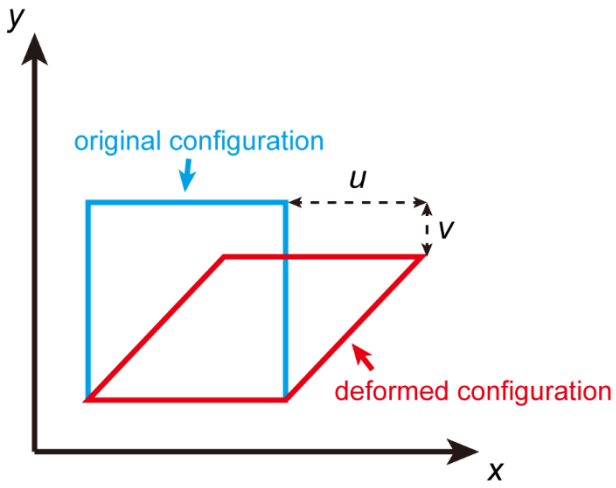


Fig. A-2. Schematic of configuration deformation with in-plane displacement *u* and *v*.

Appendix B. Rotation matrices mapping the reference crystal system into the local system for specified crystallographic orientation

The convention of the ZXZ rotation with the Euler angle, (φ_1 Φ φ_2) is: i) Rotate through φ_1 about the z-axis; ii) Rotate through Φ about the (new) x'-axis; iii) Rotate through φ_2 about the (new) z''-axis. Simply, this can be expressed as

$$\boldsymbol{R} = \boldsymbol{R}(\varphi_2)\boldsymbol{R}(\Phi)\boldsymbol{R}(\varphi_1)$$

where

$$\boldsymbol{R} = \begin{pmatrix} cos\varphi_2 & -sin\varphi_2 & 0 \\ sin\varphi_2 & cos\varphi_2 & 0 \\ 0 & 0 & 1 \end{pmatrix} \begin{pmatrix} 1 & 0 & 0 \\ 0 & cos\Phi & -sin\Phi \\ 0 & sin\Phi & cos\Phi \end{pmatrix} \begin{pmatrix} cos\varphi_1 & -sin\varphi_1 & 0 \\ sin\varphi_1 & cos\varphi_1 & 0 \\ 0 & 0 & 1 \end{pmatrix}$$

which can be written out as

$$\boldsymbol{R} = \begin{pmatrix} R_{11} & R_{12} & R_{13} \\ R_{21} & R_{22} & R_{23} \\ R_{31} & R_{32} & R_{33} \end{pmatrix}$$

To fulfil the rotation of stiffness matrix, $\boldsymbol{T_\sigma}$ and $\boldsymbol{T_\varepsilon}$ are the relevant rotation matrices for the stress and strain column vectors respectively with

$$\boldsymbol{\sigma'} = \boldsymbol{T_\sigma}\boldsymbol{\sigma}$$

$$\boldsymbol{\varepsilon'} = \boldsymbol{T_\varepsilon}\boldsymbol{\varepsilon}$$

where

$$\boldsymbol{T_\sigma} = \begin{pmatrix} R_{11}^2 & R_{21}^2 & R_{31}^2 & 2R_{11}R_{21} & 2R_{21}R_{31} & 2R_{31}R_{11} \\ R_{12}^2 & R_{22}^2 & R_{32}^2 & 2R_{12}R_{22} & 2R_{22}R_{32} & 2R_{32}R_{12} \\ R_{13}^2 & R_{23}^2 & R_{33}^2 & 2R_{13}R_{23} & 2R_{23}R_{33} & 2R_{33}R_{13} \\ R_{11}R_{12} & R_{21}R_{22} & R_{31}R_{32} & R_{11}R_{22}+R_{12}R_{21} & R_{21}R_{32}+R_{22}R_{31} & R_{31}R_{12}+R_{32}R_{11} \\ R_{12}R_{13} & R_{22}R_{23} & R_{32}R_{33} & R_{23}R_{12}+R_{13}R_{22} & R_{22}R_{33}+R_{23}R_{32} & R_{32}R_{13}+R_{33}R_{12} \\ R_{13}R_{11} & R_{23}R_{21} & R_{33}R_{31} & R_{13}R_{21}+R_{11}R_{23} & R_{23}R_{31}+R_{21}R_{33} & R_{33}R_{11}+R_{31}R_{13} \end{pmatrix}$$

and

$$\boldsymbol{T_\varepsilon} = \begin{pmatrix} R_{11}^2 & R_{21}^2 & R_{31}^2 & R_{11}R_{21} & R_{21}R_{31} & R_{31}R_{11} \\ R_{12}^2 & R_{22}^2 & R_{32}^2 & R_{12}R_{22} & R_{22}R_{32} & R_{32}R_{12} \\ R_{13}^2 & R_{23}^2 & R_{33}^2 & R_{13}R_{23} & R_{23}R_{33} & R_{33}R_{13} \\ 2R_{11}R_{12} & 2R_{21}R_{22} & 2R_{31}R_{32} & R_{11}R_{22}+R_{12}R_{21} & R_{21}R_{32}+R_{22}R_{31} & R_{31}R_{12}+R_{32}R_{11} \\ 2R_{12}R_{13} & 2R_{22}R_{23} & 2R_{32}R_{33} & R_{23}R_{12}+R_{13}R_{22} & R_{22}R_{33}+R_{23}R_{32} & R_{32}R_{13}+R_{33}R_{12} \\ 2R_{13}R_{11} & 2R_{23}R_{21} & 2R_{33}R_{31} & R_{13}R_{21}+R_{11}R_{23} & R_{23}R_{31}+R_{21}R_{33} & R_{33}R_{11}+R_{31}R_{13} \end{pmatrix}$$

Appendix C. Gradient algorithm in GND density calculation

Numerical implementation of the GND density estimation algorithm starts with

mapping the three strain components into a two-dimensional space with the uniform structured grid from the preceding DIC scanning step size (w_0, h_0). A Matlab built-in numerical differentiation function is utilized to calculate the GND density components based on the central difference:

$$G_x(i,j) = \frac{1}{2w}[H(i,j+1) - H(i,j-1)]$$

$$G_y(i,j) = \frac{1}{2h}[H(i+1,j) - H(i-1,j)]$$

where H represents any of the strain field 2nd order tensor mapped on the grid, G_x and G_y are the gradients of field H along the x and y directions, respectively. The grid size of the numerical gradient calculation (w, h) can differ from the DIC step size (w_0, h_0). However, any combination of more spacy choice of the grid would damage the resolution of the strain and its gradient field. On the other side, any combination of more compact choice of the grid would not make physical contribution for understanding the strain gradient. Therefore, we employ the identical grid configuration as the DIC step size to avoid loss of DIC resolution and to diminish the mesh size sensitivity, the latter of which has been a concern when GND density is calculated numerically (Kiener et al., 2011). The gradient values at boundary points are given by single-sided differentiation:

$$G_x(i,1) = \frac{1}{w}[H(i,2) - H(i,1)]$$

$$G_y(1,j) = \frac{1}{h}[H(2,j) - H(1,j)]$$